Chapter 4
Particle Detection

After reading this chapter, you should be able to manage the basics of particle detection, and to understand the sections describing the detection technique in a modern article of high-energy particle or astroparticle physics.

Particle detectors measure physical quantities related to the result of a collision; they should ideally identify all the outcoming (and the incoming, if unknown) particles and measure their kinematic characteristics (momentum, energy, velocity).

In order to detect a particle, one must make use of its interaction with a sensitive material. The interaction should possibly not destroy the particle that one wants to detect; however, for some particles this is the only way to obtain information.

In order to study the properties of detectors, we shall thus first need to review the characteristics of the interaction of particles with matter.

4.1 Interaction of Particles with Matter

4.1.1 Charged Particle Interactions

Charged particles interact basically with atoms, and the interaction is mostly electromagnetic: they might expel electrons (ionization), promote electrons to upper energy levels (excitation), or radiate photons (bremsstrahlung, Cherenkov radiation, transition radiation). High-energy particles may also interact directly with the atomic nuclei.

A. De Angelis and M. Pimenta, *Introduction to Particle and Astroparticle Physics*, Undergraduate Lecture Notes in Physics,
https://doi.org/10.1007/978-3-319-78181-5_4

4.1.1.1 Ionization Energy Loss

This is one of the most important sources of energy loss by charged particles. The average value of the specific (i.e., calculated per unit length) energy loss due to ionization and excitation whenever a particle goes through a homogeneous material of density ρ is described by the so-called Bethe formula.[1] This expression has an accuracy of a few % in the region $0.1 < \beta\gamma < 1000$ for materials with intermediate atomic number.

$$-\frac{dE}{dx} \simeq \rho D \left(\frac{Z}{A}\right) \frac{(z_p)^2}{\beta^2} \left[\frac{1}{2} \ln\left(\frac{2m_e c^2 \beta^2 \gamma^2}{I}\right) - \beta^2 - \frac{\delta(\beta, \rho)}{2}\right], \tag{4.1}$$

where

- ρ is the material density, in g/cm^3;
- Z and A are the atomic and mass number of the material, respectively;
- z_p is the charge of the incoming particle, in units of the electron charge;
- $D \simeq 0.307\,\text{MeV}\,\text{cm}^2/\text{g}$;
- $m_e c^2$ is the energy corresponding to the electron mass, $\sim$0.5 MeV;
- I is the mean excitation energy in the material; it can be approximated as $I \simeq 16\,\text{eV} \times Z^{0.9}$ for $Z > 1$;
- δ is a correction term that becomes important at high energies. It accounts for the reduction in energy loss due to the so-called *density effect*. As the incident particle velocity increases, media become polarized and their atoms can no longer be considered as isolated.

The energy loss by ionization (Fig. 4.1) in first approximation is:

- independent of the particle's mass;
- typically small for high-energy particles (about 2 MeV/cm in water; one can roughly assume a proportionality to the density of the material);
- proportional to $1/\beta^2$ for $\beta\gamma \leq 3$ (the minimum of ionization: minimum ionizing particle, often just called a "mip");
- basically constant for $\beta > 0.96$ (logarithmic increase after the minimum);
- proportional to Z/A (Z/A being about equal to 0.5 for all elements but hydrogen and the heaviest nuclei).

In practice, most relativistic particles (such as cosmic-ray muons) have mean energy loss rates close to the minimum; they can be considered within less than a factor of

[1] The 24-year-old Hans Bethe, Nobel Prize in 1967 for his work on the theory of stellar nucleosynthesis, published this formula in 1930; the formula—not including the density term, added later by Fermi—was derived using quantum mechanical perturbation theory up to z_p^2. The description can be improved by considering corrections which correspond to higher powers of z_p: Felix Bloch, Nobel Prize in 1952 for the development of new methods for nuclear magnetic precision measurements, obtained in 1933 a higher-order correction proportional to z_p^4, not reported in this text, and sometimes the formula is called "Bethe-Bloch energy loss"—although this naming convention has been discontinued by the Particle Data Group since 2008.

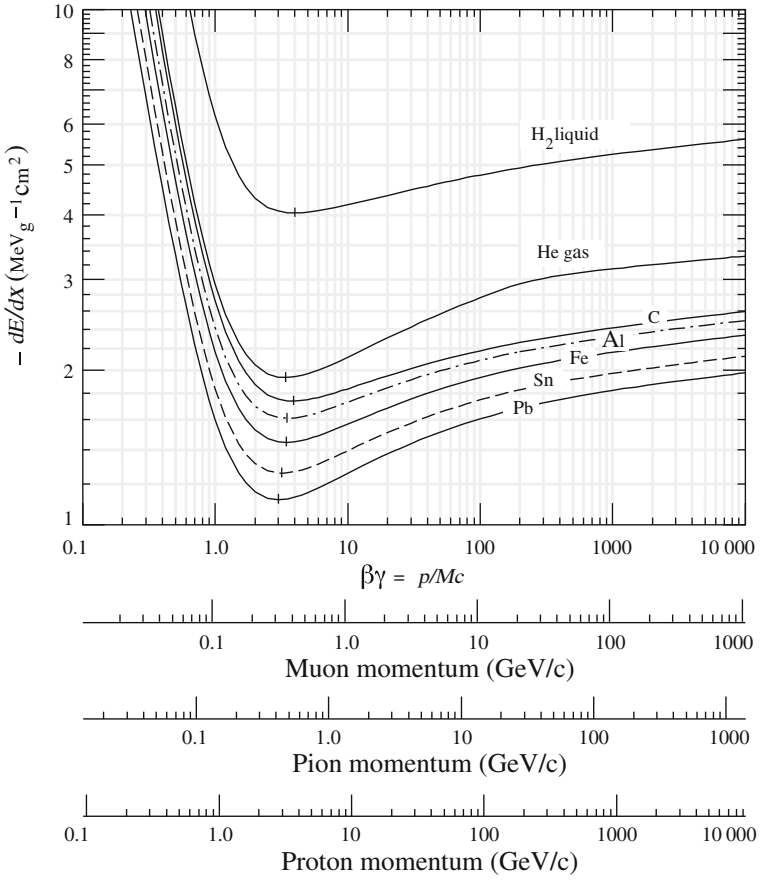

Fig. 4.1 Specific ionization energy loss for muons, pions, and protons in different materials. From K.A. Olive et al. (Particle Data Group), Chin. Phys. C 38 (2014) 090001

two as minimum ionizing particles. The loss from a minimum ionizing particle is well approximated as

$$\frac{1}{\rho}\frac{dE}{dx} \simeq -3.5\left(\frac{Z}{A}\right)\ \text{MeV}\,\text{cm}^2/\text{g}\,.$$

In any case, as we shall see later, the energy loss in the logarithmic increase region can be used by means of appropriate detectors for particle identification.

Due to the statistical nature of the ionization process, large fluctuations on the energy loss arise when fast charged particles pass through absorbers which are thin compared to the particle range. The energy loss is distributed around the most

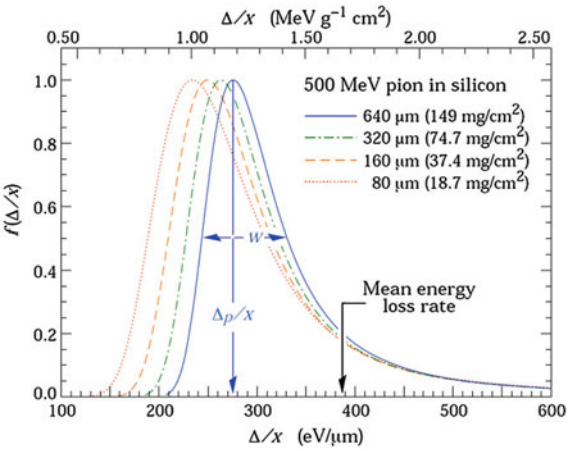

Fig. 4.2 Distribution of the energy loss (Landau distribution) in silicon for 500 MeV pions, normalized to unity at the most probable value. w is the full width at half maximum. From K.A. Olive et al. (Particle Data Group), Chin. Phys. C 38 (2014) 090001

probable value according to an asymmetric distribution (named the Landau[2] distribution). The average energy loss, represented by the Bethe formula, is larger than the most probable energy loss, since the Landau distribution has a long tail (as the width of the material increases, the most probable energy loss becomes however closer to the average, as one can see in Fig. 4.2).

Although its nature is quantum mechanical, the main characteristics of Eq. 4.1 can be derived classically, as it was first done by Bohr. Let us suppose a charged particle of mass m and charge z_p passes at a distance b from a target of mass M and charge Z. The momentum Δp transferred to the target depends on the electric field $\boldsymbol{\mathcal{E}}$ produced by the charged traveling particle. Given the symmetry of the problem only the transverse component of the electric field with the respect to the particle track $\mathcal{E}_\perp$ matters. Relating the interaction time t with the velocity of the particle, $dt = dx/v$, one can write for the momentum transfer:

$$\Delta p = \int_{-\infty}^{+\infty} F\ dt = \int_{-\infty}^{+\infty} e\ \mathcal{E}\ dt = \frac{e}{v} \int_{-\infty}^{+\infty} \mathcal{E}_\perp\ dx.$$

The electric field integral can be calculated using Gauss's law. In fact, the flux of the electric field passing through a cylinder of radius b is given by $\int \mathcal{E}_\perp\ 2\pi b\ dx = z_p\ e/\varepsilon_0$. Therefore, the momentum transferred to the target particle can be written as

$$\Delta p = \frac{z_p\ e^2}{2\ \pi\ \varepsilon_0\ v\ b}$$

[2]Lev Davidovich Landau (1908–1968) was a Soviet physicist who made fundamental contributions to many areas of theoretical physics, in particular quantum mechanics, particle physics, and the structure of matter. He received the 1962 Nobel Prize in Physics for his development of a mathematical theory of superfluidity.

or still in terms of the energy and using the classical radius of the electron[3] $r_e = (e^2/4\pi\epsilon_0)/(m_e c^2) \simeq 0.003$ pm:

$$\Delta E = \frac{\Delta p^2}{2\,m} = \left(\frac{1}{4\pi\varepsilon_0}\right)^2 \frac{1}{m\,c^2} \frac{2\,z_p^2\,Z^2\,e^4}{b^2\,\beta^2} = \frac{(m_e\,c^2)^2}{m\,c^2}\,\frac{2\,z_p^2\,Z^2}{\beta^2}\,\left(\frac{r_e}{b}\right)^2 .$$

From this expression one can see that close collisions ($\Delta E \propto 1/b^2$) and low mass particles ($\Delta E \propto 1/m$) are the most important with respect to energy loss; thus one can neglect the effect of nuclei.

Photoluminescence. In some transparent media, part of the ionization energy loss goes into the emission of visible or near-visible light by the excitation of atoms and/or molecules. This phenomenon is called photoluminescence; often it results into a fast ($<100\,\mu$s) excitation/de-excitation—in this last case we talk of fluorescence, or scintillation. Specialists often use definitions which distinguish between fluorescence and scintillation; this separation is, however, not universally accepted. We shall discuss later fluorescence in the context of the detection of large showers induced in the atmosphere by high-energy cosmic rays.

4.1.1.2 High-Energy Radiation Effects

According to classical electromagnetism, a charged particle undergoing acceleration radiates electromagnetic waves. The intensity of the emitted radiation from a dipole is proportional to the square of the acceleration.

Particles deflected by the electric field of the material traversed, thus, also emit photons. We speak in this case of bremsstrahlung, or braking radiation.

To first order, the emitted energy is (as in the classical case) proportional to the inverse of the square of the mass. On top of the ionization energy loss described by Eq. 4.1, above $\beta\gamma \sim 1000$ (which means an extremely high energy for a proton, $E \sim 1$ TeV, but just $E \sim 100$ GeV for a muon), such radiation effects become important (Fig. 4.3).

Bremsstrahlung is particularly relevant for electrons and positrons, particles for which the Bethe approximation starts to be inadequate even at lower energies. The average fractional energy loss by radiation for an electron of high energy ($E \gg m_e c^2$) is approximately independent of the energy itself, and can be described by

$$\frac{1}{E}\frac{dE}{dx} \simeq -\frac{1}{X_0} \tag{4.2}$$

[3]The classical electron radius is the size the electron would need to have for its mass to be completely due to its electrostatic potential energy, under the assumption that charge has a uniform volume density and that the electron is a sphere.

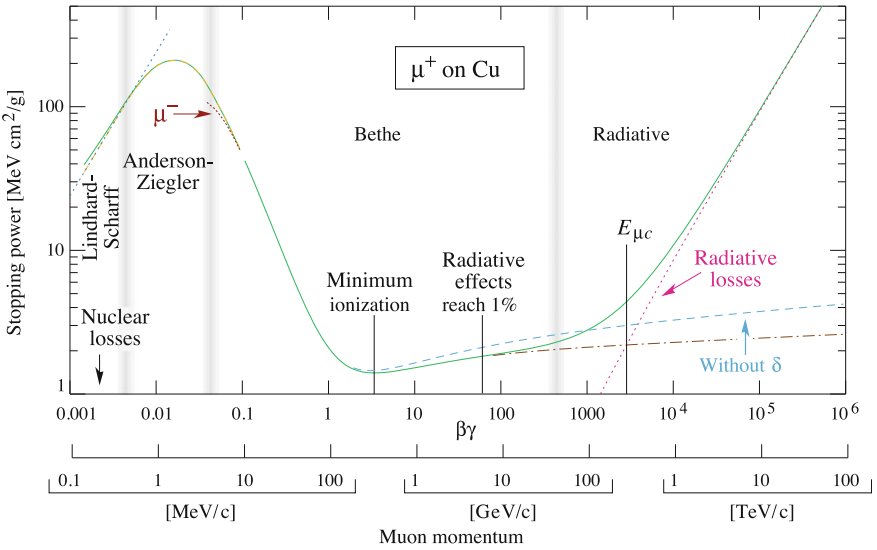

Fig. 4.3 The stopping power $(-dE/dx)$ for positive muons in copper as a function of $\beta\gamma = p/Mc$ is shown over nine orders of magnitude in momentum (corresponding to 12 orders of magnitude in kinetic energy). From K.A. Olive et al. (Particle Data Group), Chin. Phys. C 38 (2014) 090001

where X_0 is called the radiation length, and is characteristic of the material—for example, it is about 300 m for air at Normal Temperature and Pressure (NTP),[4] about 36 cm for water, about 0.5 cm for lead.

The radiation length has been tabulated for different elements in Appendix B; a good approximation (for $Z > 4$) is

$$\frac{1}{X_0} = 4\left(\frac{\hbar}{m_e c}\right)^2 Z(Z+1)\alpha^3 n_a \ln\left(\frac{183}{Z^{1/3}}\right) , \tag{4.3}$$

where $\alpha = \frac{e^2}{4\pi}$ and n_a is the density of atoms per cubic centimeter in the medium, or more simply

$$\frac{1}{\rho}X_0 \simeq 180\frac{A}{Z^2}\text{cm} \quad \left(\frac{\Delta X_0}{X_0} < \pm 20\% \text{ for } 12 < Z < 93\right) . \tag{4.4}$$

[4] NTP is commonly used as a standard condition; it is defined as air at 20 °C (293.15 K) and 1 atm (101.325 kPa). Density is 1.204 kg/m^3. Standard Temperature and Pressure STP, another condition frequently used in physics, is defined by IUPAC (International Union of Pure and Applied Chemistry) as air at 0 °C (273.15 K) and 100 kPa.

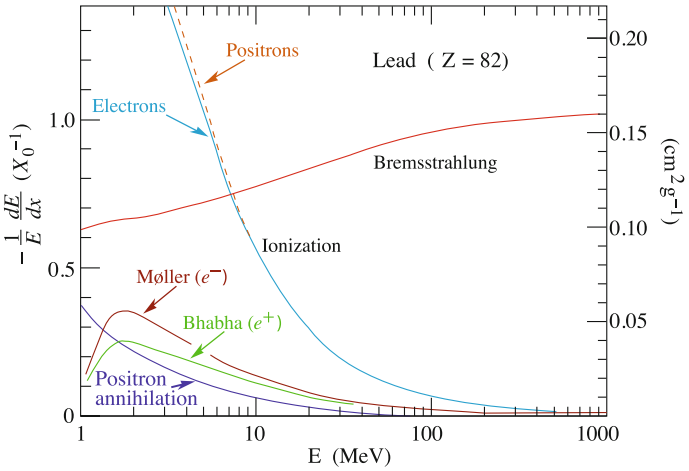

Fig. 4.4 Fractional energy loss per radiation length in lead as a function of the electron or positron energy. From K.A. Olive et al. (Particle Data Group), Chin. Phys. C 38 (2014) 090001

The total average energy loss by radiation increases rapidly (linearly in the approximation of Eq. 4.2) with energy, while the average energy loss by collision is practically constant. At high energies, radiation losses are thus much more important than collision losses (Fig. 4.4).

The energy at which the radiation energy loss overtakes the collision energy loss (called the critical energy, E_c) decreases with increasing atomic number:

$$E_c \simeq \frac{550\,\text{MeV}}{Z} \left(\frac{\Delta E_c}{E_c} < \pm 10\% \text{ for } 12 < Z < 93 \right) . \tag{4.5}$$

The critical energy for air at NTP is about 84 MeV; for water it is about 74 MeV.

The photons radiated by bremsstrahlung are distributed at leading order in such a way that the energy loss per unit energy is constant, i.e.,

$$\frac{dN_\gamma}{dE_\gamma} \propto \frac{1}{E_\gamma}$$

between 0 and E. This results in a divergence for $E_\gamma \to 0$, which anyway does not contradict energy conservation: the integral of the energy released for each energy bin is constant.

The emitted photons are collimated: the typical angle of emission is $\sim m_e c^2/E$.

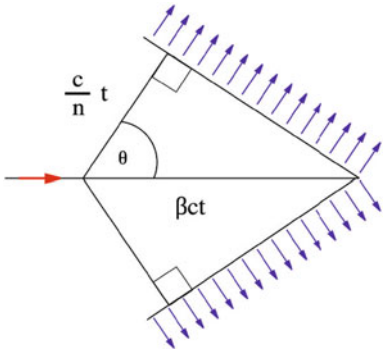

Fig. 4.5 Emission of Cherenkov radiation by a charged particle. User Harp, Creative Commons Attribution-Share Alike 2.5 Generic license via Wikimedia Commons

4.1.1.3 Cherenkov Radiation

The Vavilov–Cherenkov[5] radiation (commonly called just Cherenkov radiation) occurs when a charged particle moves through a medium faster than the speed of light in that medium. The total energy loss due to this process is negligible; however, Cherenkov radiation is important due to the possibility of use in detectors.

The light is emitted in a coherent cone (Fig. 4.5) at an angle such that

$$\cos\theta_c = \frac{1}{n\beta} \tag{4.6}$$

from the direction of the particle. The threshold velocity is thus $\beta = 1/n$, where n is the refractive index of the medium. The presence of a coherent wavefront can be easily derived by using the Huygens–Fresnel principle.

The number of photons produced per unit path length and per unit energy interval of the photons by a particle with charge $z_p e$ at the maximum (limiting) angle is

$$\frac{d^2N}{dEdx} \simeq \frac{\alpha z_p^2}{\hbar c}\sin^2\theta_c \simeq 370\sin^2\theta_c\,\mathrm{eV}^{-1}\mathrm{cm}^{-1} \tag{4.7}$$

or equivalently

$$\frac{d^2N}{d\lambda dx} \simeq \frac{2\pi\alpha z_p^2}{\lambda^2}\sin^2\theta_c \tag{4.8}$$

(the index of refraction n is in general a function of photon energy E; Cherenkov radiation is relevant when $n > 1$ and the medium is transparent, and this happens close to the range of visible light).

[5] Pavel Cherenkov (1904–1990) was a Soviet physicist who shared the Nobel Prize in physics in 1958 with compatriots Ilya Frank (1908–1990) and Igor Tamm (1895–1971) for the discovery of Cherenkov radiation, made in 1934. The work was done under the supervision of Sergey Vavilov, who died before the recognition for the discovery by the Nobel committee.

The total energy radiated is small, some 10^{-4} times the energy lost by ionization. In the visible range (300–700 nm), the total number of emitted photons is about 40/m in air, about 500/cm in water. Due to the dependence on λ, it is important that Cherenkov detectors are sensitive close to the ultraviolet region.

Dense media can be transparent not only to visible light, but also to radio waves. The development of Cherenkov radiation in the radiowave region due to the interactions with electrons in the medium is often referred to as the Askar'yan effect. This effect has been experimentally confirmed for different media (namely sand, rock salt, and ice) in accelerator experiments at SLAC; presently attempts are in progress to use this effect in particle detectors.

4.1.1.4 Transition Radiation

X-ray transition radiation (XTR) occurs when a relativistic charged particle crosses from one medium to another with different dielectric permittivity.

The energy radiated when a particle with charge $z_p e$ and $\gamma \simeq 1000$ crosses the boundary between vacuum and a different transparent medium is typically concentrated in the soft X-ray range 2–40 keV.

The process is closely related to Cherenkov radiation, and also in this case the total energy emitted is low (typically the expected number of photons per transition is smaller than unity; one thus needs several layers to build a detector).

4.1.2 Range

From the specific energy loss as a function of energy, we can calculate the fraction of energy lost as a function of the distance x traveled in the medium. This is known as the Bragg curve. For charged particles, most of the energy loss is due to ionization and occurs near the end of the path, where the particle speed is low. The Bragg curve has a pronounced peak close to the end of the path length and then falls rapidly to zero. The range R for a particle of energy E is the average distance traveled before reaching the energy at which the particle is absorbed (Fig. 4.6):

$$R(E') = \int_E^{Mc^2} \frac{1}{dE/dx} dE \,.$$

4.1.3 Multiple Scattering

A charged particle passing near a nucleus undergoes deflection, with an energy loss that is in most cases negligible. This phenomenon is called elastic scattering and is

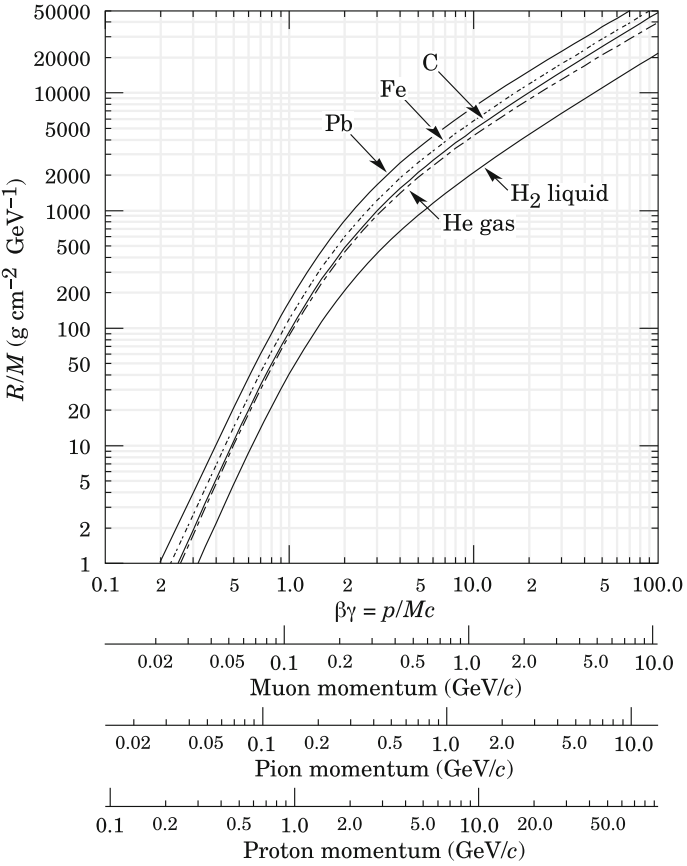

Fig. 4.6 Range per unit of density and of mass for heavy charged particles in liquid (bubble chamber) hydrogen, helium gas, carbon, iron, and lead. Example: a K^+ with momentum 700 MeV/c, $\beta\gamma \simeq 1.42$, and we read $R/M \simeq 396$, in lead, corresponding to a range of 195 g/cm^2. From K.A. Olive et al. (Particle Data Group), Chin. Phys. C 38 (2014) 090001

caused by the interaction between the particle and the Coulomb field of the nucleus. The global effect is that the path of the particle becomes a random walk (Fig. 4.7), and information on the original direction is partly lost—this fact can create problems for the reconstruction of direction in tracking detectors. For very-high-energy hadrons, also the hadronic cross section can contribute to the effect.

Summing up many relatively small random changes on the direction of flight of a particle of unit charge traversing a thin layer of material, the distribution of its projected scattering angle can be approximated by a Gaussian distribution of standard deviation projected on a plane (one has to multiply by $\sqrt{2}$ to determine the standard deviation in space):

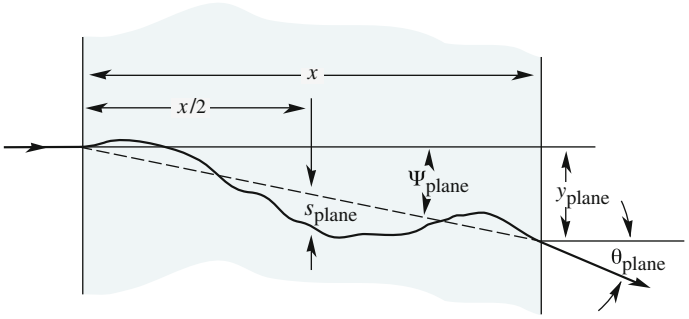

Fig. 4.7 Multiple Coulomb scattering. From K.A. Olive et al. (Particle Data Group), Chin. Phys. C 38 (2014) 090001

$$\theta_0 \simeq \frac{13.6\,\text{MeV}}{\beta cp} z_p \sqrt{\frac{x}{X_0}} \left[1 + 0.038 \ln \frac{x}{X_0} \right] .$$

X_0 is the radiation length defined before. The above expression comes from the so-called Molière theory, and is accurate to some 10% or better for $10^{-3} < x/X_0 < 100$. For an ultrarelativistic particle of absolute charge 1 it simplifies to

$$\theta_0 \simeq \frac{13.6\,\text{MeV}}{E} \sqrt{\frac{x}{X_0}} .$$

In some collisions however, deflections due to Rutherford scattering can be large and contribute to a sizable non-Gaussian tail.

4.1.4 Photon Interactions

High-energy photons mostly interact with matter via photoelectric effect, Compton scattering, and electron–positron pair production. Other processes, like Rayleigh scattering and photonuclear interactions, have in general much smaller cross sections.

4.1.4.1 Photoelectric Effect

The photoelectric effect is the ejection of an electron from a material that has just absorbed a photon. The ejected electron is called a *photoelectron*.

The photoelectric effect was pivotal in the development of quantum physics (for the explanation of this effect Albert Einstein was awarded the Nobel Prize). Due to photoelectric effect, a photon of angular frequency $\omega > V/e$ can eject from a metal an electron, which pops up with a kinetic energy $\hbar\omega - V$, where V is the minimum

gap of energy of electrons trapped in the metal (V is frequently called the *work function* of the metal).

No simple relationship between the attenuation of the incident electromagnetic wave and the photon energy E can be derived, since the process is characterized by the interaction with the (quantized) orbitals. The plot of the attenuation coefficient (the distance per unit density at which intensity is reduced by a factor $1/e$) as a function of the photon energy displays sharp peaks at the binding energies of the different orbital shells and depends strongly on the atomic number. Neglecting these effects, a reasonable approximation for the cross section σ is

$$\sigma \propto \frac{Z^{\nu}}{E^3},$$

with the exponent ν varying between 4 and 5 depending on the energy. The cross section rapidly decreases with energy above the typical electron binding energies (Fig. 4.8).

The photoelectric effect can be used for detecting photons below the MeV; a photosensor (see later) sensitive to such energies can "read" the signal generated by a photoelectron, possibly amplified by an avalanche process.

4.1.4.2 Compton Scattering

Compton scattering is the collision between a photon and an electron. Let E be the energy of the primary photon (corresponding to a wavelength λ) and suppose that the electron is initially free and at rest. After the collision, the photon is scattered at an angle θ and comes out with a reduced energy E', corresponding to a wavelength

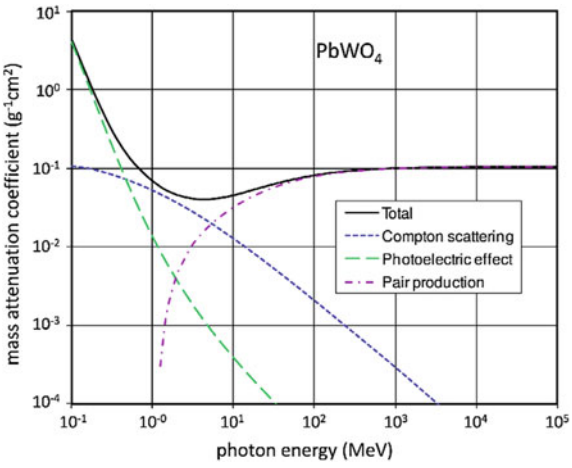

Fig. 4.8 Photon mass attenuation coefficient (cross section per gram of material) as a function of energy in lead tungstate (data from the NIST XCOM database)

λ'; the electron acquires an energy $E - E'$. The conservation laws of energy and momentum yield the following relation (Compton formula):

$$\lambda' - \lambda = \lambda_C(1 - \cos\theta) \longrightarrow E' = \frac{E}{1 + \frac{E}{m_e c^2}(1 - \cos\theta)}$$

where θ is the scattering angle of the emitted photon; $\lambda_C = h/m_e c \simeq 2.4$ pm is the Compton wavelength of the electron.

It should be noted that, in the case when the target electron is not at rest, the energy of the scattered photon can be larger than the energy of the incoming one. This regime is called *inverse Compton,* and it has great importance in the emission of high-energy photons by astrophysical sources: in practice, thanks to inverse Compton, photons can be "accelerated."

The differential cross section for Compton scattering was calculated by Klein and Nishina around 1930. If the photon energy is much below $m_e c^2$ (so the scattered electrons are nonrelativistic) then the total cross section is given by the Thomson cross section. This is known as the Thomson limit. The cross section for $E \ll m_e c^2$ (Thomson regime) is about

$$\sigma_T \simeq \frac{8\pi\alpha^2}{3m_e^2} = \frac{8\pi r_e^2}{3}\,, \tag{4.9}$$

where $r_e = (e^2/4\pi\epsilon_0)/(m_e c^2) \simeq 0.003$ pm is the classical radius of the electron. If the photon energy is $E \gg m_e c^2$, we are in the so-called Klein–Nishina regime and the total cross section falls off rapidly with increasing energy (Fig. 4.8):

$$\sigma_{KN} \simeq \frac{3\sigma_T}{8}\frac{\ln 2E}{E}\,. \tag{4.10}$$

As in the case of the photoelectric effect, the ejected electron can be detected (possibly after multiplication) by an appropriate sensor.

4.1.4.3 Pair Production

Pair production is the most important interaction process for a photon above an energy of a few tens of MeV. In the electric field in the neighborhood of a nucleus, a high-energy photon has a non-negligible probability of transforming itself into a negative and a positive electron—the process being kinematically forbidden unless an external field, regardless of how little, is present.

Energy conservation yields the following relation between the energy E of the primary photon and the total energies U and U' of the electrons:

$$E = U + U'.$$

With reasonable approximation, for 1 TeV$> E >$ 100 MeV the fraction of energy $u = U/E$ taken by the secondary electron/positron is uniformly distributed between 0 and 1 (becoming peaked at the extremes as the energy increases to values above 1 PeV).

The cross section grows quickly from the kinematic threshold of about 1 MeV to its asymptotic value reached at some 100 MeV:

$$\sigma \simeq \frac{7}{9}\frac{1}{n_a X_0}\,,$$

where n_a is the density of atomic nuclei per unit volume, in such a way that the interaction length is

$$\lambda \simeq \frac{9}{7}X_0\,.$$

The angle of emission for the particles in the pair is typically $\sim 0.8\,\mathrm{MeV}/E$.

4.1.4.4 Rayleigh Scattering and Photonuclear Interactions

Rayleigh scattering (the dispersion of electromagnetic radiation by particles with radii $\lesssim$1/10 the wavelength of the radiation) is usually of minor importance for the conditions of high-energy particle and astroparticle physics, but it can be important for light in the atmosphere, and thus for the design of instruments detecting visible light. The photonuclear effect, i.e., the excitation of nuclei by photons, is mostly restricted to the region around 10 MeV, and it may amount to as much as 10% of the total cross section due to electrodynamic effects.

4.1.4.5 Comparison Between Different Processes for Photons

The total Compton scattering probability decreases rapidly when the photon energy increases. Conversely, the total pair production probability is a slowly increasing function of energy. At large energies, most photons are thus absorbed by pair production, while photon absorption by the Compton effect dominates at low energies (being the photoelectric effect characteristic of even smaller energies). The absorption of photons by pair production, Compton, and photoelectric effect is compared in Fig. 4.8.

As a matter of fact, above about 30 MeV the dominant process is pair production, and the interaction length of a photon is, to an extremely good approximation, equal to $9X_0/7$.

At extremely high matter densities and/or at extremely high energies (typically above 10^{16}–10^{18} eV, depending on the medium composition and density) collisions cannot be treated independently, and the result of the collective quantum mechanical treatment is a reduction of the cross section. The result is the so-called

Landau–Pomeranchuk–Migdal effect, or simply LPM effect, which entails a reduction of the pair production cross section, as well as of bremsstrahlung.

4.1.5 Nuclear (Hadronic) Interactions

The nuclear force is felt by hadrons, charged and neutral; at high energies (above a few GeV), the inelastic cross section for hadrons is dominated by nuclear interaction.

High-energy nuclear interactions are difficult to model. A useful approximation is to describe them by an inelastic interaction length λ_H. Values for $\rho\lambda_H$ are typically of the order of 100 g/cm^2; a listing for some common materials is provided in Appendix B—where the inelastic interaction length λ_I and the total interaction length λ_T are separately listed, and the rule for the composition is $1/\lambda_T = 1/\lambda_H + 1/\lambda_I$.

The final state products of inelastic high-energy hadronic collisions are mostly pions, since these are the lightest hadrons. The rate of positive, negative, and neutral pions is more or less equal—as we shall see, this fact is due to an approximate symmetry of hadronic interactions, called the *strong isospin* symmetry.

4.1.6 Interaction of Neutrinos

The case of neutrinos is a special one. Neutrinos have a very low interaction cross section. High-energy neutrinos mainly interact with nucleons, being the neutrino-lepton cross section smaller—with the exception of the peak corresponding to the production of the $W^{\pm}$ boson in neutrino-lepton interactions at $E_\nu \sim 10^{16}$ eV.

The neutrino-nucleon cross section grows with energy. It can be parameterized for intermediate energies, $1\,\text{MeV} \lesssim E \lesssim 10\,\text{TeV}$ (Fig. 4.9) as

$$\sigma_{\nu N} \simeq (0.67 \times 10^{-38} E)\,\text{cm}^2 = (6.7\,E)\,\text{fb}\,, \tag{4.11}$$

E being the neutrino energy in GeV. At energies between 10 and 10^7 TeV (10^{19} eV), a parametrization is

$$\sigma_{\nu N} \simeq \left(0.67 \times 10^{-34} \sqrt{\frac{E}{10\,\text{TeV}}}\right) \text{cm}^2. \tag{4.12}$$

Solar neutrinos, which have MeV energies, typically cross the Earth undisturbed (see a more complete discussion in Chap. 9).

The low value of the interaction cross section makes the detection of neutrinos very difficult.

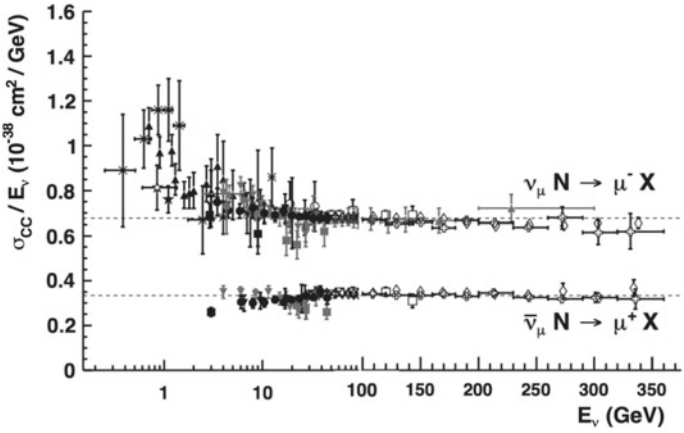

Fig. 4.9 Measurements of muon neutrino and antineutrino inclusive scattering cross sections divided by neutrino energy as a function of neutrino energy; different symbols represent measurements by different experiments. Note the transition between logarithmic and linear scales at 100 GeV. From K.A. Olive et al. (Particle Data Group), Chin. Phys. C 38 (2014) 090001

4.1.7 Electromagnetic Showers

High-energy electrons lose most of their energy by radiation. Thus, in their interaction with matter, most of the energy is spent in the production of high-energy photons and only a small fraction is dissipated. The secondary photons, in turn, undergo pair production (or, at lower energies, Compton scattering); secondary electrons and positrons can in turn radiate. This phenomenon continues generating cascades (showers) of electromagnetic particles; at each step the number of particles increases while the average energy decreases, until the energy falls below the critical energy.

Given the characteristics of the interactions of electrons/positrons and of photons with matter, it is natural to describe the process of electromagnetic cascades in terms of the scaled distance

$$t = \frac{x}{X_0}$$

(where X_0 is the radiation length), and of the scaled energy

$$\epsilon = \frac{E}{E_c}$$

(where E_c is the critical energy); the radiation length and the critical energy have been defined in Sect. 4.1.1.2. Since the opening angles for bremsstrahlung and pair production are small, the process can be in first approximation (above the critical energy) considered as one-dimensional (the lateral spread will be discussed at the end of this section).

A simple approximation (a "toy model"), proposed by Heitler in the late 1930s, assumes that

- the incoming charged particle has an initial energy E_0 much larger than the critical energy E_c;
- each electron travels one radiation length and then gives half of its energy to a bremsstrahlung photon;
- each photon travels one radiation length and then creates an electron–positron pair; the electron and the positron each carry half of the energy of the original photon.

In the above model, asymptotic formulas for radiation and pair production are assumed to be valid; the Compton effect and the collision processes are neglected. The branching stops abruptly when $E = E_c$, and then electrons and positrons lose their energy by ionization.

This simple branching model is schematically shown in Fig. 4.10, left. It implies that after t radiation lengths the shower will contain 2^t particles and there will be roughly the same number of electrons, positrons, and photons, each with an average energy

$$E(t) = E_0/2^t \,.$$

The cascading process will stop when $E(t) = E_c$, at a thickness of absorber $t_{\max}$, that can be written in terms of the initial and critical energies as

$$t_{\max} = \log_2(E_0/E_c) \,,$$

with the number of particles at this point given by

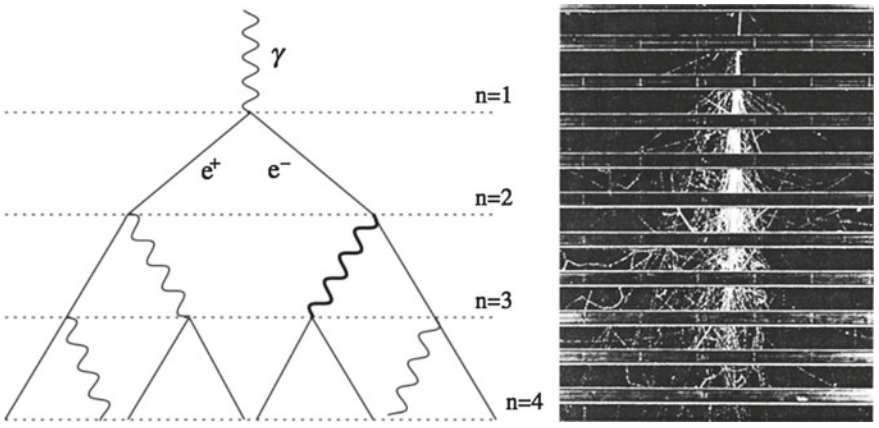

Fig. 4.10 Left: Scheme of the Heitler approximation for the development of an electromagnetic shower. From J. Matthews, Astropart. Phys. 22 (2005) 387. Right: Image of an electromagnetic shower developing through a number of brass plates 1.25 cm thick placed across a cloud chamber (from B. Rossi, "Cosmic rays," McGraw-Hill 1964)

$$N_{\max} = \frac{E_0}{E_c} \equiv y\,.$$

The model suggests that the shower depth at its maximum varies as the logarithm of the primary energy. This emerges also from more sophisticated shower models and is observed experimentally. A real image of an electromagnetic shower in a cloud chamber is shown in Fig. 4.10, right.

An improved model was formulated by Rossi in the beginning of the 1940s. Rossi (see, e.g., reference [F4.1]) computed analytically the development of a shower in the so-called approximation B in which: electrons lose energy by ionization and bremsstrahlung (described by asymptotical formulae); photons undergo pair production, also described by asymptotic formulae. All the process is one-dimensional. The results of the "Rossi approximation B" are summarized in Table 4.1. Under this approximation, the number of particles grows exponentially in the beginning up to the maximum, and then decreases as shown in Figs. 4.11 and 4.12.

A common parameterization of the longitudinal profile for a shower of initial energy E_0 is

Table 4.1 Shower parameters for a particle on energy E_0 according to Rossi's approximation B ($y = E_0/E_c$)

	Incident electron	Incident photon
Peak of shower $t_{\max}$	$1.0 \times (\ln y - 1)$	$1.0 \times (\ln y - 0.5)$
Center of gravity t_{med}	$t_{\max} + 1.4$	$t_{\max} + 1.7$
Number of e^+ and e^- at peak	$0.3y/\sqrt{\ln y - 0.37}$	$0.3y/\sqrt{\ln y - 0.31}$
Total track length	y	y

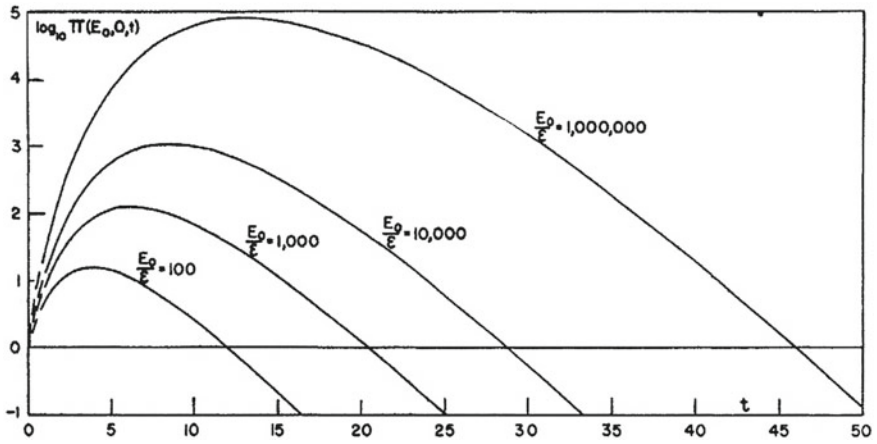

Fig. 4.11 Logarithm of the number of electrons for electron-initiated showers, calculated under Rossi approximation B, as a function of the number of radiation lengths traversed. Multiplication by E_c/I (E_c is called ε in the figure) yields the specific ionization energy loss [F4.1]

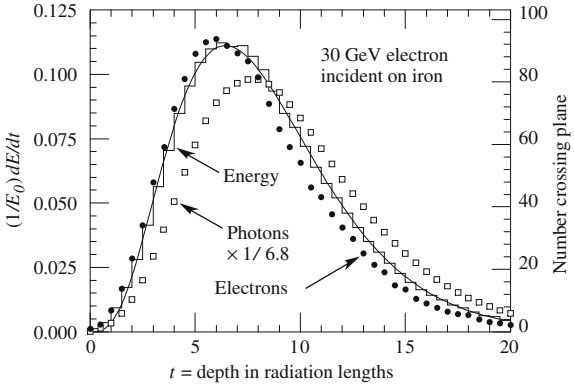

Fig. 4.12 A Monte Carlo simulation of a 30 GeV electron-induced cascade in iron. The histogram shows the fractional energy deposition per radiation length, and the curve is a fit to the distribution using Eq. 4.13. The circles indicate the number of electrons with total energy greater than 1.5 MeV crossing planes at $X_0/2$ intervals (scale on the right) and the squares the number of photons above the same energy crossing the planes (scaled down to have the same area as the electron distribution). From K.A. Olive et al. (Particle Data Group), Chin. Phys. C 38 (2014) 090001

$$\frac{dE}{dt} = E_0 \frac{\beta}{\Gamma(\alpha)} (\beta t)^{\alpha-1} e^{-\beta t} \,, \tag{4.13}$$

where Γ is Euler's Gamma function $\Gamma(z) = \int_0^{+\infty} t^{z-1}\, e^{-t}\, dt$. In the above approximation, $t_{\max} = (\alpha - 1)/\beta$, which should be thus equal to $\ln(E_0/E_c) - C$ with $C = 1$ for an electron and $C = 0.5$ for a photon.

Fluctuations on the total track length are dominated by the fluctuations on the total number of particles, and thus they grow as $\sqrt{E_0}$. An incomplete longitudinal containment of the shower badly increases fluctuations on the deposited energy. A rule of thumb for the longitudinal containment of 95% of the shower is

$$T(95\%) = (t_{\max} + 0.08Z + 9.6) \,,$$

expressed in radiation lengths.

Despite the elegance of Rossi's calculations, one can do better using computers, and most calculations are performed nowadays by Monte Carlo methods.[6] Monte Carlo calculations of electromagnetic cascades have the advantages of using accurate cross sections for bremsstrahlung and pair production, the correct energy dependence of ionization loss, and including all electromagnetic interactions. Monte Carlo calculations, in addition, give correct account for the fluctuations in the shower development, as well as for the angular and lateral distribution of the shower particles. Rossi's approximation B, however, is faster and represents a rather accurate model.

[6]Monte Carlo methods are computational algorithms based on repeated random sampling. The name is due to its resemblance to the act of playing in a gambling casino.

The description of the transverse development of a shower is more complicated. Usually the normalized lateral density distribution of electrons is approximated by the Nishimura–Kamata–Greisen (NKG) function, which depends on the "shower age" s, being 0 at the first interaction, 1 at the maximum, and 3 at the death [F4.1]:

$$s = \frac{3t}{t + 2t_{\max}} \,. \tag{4.14}$$

The NKG function:

$$\rho_{\mathrm{NKG}}(r, s, N_e) = \frac{N_e}{R_M^2} \frac{\Gamma(4.5 - s)}{2\pi\Gamma(s)\Gamma(4.5 - 2s)} \left(\frac{r}{R_M}\right)^{s-2} \left(1 + \frac{r}{R_M}\right)^{s-4.5} \tag{4.15}$$

where N_e is the electron shower size, r is the distance from the shower axis, and R_M is a transverse scale called the Molière radius described below, is accurate for a shower age $0.5 < s < 1.5$. A variety of transverse distribution functions can be found in the literature (Greisen, Greisen–Linsley, etc.) and are mostly specific modifications of the NKG function.

In a crude approximation, one can assume the transverse dimension of the shower to be dictated by the Molière radius:

$$R_M \simeq \frac{21\,\mathrm{MeV}}{E_c} X_0 \,.$$

About 90% of the shower energy is deposited in a cylinder of radius R_M; about 95% is contained in a radius of $2R_M$, and about 99% in a radius of $3R_M$. In air at NTP, $R_M \simeq 80\,\mathrm{m}$; in water $R_M \simeq 9\,\mathrm{cm}$.

4.1.8 Hadronic Showers

The concept of hadronic showers is similar to the concept of electromagnetic showers: primary hadrons can undergo a sequence of interactions and decays creating a cascade. However, on top of electromagnetic interactions one has now nuclear reactions. In addition, in hadronic collisions with the nuclei of the material, a significant part of the primary energy is consumed in the nuclear processes (excitation, emission of low-energy nucleons, etc.). One thus needs *ad hoc* Monte Carlo corrections to account for the energy lost, and fluctuations are larger. The development of appropriate Monte Carlo codes for hadronic interactions has been a problem in itself, and still the calculation requires huge computational "loads." At the end of a hadronic cascade, most of the particles are pions, and one-third of the pions are neutral and decay almost instantaneously ($\tau \sim 10^{-16}\,\mathrm{s}$) into a pair of photons; thus on average one third of the hadronic cascade is indeed electromagnetic (and the fraction of energy detected in electromagnetic form is larger, since roughly three quarters of

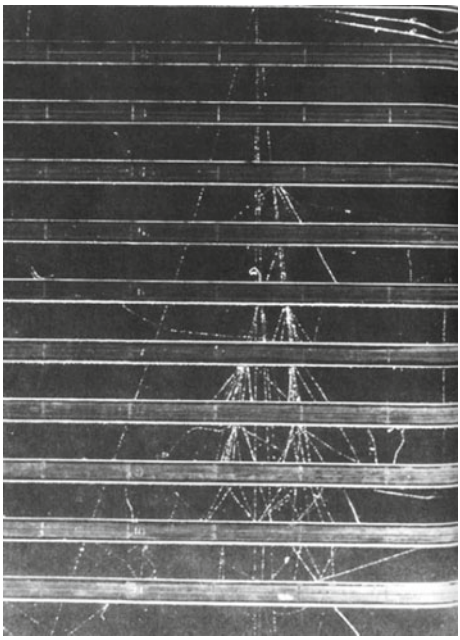

Fig. 4.13 Image of a hadronic shower developing through a number of brass plates 1.25 cm thick placed across a cloud chamber (from B. Rossi, "Cosmic rays," McGraw-Hill 1964). To be compared to Fig. 4.10, right

the energy of charged pions is "wasted" into neutrinos). As an example, the image of a hadronic shower in a cloud chamber is shown in Fig. 4.13.

To a first approximation, the development of the shower can be described by the inelastic hadronic interaction length λ_H; however, the approximation is less accurate than the one we did when we assumed electromagnetic reactions to scale with the radiation length X_0, and intrinsic fluctuations are larger.

4.2 Particle Detectors

The aim of a particle detector is to measure the momenta and to identify the particles that pass through it after being produced in a collision or a decay; this is called an "event." The position in space where the event occurs is known as the interaction point.

In order to identify every particle produced by the collision, and plot the paths they have taken—i.e., to "completely reconstruct the event"—it is necessary to know the masses and momenta of the particles themselves. The mass can be computed by measuring the momentum and either the velocity or the energy.

The characteristics of the different instruments that allow for these measurements are presented in what follows.

4.2.1 Track Detectors

A tracking detector reveals the path taken by a charged particle by measurements of sampled points (hits). Momentum measurements can be made by measuring the curvature of the track in a magnetic field, which causes the particle to curve into a spiral orbit with a radius proportional to the momentum of the particle. This requires the determination of the best fit to a helix of the hits (particle fit). For a particle of unit charge

$$p \simeq 0.3 B_{\perp} R \,,$$

where $B_{\perp}$ is the component of the magnetic field perpendicular to the particle velocity, expressed in tesla (which is the order of magnitude of typical fields in detectors), the momentum p is expressed in GeV/c, and R is the radius of curvature (Larmor radius) of the helix in meters.

A source of uncertainty for this determination is given by the errors in the measurement of the hits; another (intrinsic) noise is given by multiple scattering. In what follows we shall review some detectors used to determine the trajectory of charged tracks.

4.2.1.1 Cloud Chamber and Bubble Chamber

The cloud chamber was invented by C.T.R. Wilson in the beginning of the twentieth century and was used as a detector for reconstructing the trajectories of charged cosmic rays. The instrument, already discussed in the previous chapter, is a container with a glass window, filled with air and saturated water vapor (Fig. 3.8); the volume can be suddenly expanded, and the adiabatic expansion causes the temperature to decrease, bringing the vapor to a supersaturated (metastable) state. A charged particle crossing the chamber produces ions, which act as seeds for the generation of droplets along the trajectory. One can record the trajectory by taking a photographic picture. If the chamber is immersed in a magnetic field B, momentum and charge can be measured by the curvature.

The working principle of bubble chambers[7] (Fig. 4.14) is similar to that of the cloud chamber, but here the fluid is a liquid. Along the trajectory of the particle, a trail of gas bubbles evaporates around the ions.

Due to the higher density of liquids compared with gases, the interaction probability is larger for bubble chambers than for gas chambers, and bubble chambers act at the same time both as an effective target and as a detector. Different liquids

[7]Donald A. Glaser (Cleveland, Ohio, 1926 – Berkeley, California, 2013) was awarded the Nobel Prize in Physics 1960 "for the invention of the bubble chamber". After the Nobel Prize, since he felt that as the experiments grew larger in scale and cost, he was doing more administrative work, and that the ever-more-complex equipment was causing consolidation into fewer sites and requiring more travel for physicists working in high-energy physics, he began to study molecular biology. As molecular biology became more dependent on biochemistry, Glaser again considered a career change, and moved to neurobiology.

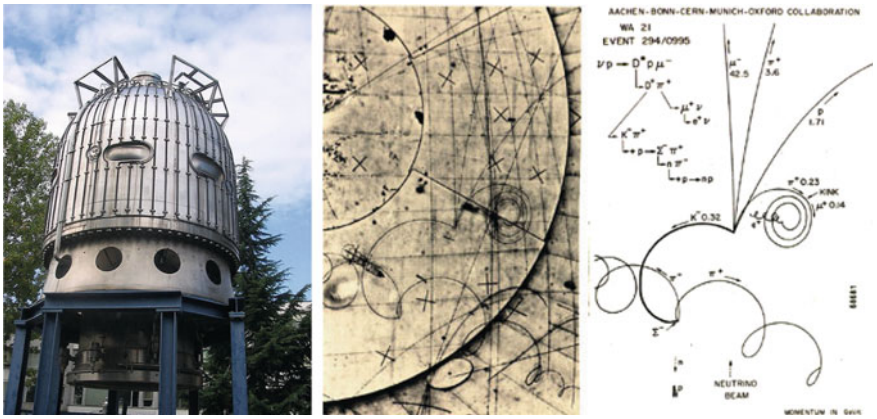

Fig. 4.14 Left: The BEBC bubble chamber. Center: A picture taken in BEBC, and right: its interpretation. Credits: CERN

can be used, depending on the type of experiment: hydrogen to have protons as a target nucleus, deuterium to study interactions on neutrons, etc. From 1950 to the mid-1980s, before the advent of electronic detectors, bubble chambers were the reference tracking detectors. Very large chambers were built (the Big European Bubble Chamber BEBC now displayed at the entrance of the CERN exhibition is a cylinder with an active volume of 35 cubic meters), and wonderful pictures were recorded.

Bubble and cloud chambers provide a complete information: the measurement of the bubble density (their number per unit length) provides an estimate of the specific ionization energy loss dE/dx, hence $\beta\gamma = p/Mc$; the range, i.e., the total track length before the particle eventually stops (if the stopping point is recorded), provides an estimate for the initial energy; the multiple scattering (see below) provides an estimate for the momentum.

A weak point of cloud and bubble chambers is their dead time: after an expansion, the fluid must be re-compressed. This might take a time ranging from about 50 ms for small chambers (LEBC, the LExan Bubble Chamber, used in the beginning of the 1980s for the study of the production and decay of particles containing the quark charm, had an active volume of less than a liter) to several seconds. Due to this limitation and to the labor-consuming visual scanning of the photographs, bubble chambers were abandoned in the mid-1980s—cloud chambers had been abandoned much earlier.

4.2.1.2 Nuclear Emulsions

A nuclear emulsion is a photographic plate with a thick emulsion layer and very uniform grain size. Like bubble chambers and cloud chambers they record the tracks of charged particles passing through, by changing the chemical status of grains that

have absorbed photons (which makes them visible after photographic processing). They are compact, have high density, but have the disadvantages that the plates must be developed before the tracks can be observed, and they must be visually examined.

Nuclear emulsion have very good space resolution of the order of about 1 μm. They had great importance in the beginning of cosmic-ray physics, and they are still used in neutrino experiments (where interactions are rare) due to the lower cost per unit of volume compared to semiconductor detectors and to the fact that they are unsurpassed for what concerns to the single-point space resolution. They recently had a revival with the OPERA experiment at the LNGS underground laboratory in Gran Sasso, Italy, detecting the interactions of a beam of muon neutrinos sent from the CERN SPS in Geneva, 730 km away.

4.2.1.3 Ionization Counter, Proportional Counter and Geiger–Müller Counter

These three kinds of detectors have the same principle of operation: they consist of a tube filled with a gas, with a charged metal wire inside (Fig. 4.15). When a charged particle enters the detector, it ionizes the gas, and the ions and the electrons can be collected by the wire and by the walls (the mobility of electrons being larger than the mobility of ions, it is convenient that the wire's potential is positive). The electrical signal of the wire can be amplified and read by means of an amperometer. The voltage V of the wire must be larger than a threshold below which ions and electrons spontaneously recombine.

Depending on the voltage V of the wire, one can have three different regimes (Fig. 4.16):

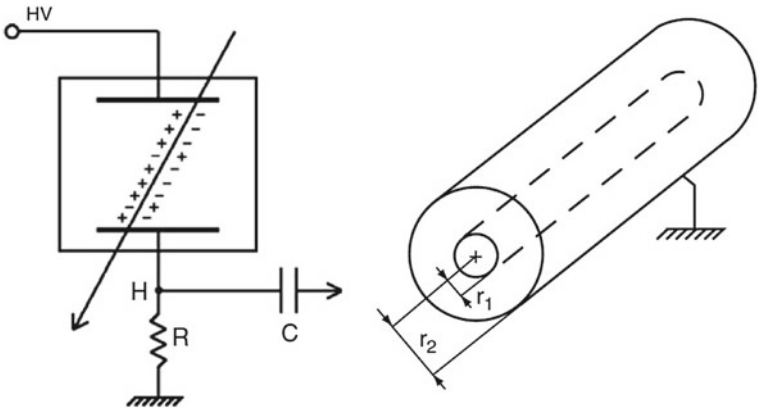

Fig. 4.15 Left: Operational scheme of an ionization chamber. Right: A chamber made in a "tube" shape, using coaxial cylindrical electrodes. From Braibant, Giacomelli and Spurio, "Particles and fundamental interactions," Springer 2014

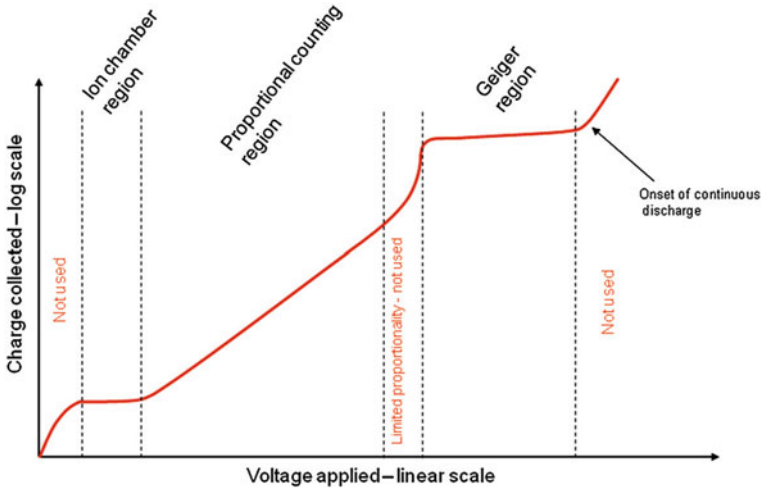

Fig. 4.16 Practical gaseous ionization detector regions: variation of the ion charge with applied voltage in a counter, for a constant incident radiation. By Doug Sim (own work) [CC BY-SA 3.0 http://creativecommons.org/licenses/by-sa/3.0], via Wikimedia Commons

- The ionization chamber regime when $V < I/e$ (I is the ionization energy of the gas, and e the electron charge). The primary ions produced by the track are collected by the wire, and the signal is then proportional to the energy released by the particle.
- The proportional counter regime when $V > I/e$, but V is smaller than a breakdown potential V_{GM} (see below). The ions and the electrons are then accelerated at an energy such that they can ionize the gas. The signal is thus amplified and it generates an avalanche of electrons around the anode. The signal is then proportional to the wire tension.
- Above a potential V_{GM}, the gas is completely ionized; the signal is then a short pulse of height independent of the energy of the particle (Geiger–Müller regime). Geiger–Müller tubes are also appropriate for detecting gamma radiation, since a photoelectron can generate an avalanche.

4.2.1.4 Wire Chamber

The multiwire chamber[8] is basically a sequence of proportional counters. Tubes are replaced by two parallel cathodic planes; the typical distance between the planes is 1–2 cm and the typical distance between the anodic wires is 1 mm (Fig. 4.17).

[8] Jerzy ("Georges") Charpak (1924–2010) was awarded the Nobel Prize in Physics in 1992 "for his invention and development of particle detectors, in particular the multiwire proportional chamber." Charpak was a Polish-born, French physicist. Coming from a Jewish family, he was deported to the Nazi concentration camp in Dachau. After the liberation he studied in Paris and, from 1959, worked at CERN, Geneva.

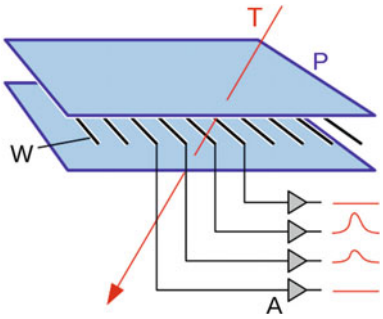

Fig. 4.17 Scheme of a multiwire chamber. By Michael Schmid (own work) [GFDL http://www.gnu.org/copyleft/fdl.html], via Wikimedia Commons

Fig. 4.18 The spark chamber built by LIP (Laboratório de Instrumentação e Partículas, Portugal) for educational purposes records a cosmic ray shower

A charged particle deposits the ionization charge on the closest wire, inducing an electric current; by a sequence of two parallel detectors with the wires aligned perpendicularly one can determine the position of a particle. The typical response time is of the order of 30 ns.

4.2.1.5 Streamer Chamber and Spark Chamber

These are typically multianode (can be multiwire) chambers operating in the Geiger–Müller regime. Short electric pulses of the order of 10 kV/cm are sent between subsequent planes; when a particle passes in the chamber, it can generate a series of discharges which can be visible—a sequence of sparks along the trajectory, Fig. 4.18.

4.2.1.6 Drift Chamber

The drift chamber is a multiwire chamber in which spatial resolution is achieved by measuring the time electrons need to reach the anode wire. This results in wider wire spacing with respect to what can be used in multiwire proportional chambers. Fewer channels have to be equipped with electronics in order to obtain a comparable overall space resolution; in addition, drift chambers are often coupled to high-precision space measurement devices like silicon detectors (see below).

Drift chambers use longer drift distances than multiwire chambers, hence their response can be slower. Since the drift distance can be long and drift velocity needs to be well known, the shape and constancy of the electric field need to be carefully adjusted and controlled. To do this, besides the anode wires (also called "signal" or "sense" wires), thick field-shaping cathode wires called "field wires" are often used.

An extreme case is the time projection chamber (TPC), for which drift lengths can be very large (up to 2 m), and sense wires are arranged at one end; signals in pads or strips near the signal wire plane are used to obtain three-dimensional information.

4.2.1.7 Semiconductor Detectors

Silicon detectors are solid-state particle detectors, whose principle of operation is similar to that of an ionization chamber: the passage of ionizing particles produces in them a number of electron–hole pairs proportional to the energy released. The detector is like a diode (p-n junction) with reverse polarization, the active area being the depleted region. The electron–hole pairs are collected thanks to the electric field, and generate an electrical signal.

The main feature of silicon detectors is the small energy required to create a electron–hole pair—about 3.6 eV, compared with about 30 eV necessary to ionize an atom in an Ar gas ionization chamber.

Furthermore, compared to gaseous detectors, they are characterized by a high density and a high stopping power, much greater than that of the gaseous detectors: they can thus be very thin, typically about 300 μm.

An arrangement of silicon detectors is the so-called microstrip arrangement. A microstrip is a conducting strip separated from a ground plane by a dielectric layer known as the substrate. The general pattern of a silicon microstrip detector is shown in Fig. 4.19. The distance between two adjacent strips, called the pitch, can be of the order of 100 μm, as the width of each strip.

From the signal collected on the strip one can tell if a particle has passed through the detector. The accuracy can be smaller than the size and the pitch: the charge sharing between adjacent strips improves the resolution to some 10 μm. As in the case of multiwire chambers, the usual geometry involves adjacent parallel planes of mutually perpendicular strips.

A recent implementation of semiconductor detectors is the silicon pixel detector. Wafers of silicon are segmented into little squares (pixels) that are as small as 100 μm

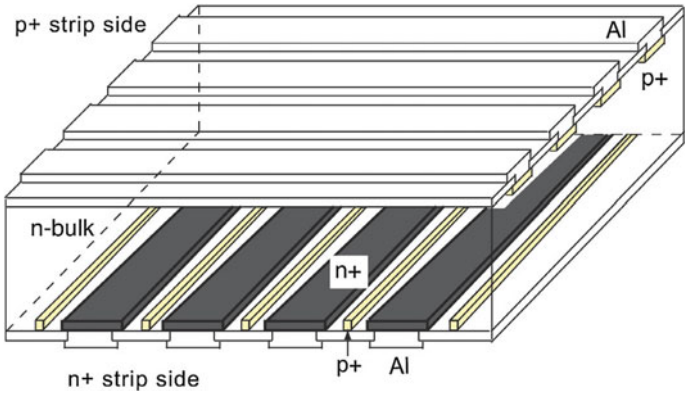

Fig. 4.19 Scheme of a silicon microstrip detector, arranged in a double-side geometry (strips are perpendicular). Source: http://spie.org/x20060.xml

on a side. Electronics is more expensive (however with modern technology it can be bonded to the sensors themselves); the advantage is that one can measure directly the hits without ambiguities.

4.2.1.8 Scintillators

Scintillators are among the oldest particle detectors. They are slabs of transparent material, organic or inorganic; the ionization induces fluorescence, and light is conveyed toward a photosensor (photosensors will be described later). The light yield is large—can be as large as 10^4 photons per MeV of energy deposited—and the time of formation of the signal is very fast, typically less than 1 ns: they are appropriate for trigger[9] systems.

To make the light travel efficiently toward the photosensor (photomultiplier), light guides are frequently used (Fig. 4.20). Sometimes the fluorescence is dominated by low wavelengths; in this case it is appropriate to match the photosensor optical efficiency with a *wavelength shifter* (a material inducing absorption of light and re-emission in an appropriate wavelength).

The scintillators can be used as tracking devices, in the so-called hodoscope configuration (from the Greek "hodos" for path, and "skope" for observation) as in the case of silicon strips. Hodoscopes are characterized by being made up of many detecting planes, made in turn by segments; the combination of which segments record a detection is then used to reconstruct the particle trajectory. Detecting planes can be arranged in pairs of layers. The strips of the two layers should be arranged in perpendicular directions (let us call them horizontal and vertical). A particle passing

[9] A trigger is an electronic system that uses simple criteria to rapidly decide which events in a particle detector to keep in cases where only a small fraction of the total number of events can be recorded.

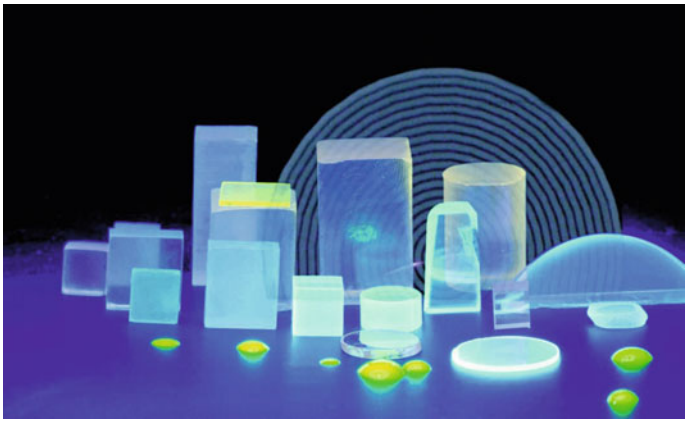

Fig. 4.20 Scintillators. From http://www.tnw.tudelft.nl/fileadmin/Faculteit/TNW

through hits a strip in each layer; the vertical scintillator strip reveals the horizontal position of the particle, and the horizontal strip indicates its vertical position (as in the case of two wire chambers with perpendicular orientation of the wires, but with poorer resolution). Scintillator hodoscopes are among the cheapest detectors for tracking charged particles.

Among scintillators, some are polymeric (plastic); plastic scintillators are particularly important due to their good performance at low price, to their high light output and relatively quick (few ns) signal, and in particular to their ability to be shaped into almost any desired form.

4.2.1.9 Resistive Plate Chambers

The resistive plate chamber (RPC) is a lower-cost alternative to large scintillator planes. An RPC is usually constructed from two parallel high-resistivity glass or melaminic plates with a gap of a few millimeters between them, which is filled with gas at atmospheric pressure. A high potential (of the order of 10 kV) is maintained between the plates.

A charged particle passing through the chamber initiates an electric discharge, whose size and duration are limited by the fact that the current brings the local potential below the minimum required to maintain it. The signal induced is read by metallic strips on both sides of the detector and outside the gas chamber, which are separated from the high voltage coatings by thin insulating sheets.

RPC detectors combine high efficiency (larger than 95%) with excellent time resolution (about 1 ns), and they are therefore a good choice for trigger systems.

Table 4.2 Typical characteristics of different kinds of tracking detectors. Data come from K.A. Olive et al. (Particle Data Group), Chin. Phys. C 38 (2014) 090001

Detector type	Spatial resolution	Time resolution	Dead time
RPC	$\leq$10 mm	$\sim$1 ns (down to $\sim$50 ps)	–
Scintillation counter	10 mm	0.1 ns	10 ns
Emulsion	1 μm	–	–
Bubble chamber	10–100 μm	1 ms	50 ms–1 s
Proportional chamber	50–100 μm	2 ns	20–200 ns
Drift chamber	50–100 μm	few ns	20–200 ns
Silicon strip	Pitch/5 (few μm)	few ns	50 ns
Silicon pixel	10 μm	few ns	50 ns

4.2.1.10 Comparison of the Performance of Tracking Detectors

The main characteristics of tracking detectors are summarized in Table 4.2.

4.2.2 Photosensors

Most detectors in particle physics and astrophysics rely on the detection of photons near the visible range, i.e., in the eV energy range. This range covers scintillation and Cherenkov radiation as well as the light detected in many astronomical observations.

Essentially, one needs to extract a measurable signal from a (usually very small) number of incident photons. This goal can be achieved with the generation of a primary photoelectron or electron–hole pair by an incident photon (typically via photoelectric effect), amplifying the signal to a detectable level (usually by a sequence of avalanche processes), and collecting the secondary charges to form the electrical signal.

The important characteristics of a photodetector include:

- the quantum efficiency QE, namely the probability that a primary photon generates a photoelectron;
- the collection efficiency C related to the overall acceptance;
- the gain G, i.e., the number of electrons collected for each photoelectron generated;
- the dark noise DN, i.e., the electrical signal when there is no incoming photon;
- the intrinsic response time of the detector.

Several kinds of photosensor are used in experiments.

4.2.2.1 Photomultiplier Tubes

Photomultiplier tubes (photomultipliers or PMTs) are detectors of light in the ultraviolet, visible, and near-infrared regions of the electromagnetic spectrum; they are the oldest photon detectors used in high-energy particle and astroparticle physics.

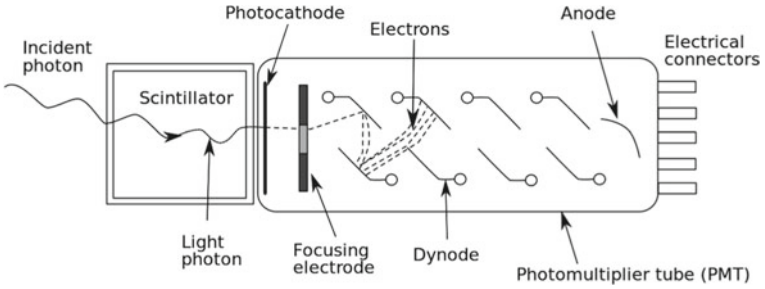

Fig. 4.21 Scheme of a photomultiplier attached to a scintillator. Source: Colin Eberhardt [public domain], via Wikimedia Commons

They are constructed (Fig. 4.21) from a glass envelope with a high vacuum inside, housing a photocathode, several intermediate electrodes called dynodes, and an anode. As incident photons hit the photocathode material (a thin deposit on the entrance window of the device) electrons are produced by photoelectric effect and directed by the focusing electrode toward the electron multiplier chain, where they are multiplied by secondary emission.

The electron multiplier consists of several dynodes, each held at a higher positive voltage than the previous one (the typical total voltage in the avalanche process being of 1–2 kV). The electrons produced in the photocathode have the energy of the incoming photon (minus the work function of the photocathode, i.e., the energy needed to extract the electron itself from the metal, which typically amounts to a few eV). As the electrons enter the multiplier chain, they are accelerated by the electric field. They hit the first dynode with an already much higher energy. Low-energy electrons are then emitted, which in turn are accelerated toward the second dynode. The dynode chain is arranged in such a way that an increasing number of electrons are produced at each stage. When the electrons finally reach the anode, the accumulation of charge results in a sharp current pulse. This is the result of the arrival of a photon at the photocathode.

Photocathodes can be made of a variety of materials with different properties. Typically materials with a low work function are chosen.

The typical quantum efficiency of a photomultiplier is about 30% in the range from 300 to 800 nm of wavelength for the light, and the gain G is in the range 10^5–10^6.

A recent improvement to the photomultiplier was obtained thanks to hybrid photon detectors (HPD), in which a vacuum PMT is coupled to a silicon sensor. A photoelectron ejected from the photocathode is accelerated through a potential difference of about $V \simeq 20\,\text{kV}$ before it hits a silicon sensor/anode. The number of electron–hole pairs that can be created in a single acceleration step is $G \sim V/(3.6\,\text{V})$, the denominator being the mean voltage required to create an electron–hole pair. The linear behavior of the gain is helpful because, unlike exponential gain devices, high voltage stability translates in gain stability. HPD detectors can work as single-photon counters.

4.2.2.2 Gaseous Photon Detectors

In gaseous photomultipliers (GPM) a photoelectron entering a suitably chosen gas mixture (a gas with low photoionization work function, like the tetra dimethylamine ethylene (TMAE)) starts an avalanche in a high-field region. Similarly to what happens in gaseous tracking detectors, a large number of secondary ionization electrons are produced and collected.

Since GPMs can have a good space resolution and can be made into flat panels to cover large areas, they are often used as position-sensitive photon detectors. Many of the ring-imaging Cherenkov (RICH) detectors (see later) use GPM as sensors.

4.2.2.3 Solid-State Photon Detectors

Semiconductor photodiodes were developed during World War II, approximately at the same time photomultiplier tubes became a commercial product. Only in recent years, however, a technique which allows the Geiger-mode avalanche in silicon was engineered, and the semiconductor photodetectors reached sensitivities comparable to photomultiplier tubes. Solid-state photodetectors (often called SiPM) are more compact, lightweight, and they might become cheaper than traditional PMTs in the near future. They also allow fine pixelization, of the order of $1\,\text{mm} \times 1\,\text{mm}$, are easy to integrate in large systems and can operate at low electric potentials.

One of the recent developments in the field was the construction of large arrays of tiny avalanche photodiodes (APD) packed over a small area and operated in Geiger mode.

The main advantages of SiPM with respect to the standard PMT are compact size, low power consumption, low operating voltage (less than 100 V), and immunity to electromagnetic field. The main disadvantages of SiPM are dark current caused by thermally generated avalanches even in the absence of an incoming photon, cross talk between different channels, and the dependence of gain on temperature, of the order of 1% per kelvin at standard temperatures (temperature needs thus to be stabilized, or at least monitored).

4.2.3 Cherenkov Detectors

The main ingredients of Cherenkov detectors are a medium to produce Cherenkov radiation (usually called the radiator) and a system of photodetectors to detect Cherenkov photons. The yield of Cherenkov radiation is usually generous so as to make these detectors perform well.

If one does not need particle identification, a cheap medium (radiator) with large refractive index n can be used so to have a threshold for the emission as low as possible. A typical radiator is water, with $n \simeq 1.33$. The IceCube detector in Antarctica uses ice as a radiator (the photomultipliers are embedded in the ice).

Since the photon yield and the emission angle depend on the mass of the particle, some Cherenkov detectors are also used for particle identification.

Threshold Cherenkov detectors make a yes/no decision based on whether a particle velocity is or not above the Cherenkov threshold velocity c/n—this depends exclusively on the velocity and, if the momentum has been measured, provides a threshold measurement of the value of the mass. A more advanced version uses the number of detected photoelectrons to discriminate between particle species.

Imaging Cherenkov detectors measure the ring-correlated angles of emission of the individual Cherenkov photons. Low-energy photon detectors measure the position (and sometimes the arrival time) of each photon. These must then be "imaged" onto a detector so that the emission angles can be derived. Typically the optics maps the Cherenkov cone onto (a portion of) a conical section at the photodetector.

Among imaging detectors, in the so-called ring-imaging Cherenkov (RICH) detectors, the Cherenkov light cone produced by the passage of a high-speed charged particle in a suitable gaseous or liquid radiator is detected on a position-sensitive planar photon detector. This allows for the reconstruction of a conical section (can be a ring), and its parameters give a measurement of the Cherenkov emission angle (Fig. 4.22). Both focusing and proximity-focusing detectors are used. In focusing detectors, photons are collected by a parabolic mirror and focused onto a photon detector at the focal plane. The result is a conic section (a circle for normal incidence); it can be demonstrated that the radius of the circle is independent of the emission point along the particle track. This scheme is suitable for low refractive index radiators such as gases, due to the large radiator length needed to accumulate enough photons. In proximity-focusing detectors, more compact, the Cherenkov light emitted in a thin volume traverses a short distance (the proximity gap) and is detected in the photon detector plane. The image is a ring of light, with radius defined by the Cherenkov emission angle and the proximity gap.

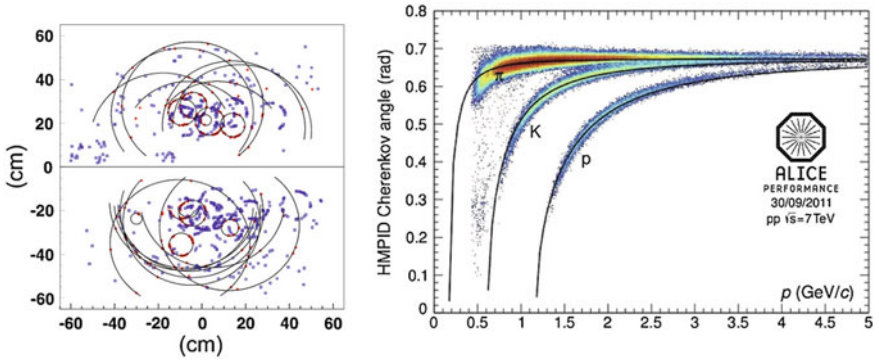

Fig. 4.22 Left: Image of the hits on the photon detectors of the RICHs of the LHCb experiment at CERN with superimposed rings. Credit: LHCb collaboration. Right: Dependence of the Cherenkov angle measured by the RICH of the ALICE experiment at CERN on the particle momentum; the angle can be used to measure the mass through Eq. 4.6 ($\beta = p/E$). Credit: ALICE Collaboration

Atmospheric Cherenkov telescopes for high-energy γ astrophysics are also in use. If one uses a parabolic telescope, again the projection of the Cherenkov emission by a particle along its trajectory is a conical section in the focal plane. If the particle has generated through a multiplicative cascade a shower of secondary particles (see later), the projection is a spot, whose shape can enable us to distinguish whether the primary particle was a hadron or an electromagnetic particle (electron, positron, or photon).

4.2.4 Transition Radiation Detectors

Similar to Cherenkov detectors, transition radiation detectors (TRD) couple interfaces between different media (used as radiators) to photon detectors. Thin foils of lithium, polyethylene, or carbon are common; randomly spaced radiators are also in use, like foams. The main problem in the TRD is the low number of photons. In order to intensify the photon flux, periodic arrangements of a large number of foils are used, interleaved with X-ray detectors such as multiwire proportional chambers filled with xenon or a Xe/CO_2 mixture.

4.2.5 Calorimeters

Once entering an absorbing medium, particles undergo successive interactions and decays, until their energy is degraded, as we have seen in Sect. 4.1.7. Calorimeters are blocks of matter in which the energy of a particle is measured through the absorption to the level of detectable atomic ionizations and excitations. Such detectors can be used to measure not only the energy, but also the position in space, the direction, and in some cases the nature of the particle.

4.2.5.1 Electromagnetic Calorimeters

An ideal material used for an electromagnetic calorimeter—a calorimeter especially sensitive to electrons/positrons and photons—should have a short radiation length, so that one can contain the electromagnetic shower in a compact detector, and the signal should travel unimpeded through the absorber (homogeneous calorimeters). However, sometimes materials which can be good converters and conductors of the signals are very expensive: one then uses *sampling* calorimeters, where the degraded energy is measured in a number of sensitive layers separated by passive absorbers.

The performance of calorimeters is limited both by the unavoidable fluctuations of the elementary phenomena through which the energy is degraded and by the technique chosen to measure the final products of the cascade processes.

Homogeneous Calorimeters. Homogeneous calorimeters may be built with heavy (high density, high Z) scintillating crystals, i.e., crystals in which ionization energy loss results in the emission of visible light, or Cherenkov radiators such as lead glass and lead fluoride. The material acts as a medium for the development of the shower, as a transducer of the electron signal into photons, and as a light guide toward the photodetector. Scintillation light and/or ionization can be detected also in noble liquids.

Sampling Calorimeters. Layers of absorbers are typically interspersed with layers of active material (sandwich geometry). The absorber helps the development of the electromagnetic shower, while the active material transforms part of the energy into photons, which are guided toward the photodetector. Different geometries can be used: for example, sometimes rods of active material cross the absorber (spaghetti geometry).

Converters have high density, short radiation length. Typical materials are iron (Fe), lead (Pb), uranium, tungsten (W). Typical active materials are plastic scintillator, silicon, liquid ionization chamber gas detectors.

Disadvantages of sampling calorimeters are that only part of the deposited particle energy is detected in the active layers, typically a few percent (and even one or two orders of magnitude less in the case of gaseous detectors). Sampling fluctuations typically result in a worse energy resolution for sampling calorimeters.

Electromagnetic Calorimeters: Comparison of the Performance. The fractional energy resolution $\Delta E/E$ of a calorimeter can be parameterized as

$$\frac{\Delta E}{E} = \frac{a}{\sqrt{E}} \oplus b \oplus \frac{c}{E},$$

where the symbol $\oplus$ represents addition in quadrature. The stochastic term a originates from statistics-related effects such as the intrinsic fluctuations in the shower, number of photoelectrons, dead material in front of the calorimeter, and sampling fluctuations—we remind that the number of particles is roughly proportional to the energy, and thus the Poisson statistics gives fluctuations proportional to $\sqrt{E}$. The a term is at a few percent level for a homogeneous calorimeter and typically 10% for sampling calorimeters. The systematic or constant b term represents contributions from the detector nonuniformity and calibration uncertainty, and from incomplete containment of the shower. In the case of hadronic cascades (discussed below), the different response of the instrument to hadrons and leptons, called noncompensation, also contributes to the constant term. The constant term b can be reduced to below one percent. The c term is due to electronic noise. Some of the above terms can be negligible in calorimeters.

The best energy resolution for electromagnetic shower measurement is obtained with total absorption, homogeneous calorimeters, such as those built with heavy crystal scintillators like $Bi_4Ge_3O_{12}$, called BGO. They are used when optimal performance is required. A relatively cheap scintillator with relatively short X_0 is the cesium iodide (CsI), which becomes more luminescent when activated with thallium,

Table 4.3 Main characteristics of some electromagnetic calorimeters. Data from K.A. Olive et al. (Particle Data Group), Chin. Phys. C 38 (2014) 090001. The accelerators quoted in the table are discussed in the next section

Technology (experiment)	Depth (X_0)	Energy resolution (relative)
BGO (L3 at LEP)	22	$2\%/\sqrt{E} \oplus 0.7\%$
CsI (kTeV at the FNAL K beam)	27	$2\%/\sqrt{E} \oplus 0.45\%$
$PbWO_4$ (CMS at LHC)	25	$3\%/\sqrt{E} \oplus 0.5\% \oplus 0.2\%/E$
Lead glass (DELPHI, OPAL at LEP)	20	$5\%/\sqrt{E}$
Scintillator/Pb (CDF at the Tevatron)	18	$18.5\%/\sqrt{E}$
Liquid Ar/Pb (SLD at SLC)	21	$12\%/\sqrt{E}$

and is called CsI(Tl); this is frequently used for dosimetry in medical applications, and in space applications, where high technological readiness and reliability are needed.

Energy resolutions for some homogeneous and sampling calorimeters are listed in Table 4.3.

4.2.5.2 Hadronic Calorimeters

We have examined the main characteristics of hadronic showers in Sect. 4.1.8.

Detectors capable of absorbing hadrons and detecting a signal were developed around 1950 for the measurement of the energy of cosmic rays. It can be assumed that the energy of the incident particle is proportional to the multiplicity of charged particles.

Most large hadron calorimeters are sampling calorimeters installed as part of complex detectors at accelerator experiments. The basic structure typically consists of absorber plates (Fe, Pb, Cu, or occasionally U or W) alternating with plastic scintillators (shaped as plates, tiles, bars), liquid argon (LAr) chambers, or gaseous detectors (Fig. 4.23). The ionization is measured directly, as in LAr calorimeters, or via scintillation light observed in photodetectors (usually photomultipliers).

The fluctuations in the invisible energy and in the hadronic component of a shower affect the resolution of hadron calorimeters.

A hadron with energy E generates a cascade in which there are repeated hadronic collisions. In each of these, neutral pions are also produced, which immediately ($\tau \sim 0.1$ fs) decay into photons: a fraction of the energy is converted to a potentially observable signal with an efficiency which is in general different, usually larger, than the hadronic detection efficiency. The response of the calorimeters to hadrons is thus not compensated with respect to the response to electromagnetic particles (or to the electromagnetic part of the hadronic shower).

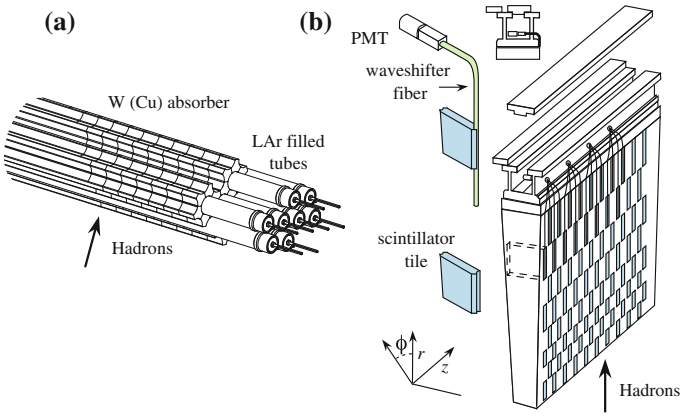

Fig. 4.23 Hadronic calorimeters of the ATLAS experiments at LHC. Credit: CERN

Due to all these problems, typical fractional energy resolutions are in the order of $30–50\%/\sqrt{E}$.

What is the difference between electromagnetic and hadronic calorimeters? Electromagnetic calorimeters are designed to stop photons and electrons and prevent the electromagnetic shower from leaking into the hadronic calorimeter, which in complex detectors is normally located downstream the electromagnetic calorimeter. Many hadrons still lose most of their energy in the electromagnetic calorimeter via strong interactions. Two prerequisites for a good electromagnetic calorimeter are a large Z and a large signal. Due to intrinsic fluctuations of hadronic showers, a hadronic calorimeter, for which large mass number A is the main requirement in order to maximize the hadronic cross section, is less demanding. In principle, however, you can have also a single calorimeter both for "electromagnetic" particles and for hadrons—in this case, cost will be a limitation.

4.3 High-Energy Particles

We have seen that when we use a beam of particles as a microscope, like Rutherford did in his experiment, the minimum distance we can sample (e.g., to probe a possible substructure in matter) decreases with increasing energy. According to de Broglie's equation, the relation between the momentum p and the wavelength λ of a wave packet is given by

$$\lambda = \frac{h}{p}\,.$$

Therefore, larger momenta correspond to shorter wavelengths and allow us to access smaller structures. Particle acceleration is thus a fundamental tool for research in physics.

In addition, we might be interested in using high-energy particles to produce new particles in collisions. This requires more energy, the more massive the particles we want to produce.

4.3.1 Artificial Accelerators

A particle accelerator is an instrument using electromagnetic fields to accelerate charged particles at high energies.

There are two schemes of collision:

- collision with a fixed target (fixed-target experiments);
- collision of a beam with another beam running in the opposite direction (collider experiments).

We also distinguish two main categories of accelerators depending on the geometry: linear accelerators and circular accelerators. In linear accelerators the bremsstrahlung energy loss is much reduced since there is no centripetal acceleration, but particles are wasted after a collision, while in circular accelerators the particles which did not interact can be reused.

The center-of-mass energy E_{CM} sets the scale for the maximum mass of the particles we can produce (the actual value of the available energy being in general smaller due to constraints related to conservation laws).

We want now to compare fixed-target and colliding beam experiments concerning the available energy.

In the case of beam–target collisions between a particle of energy E much larger than its mass, and a target of mass m,

$$E_{\mathrm{CM}} \simeq \sqrt{2mE}\,.$$

This means that, in a fixed-target experiment, the center-of-mass energy grows only with the square root of E. In beam–beam collisions, instead,

$$E_{\mathrm{CM}} = 2E\,.$$

It is therefore much more efficient to use two beams in opposite directions. As a result, most of the recent experiments at accelerators are done at colliders.

Making two beams collide, however, is not trivial: one must control the fact that the beams tend to defocus due to mutual repulsion of the particles. In addition, Liouville's theorem states that the phase space volume (the product of the spread in terms of the space coordinates times the spread in the momentum coordinate) of an isolated beam is constant: reducing the momentum dispersion is done at the expense

of the space dispersion—and one needs small space dispersion in order that the particles in the beam actually collide. Beating Liouville's theorem requires feedback on the beam itself.[10]

Since beams are circulated for several hours, circular accelerators are based on beams of stable particles and antiparticles, such as electrons, protons, and their antiparticles. In the future, muon colliders are an interesting candidate: as "clean" as electrons, since they are not sensitive to the hadronic interaction, muons have a lower energy dissipation (due to synchrotron radiation and bremsstrahlung) thanks to their mass being 200 times larger than electrons.

Particle accelerators and detectors are often situated underground in order to provide the maximal shielding possible from natural radiation such as cosmic rays that would otherwise mask the events taking place inside the detector.

4.3.1.1 Acceleration Methods

A particle of charge q and speed $\mathbf{v}$ in an electric field $\boldsymbol{\mathcal{E}}$ and a magnetic field $\mathbf{B}$ feels a force

$$\mathbf{F} = q(\boldsymbol{\mathcal{E}} + \mathbf{v} \times \mathbf{B}) \,.$$

The electric field can thus accelerate the particle. The work by the magnetic field is zero; nevertheless the magnetic field can be used to control the particle's trajectory. For example, a magnetic field perpendicular to $\mathbf{v}$ can constrain the particle along a circular trajectory perpendicular to $\mathbf{B}$.

If a single potential were applied, increasing energy would demand increasing voltages. The solution is to apply multiple times a limited potential.

An acceleration line (which corresponds roughly to a linear accelerator) works as follows. In a beam pipe (a cylindrical tube in which vacuum has been made) cylindrical electrodes are aligned. A pulsed radiofrequency (RF) source of electromotive force V is applied. Thus particles are accelerated when passing in the RF cavity (Fig. 4.24); the period is adjusted in such a way that half of the period corresponds of the time needed for the particle to cross the cavity. The potential between the cylinders is reversed when the particle is located within them.

To have a large number of collisions, it is useful that particles are accelerated in bunches. This introduces an additional problem, since the particles tend to diverge due to mutual electrostatic repulsion. Divergence can be compensated thanks to focusing magnets (e.g., quadrupoles, which squeeze beams in a plane).

A collider consists of two circular or almost circular accelerator structures with vacuum pipes, magnets and accelerating cavities, in which two beams of particles

[10]The Nobel Prize for physics in 1984 was awarded to the Italian physicist Carlo Rubbia (1934–) and to the Dutch engineer Simon van der Meer (1925–2011) "for their decisive contributions to the large project, which led to the discovery of the field particles W and Z, communicators of weak interaction." In short, Rubbia and van der Meer used feedback signals sent in the ring to reduce the entropy of the beam; this technique allowed the accumulation of focalized particles with unprecedented efficiency, and is at the basis of all modern accelerators.

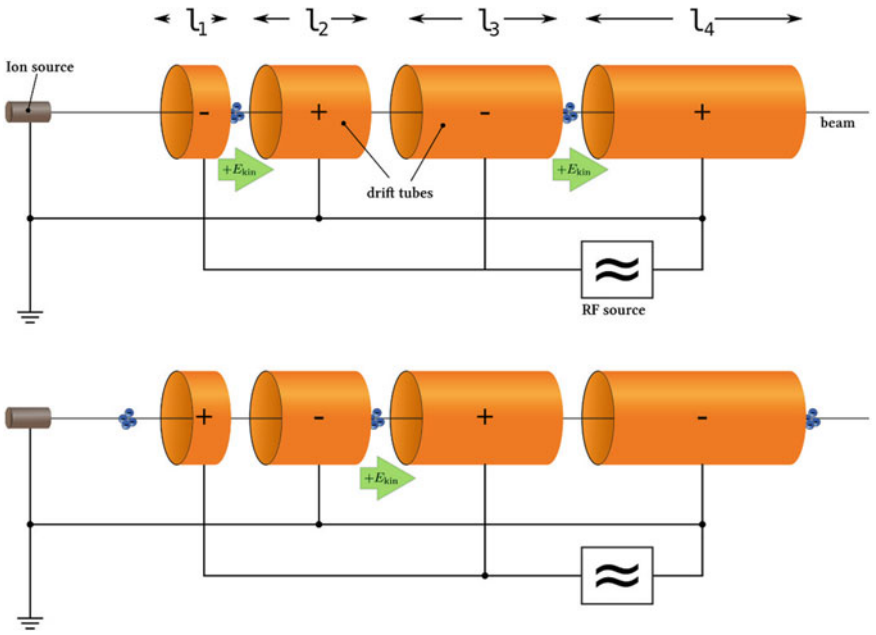

Fig. 4.24 Scheme of an acceleration line displayed at two different times. By Sgbeer (own work) [GFDL http://www.gnu.org/copyleft/fdl.html], via Wikimedia Commons

travel in opposite directions. The particles may be protons in both beams, or protons and antiprotons, or electrons and positrons, or electrons and protons, or also nuclei and nuclei. The two rings intercept each other at a few positions along the circumference, where bunches can cross and particles can interact. In a particle–antiparticle collider (electron–positron or proton–antiproton), as particles and antiparticles have opposite charges and the same mass, a single magnetic structure is sufficient to keep the two beams circulating in opposite directions.

4.3.1.2 Parameters of an Accelerator

An important parameter for an accelerator is the maximum center-of-mass (c.m.) energy $\sqrt{s}$ available, since this sets the maximum mass of new particles that can be produced.

Another important parameter is *luminosity,* already discussed in Chap. 2. Imagine a physical process has a cross section σ_{proc}; the number of outcomes of this process per unit time can be expressed as

$$\frac{dN_{\text{proc}}}{dt} = \frac{dL}{dt}\sigma_{\text{proc}} .$$

dL/dt is called *differential luminosity* of the accelerator, and is measured in $\mathrm{cm}^{-2}\,\mathrm{s}^{-1}$; however, for practical reasons it is customary to use "inverse barns" and its multiples instead of cm^{-2} (careful: due to the definition, $1\ \mathrm{mbarn}^{-1} = 1000\ \mathrm{barn}^{-1}$).

The integrated luminosity can be obtained by integrating the differential luminosity over the time of operation of an accelerator:

$$L = \int_{\text{time of operation}} \frac{dL(t)}{dt} dt\,.$$

In a collider, the luminosity is proportional to the product of the numbers of particles, n_1 and n_2, in the two beams. Notice that in a proton–antiproton collider the number of antiprotons is in general smaller than that of protons, due to the "cost" of the antiprotons (antiprotons are difficult to store and to accumulate, since they easily annihilate). The luminosity is also proportional to the number of crossings in a second f and inversely proportional to the transverse section $\mathcal{A}$ at the intersection point

$$\frac{dL}{dt} = f\frac{n_1 n_2}{\mathcal{A}}\,.$$

4.3.2 Cosmic Rays as Very-High-Energy Beams

As we have already shown, cosmic rays can attain energies much larger than the particles produced at human-made accelerators. The main characteristics of cosmic rays have been explained in Sect. 1.6 and in Chap. 3.

We just recall here that the distribution in energy (the so-called spectrum) of cosmic rays is quite well described by a power law E^{-p}, with the so-called spectral index p around 3 on average (Fig. 1.8), extending up to about 10^{21} eV (above this energy the GZK cutoff, explained in the previous chapters, stops the cosmic travel of particles; a similar mechanism works for heavier nuclei, which undergo photodisintegration during their cosmic travel). The majority of the high-energy particles in cosmic rays are protons (hydrogen nuclei); about 10% are helium nuclei (nuclear physicists call them usually "alpha particles"), and 1% are neutrons or nuclei of heavier elements. These together account for 99% of the cosmic rays, and electrons, photons, and neutrinos dominate the remaining 1%. The number of neutrinos is estimated to be comparable to that of high-energy photons, but it is very high at low energy because of the nuclear processes that occur in the Sun. Cosmic rays hitting the atmosphere (called primary cosmic rays) generally produce secondary particles that can reach the Earth's surface, through multiplicative showers.

The reason why human-made accelerators cannot compete with cosmic accelerators from the point of view of the maximum attainable energy is that with the present technologies acceleration requires confinement within a radius R by a magnetic field B, and the final energy is proportional to R times B. On Earth, it is difficult to imagine reasonable radii of confinement larger than one hundred kilo-

meters and magnetic fields stronger than ten tesla (one hundred thousand times the Earth's magnetic field). This combination can provide energies of a few tens of TeV, such as those of the LHC accelerator at CERN. In nature there are accelerators with much larger radii, as the remnants of supernovae (hundreds of light years) and active galactic nuclei (tens of thousands of light years): one can thus reach energies as large as 10^{21} eV, i.e., 1 ZeV (the so-called extremely high-energy (EHE) cosmic rays; cosmic rays above 10^{18} eV, i.e., 1 EeV, are often called ultrahigh energy, UHE). Of course terrestrial accelerators have great advantages like luminosity and the possibility of knowing the initial conditions.

The conditions are synthetically illustrated in the so-called Hillas plot (Fig. 10.32), a scatter plot in which different cosmic objects are grouped according to their sizes and magnetic fields; this will be discussed in larger detail in Chap. 10. UHE can be reached in the surroundings of active galactic nuclei, or in gamma-ray bursts. R times B in supernova remnants is such that particles can reach energies of some PeV.

4.4 Detector Systems and Experiments at Accelerators

Detectors at experimental facilities are in general hybrid, i.e., they combine many of the detectors discussed so far, such as drift chambers, Cherenkov detectors, electromagnetic, and hadronic calorimeters. They are built up in a sequence of layers, each one designed to measure a specific aspect of the particles produced after the collision.

Starting with the innermost layer, the successive layers are typically as follows:

- A tracking system: this is designed to track all the charged particles and allow for complete event reconstruction. It is in general the first layer crossed by the particles, in such a way that their properties have not yet been deteriorated by the interaction with the material of the detector. It should have as little material as possible, so as to preserve the particles for the subsequent layer.
- A layer devoted to electromagnetic calorimetry.
- A layer devoted to hadronic calorimetry.
- A layer of muon tracking chambers: any particle releasing signal on these tracking detectors (often drift chambers) has necessarily traveled through all the other layers and is very likely a muon (neutrinos have extremely low interaction cross sections, and most probably they cross also the muon chambers without leaving any signal).

A layer containing a solenoid can be inserted after the tracking system, or after the calorimeter. Tracking in a magnetic field allows for momentum measurement.

The particle species can be identified, for example, by energy loss, curvature in magnetic field, and Cherenkov radiation. However, the search for the identity of a particle can be significantly narrowed down by simply examining which parts of the detector it deposits energy in:

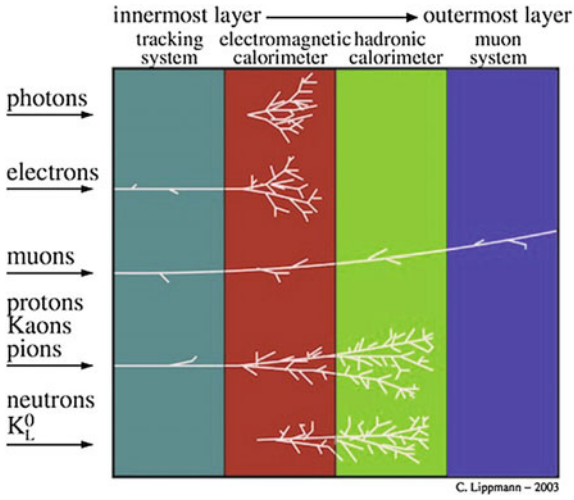

Fig. 4.25 Overview of the signatures by a particle in a multilayer hybrid detector. Credit: CERN

- Photons leave no tracks in the tracking detectors (unless they undergo pair production) but produce a shower in the electromagnetic calorimeter.
- Electrons and positrons leave a track in the tracking detectors and produce a shower in the electromagnetic calorimeter.
- Muons leave tracks in all the detectors (likely as a minimum ionizing particle in the calorimeters).
- Longlived charged hadrons (protons for example) leave tracks in all the detectors up to the hadronic calorimeter where they shower and deposit all their energy.
- Neutrinos are identified by missing energy-momentum when the relevant conservation law is applied to the event.

These signatures are summarized in Fig. 4.25.

4.4.1 Examples of Detectors for Fixed-Target Experiments

In a fixed-target experiment, relativistic effects make the interaction products highly collimated. In such experiments then, in order to enhance the possibility of detection in the small-x_T ($x_T = p_T/\sqrt{s}$, where p_T is the momentum component perpendicular to the beam direction), different stages are separated by magnets opening up the charged particles in the final state (lever arms).

The first detectors along the beam line should be nondestructive; at the end of the beam line, one can have calorimeters. Two examples are given in the following; the first is a fixed-target experiment from the past, while the second is an *almost* fixed-target detector presently operating.

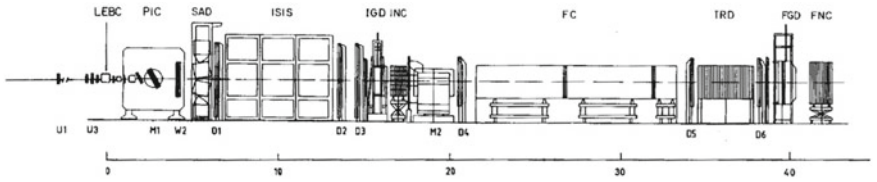

Fig. 4.26 A configuration of the European Hybrid Spectrometer (a fixed-target detector at the CERN Super Proton Synchrotron). From M. Aguilar-Benitez et al., "The European hybrid spectrometer," Nucl. Instr. Methods 258 (1987) 26

4.4.1.1 The European Hybrid Spectrometer at the SPS

The European Hybrid Spectrometer EHS was operational during the 1970s and in the beginning of the 1980s at the North Area of CERN, where beams of protons were extracted from the SPS (Super Proton Synchrotron)[11] accelerator at energies ranging from 300 to 400 GeV. Such particles might possibly generate secondary beams of charged pions of slightly smaller energies by a beam-dump and a velocity selector based on magnetic field. EHS was a multi-stage detector serving different experiments (NA16, NA22, NA23, NA27). Here we describe a typical configuration; Fig. 4.26 shows a schematic drawing of the EHS setup.

In the figure, the beam particles come in from the left. Their direction is determined by the two small wire chambers U1 and U3. From the collision point inside a rapid cycling bubble chamber (RCBC; the previously described LEBC is an example, with a space resolution of 10 μm) most of the particles produced enter the downstream part of the spectrometer.

The RCBC acts both as a target and as a vertex detector. If an event is triggered, stereoscopic pictures are taken with 3 cameras and recorded on film.

The momentum resolution of the secondary particles depends on the number of detector element hits available for the track fits. For low momentum particles, typically $p < 3\,\text{GeV}/c$, length and direction of the momentum vector at the collision point can be well determined from RCBC. On the other hand, tracks with $p > 3\,\text{GeV}/c$ have a very good chance to enter the so-called first lever arm. This is defined by the group of four wire chambers W2, D1, D2, and D3 placed between the two magnets M1 and M2. Very fast particles (typically with momentum $p > 30\,\text{GeV}/c$) will go through the aperture of the magnet M2 to the so-called second lever arm, consisting of the three drift chambers D4, D5, and D6.

To detect gamma rays, two electromagnetic calorimeters are used in EHS, the intermediate gamma detector (IGD) and the forward gamma detector (FGD). IGD is placed before the magnet M2. It has a central hole to allow fast particles to proceed to the second lever arm. FGD covers this hole at the end of the spectrometer. The

[11] A synchrotron is a particle accelerator ring, in which the guiding magnetic field (bending the particles into a closed path) is time dependent and synchronized to a particle beam of increasing kinetic energy. The concept was developed by the Soviet physicist Vladimir Veksler in 1944.

IGD has been designed to measure both the position and the energy of a shower in a two-dimensional matrix of lead-glass counters 5 cm × 5 cm in size, each of them connected to a PMT. The FGD consists of three separate sections. The first section is the converter (a lead-glass wall), to initiate the electromagnetic shower. The second section (the position detector) is a three-plane scintillator hodoscope. The third section is the absorber, a lead-glass matrix deep enough (60 radiation length) to totally absorb showers up to the highest available energies. For both calorimeters, the relative accuracy on energy reconstruction is $\Delta E/E \simeq 0.1/\sqrt{E} \oplus 0.02$.

The spectrometer included also three detectors devoted to particle identification: the silica-aerogel Cherenkov detector (SAD), the ISIS chamber measuring specific ionization, and the transition radiation detector TRD.

4.4.1.2 LHCb at LHC

LHCb ("Large Hadron Collider beauty") is a detector at the Large Hadron Collider accelerator at CERN. LHCb is specialized in the detection of *b*-hadrons (hadrons containing a bottom quark). A sketch of the detector is shown in Fig. 4.27.

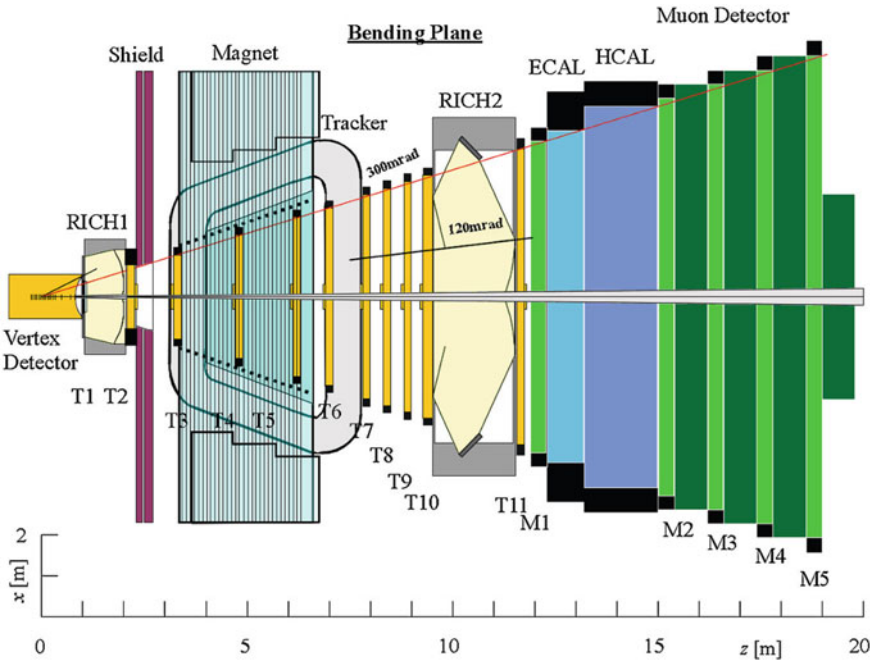

Fig. 4.27 Sketch of the LHCb detector. Credit: CERN

Although, in strict terms, LHCb is a colliding beam experiment, it is done as a fixed-target one: the strongly boosted *b*-hadrons fly along the beam direction, and one side is instrumented.

At the heart of the detector is the vertex detector, recording the decays of the *b* particles, which have typical lifetimes of about 1 ps and will travel only about 10 mm before decaying. It has 17 planes of silicon (radius 6 cm) spaced over a meter and consisting of two disks (in order to measure radial and polar coordinates) and provides a hit resolution of about 10 and 40 μm for the impact parameter of high momentum tracks.

Downstream of the vertex detector, the tracking system (made of 11 tracking chambers) reconstructs the trajectories of emerging particles. LHCb's 1.1 T superconducting dipole spectrometer magnet (inherited from the DELPHI detector at LEP, see later) opens up the tracks.

Particle identification is performed by two ring-imaging Cherenkov (RICH) detector stations. The first RICH is located just behind the vertex detector and equipped with a 5 cm silica aerogel and 1 m C_4F_{10} gas radiators, while the second one consists of 2 m of CF_4 gas radiator behind the tracker. Cherenkov photons are picked up by a hybrid photodiode array.

The electromagnetic calorimeter, installed following the second RICH, is a "shashlik" structure of scintillator and lead read out by wavelength-shifting fibers. It has three annular regions with different granularities in order to optimize readout. A lead-scintillator preshower detector improves electromagnetic particle identification.

The hadron calorimeter is made of scintillator tiles embedded in iron. Like the electromagnetic calorimeter upstream, it has three zones of granularity. Downstream, shielded by the calorimetry, are four layers of muon detectors. These are multigap resistive plate chambers and cathode pad chambers embedded in iron, with an additional layer of cathode pad chambers mounted before the calorimeters. Besides muon identification, this provides important input for triggering.

There are four levels of triggering. The initial (level 0) decisions are based on a high transverse momentum particle and use the calorimeters and muon detectors. This reduces by a factor of 40 the 40 MHz input rate. The next trigger level (level 1) is based on vertex detector (to look for secondary vertices) and tracking information, and reduces the data by a factor of 25 to an output rate of 40 kHz. Level 2, suppressing fake secondary decay vertices, achieves further eightfold compression. Level 3 reconstructs *B* decays to select specific decay channels, achieving another compression factor of 25. Data are written to tape at 200 Hz.

4.4.2 Examples of Detectors for Colliders

The modern particle detectors in use today at colliders are as much as possible hermetic detectors. They are designed to cover most of the solid angle around the interaction point (a limitation being given by the presence of the beam pipe). The

typical detector consists of a cylindrical section covering the "barrel" region and two endcaps covering the "forward" regions.

In the standard coordinate system, the z axis is along the beam direction, the x axis points toward the center of the ring, and the y axis points upwards. The polar angle to the z axis is called θ and the azimuthal angle is called ϕ; the radial coordinate is $R = \sqrt{x^2 + y^2}$.

Frequently the polar angle is replaced by a coordinate called *pseudorapidity* η and defined as

$$\eta = \ln \left[\tan \left(\frac{\theta}{2} \right) \right] ;$$

the region $\eta \simeq 0$ corresponds to $\theta \simeq \pi/2$, and is called the central region. When in Chap. 6 we shall discuss the theory of hadronic interactions, quantum chromodynamics, we shall clarify the physical significance of this variable.

The detector has the typical onion-like structure described in the previous section: a sequence of layers, the innermost being the most precise for tracking.

The configuration of the endcaps is similar to that in a fixed-target experiment except for the necessary presence of a beam pipe, which makes it impossible to detect particles at very small polar angles, and entails the possible production of secondary particles in the pipe wall.

In the following sections we shall briefly describe three generations of collider detectors operating at the European Organization for Particle Physics, CERN: UA1 at the S$p\bar{p}$S $p\bar{p}$ accelerator, DELPHI at the LEP e^+e^- accelerator, and the main detectors at the LHC pp accelerator: CMS and ATLAS. We shall see how much the technology developed and the required labor increased; the basic ideas are anyway still common to the prototype detector, UA1.

4.4.2.1 UA1 at the S$p\bar{p}$S

The UA1 experiment, named as the first experiment in the CERN Underground Area (UA), was operating at CERN's S$p\bar{p}$S (Super proton–antiproton Synchrotron) accelerator–collider from 1981 till 1993. The discovery of the W and Z bosons, mediators of the weak interaction, by this experiment in 1983, led to the Nobel Prize for physics to Carlo Rubbia and Simon van der Meer in 1984 (the motivation of the prize being more related to the development of the collider technology). The S$p\bar{p}$S was colliding protons and antiprotons at a typical c.m. energy of 540 GeV; three bunches of protons and three bunches of antiprotons, 10^{11} particles per bunch, were present in the ring at the same time, and the luminosity was about $5 \times 10^{27}\,\mathrm{cm}^{-2}/\mathrm{s}$ (5 inverse millibarn per second).

UA1 was a huge and complex detector for its days, and it has been the prototype of collider detectors. The collaboration constructing and managing the detector included approximately 130 scientists from all around the world.

UA1 was a general-purpose detector. The central tracking system was an assembly of six drift chambers 5.8 m long and 2.3 m in diameter. It recorded the tracks of

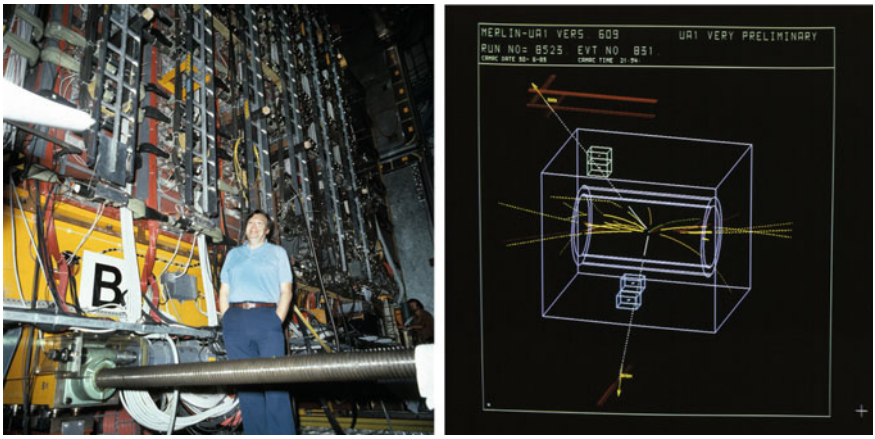

Fig. 4.28 Left: The UA1 detector, and Carlo Rubbia. Right: A Z boson decaying into a muon–antimuon pair as seen at the event display of UA1 (Source: CERN)

charged particles curving in a 0.7 T magnetic field, measuring their momenta with typical accuracy $\delta p/p \simeq 0.01 p_T$ (where p_T is the momentum component transverse to the beam axis, also called the transverse momentum[12]; p is expressed in GeV/c) and possibly identifying them by the specific energy loss dE/dx. The geometrical arrangement of the approximately 17 000 field wires and 6125 sense wires allowed a three-dimensional reconstruction of events. UA1 introduced also the concept of event display (Fig. 4.28).

After the tracking chamber and an air gap of 0.5 m, the particles next encountered the calorimeter plus 60 cm of additional iron shielding, including the magnet yoke. The calorimeter started with an electromagnetic calorimeter made of a sandwich of lead and scintillator, with a total relative energy resolution about $0.2/\sqrt{E}$. The iron shielding was partially instrumented with streamer tubes[13] measuring the position and the number of minimum ionizing particles, and thus, acting as a hadronic calorimeter with relative energy resolution about $0.8/\sqrt{E}$. Together, the calorimeter and the shielding corresponded to more than eight interaction lengths of material, which almost completely absorbed strongly interacting particles. Finally, muons were detected in the outer muon chambers, which covered about 75% of the solid angle in the pseudorapidity range $|\eta| < 2.3$. Muon trigger processors required tracks in the muon chambers pointing back to the interaction region to retain an event as significant.

[12] Being proportional to $(1/p_T)$ the fitted quantity by means of the radius of curvature, the accuracy on the momentum measurement can be parameterized as $\delta(1/p_T) = \delta(p)/(p_T p) \sim$ constant.

[13] Limited streamer tubes, often simply called streamer tubes, are made of a resistive cathode in the form of a round or square tube, with a thick (0.1 mm) anode wire in its axis; they operate at voltages close to the breakdown (see Sect. 4.2.1.3). Such detectors can be produced with 1–2 cm diameter, and they are cheap and robust.

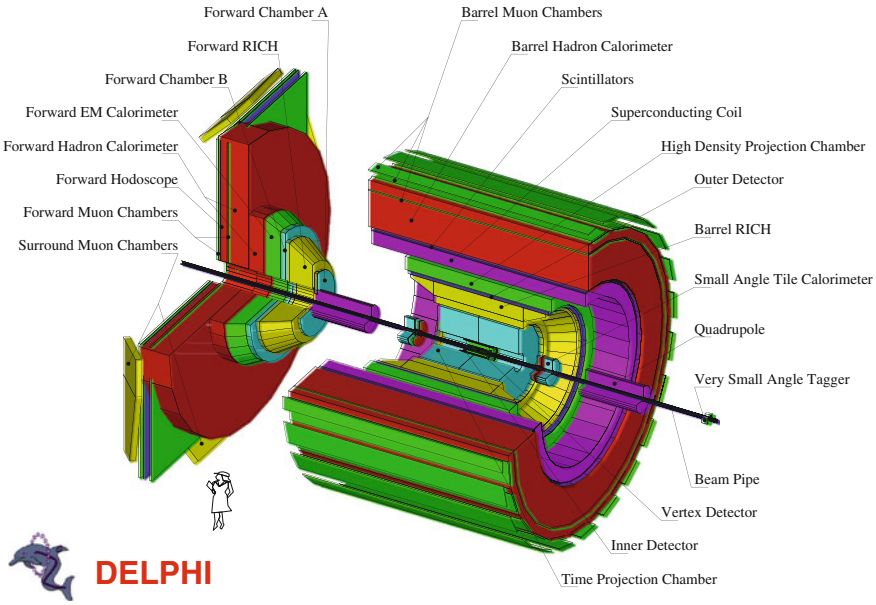

Fig. 4.29 The DELPHI detector at LEP. Source: CERN

4.4.2.2 DELPHI at LEP

DELPHI (DEtector with Lepton Photon and Hadron Identification, Fig. 4.29) was one of the four experiments built for the LEP (Large Electron–Positron) collider at CERN. The main aim of the experiment was the verification of the theory known as the standard model of particle physics. DELPHI started collecting data in 1989 and ran for about 8 months/year, 24 h a day, until the end of 2000; it recorded the products of collisions of electrons and positrons at c.m. energies from 80 to 209 GeV (most of the data being taken at the Z peak, around 91.2 GeV). Typical luminosity was 2×10^{31} cm^{-2}/s (20 inverse microbarn per second). DELPHI was built and operated by approximately 600 scientists from 50 laboratories all over the world.

DELPHI consisted of a central cylindrical section and two endcaps, in a solenoidal magnetic field of 1.2 T provided by a superconducting coil. The overall length and the diameter were over 10 m and the total weight was 2500 tons. The electron–positron collisions took place inside the vacuum pipe at the center of DELPHI and the products of the annihilations would fly radially outwards, tracked by several detection layers and read out via about 200 000 electronic channels. A typical event was about one million bits of information.

The DELPHI detector was composed of subdetectors as shown in Fig. 4.29. In the barrel part of the detector, covering approximately the region of polar angle θ between 40° and 140°, there was an onion-like structure of tracking detectors, the ones closest to the collision point being characterized by best resolution: the silicon

Vertex Detector (VD), a cylinder of proportional counters called the Inner Detector (ID), the Time Projection Chamber (TPC), another cylinder of proportional counters called the Outer Detector (OD) and the Barrel Muon Chambers (MUB). The Time Projection Chamber (TPC), shown as the big cylinder in the Figure, was the main tracking device of DELPHI, helping as well in charged particle identification by measuring the specific ionization energy loss dE/dx. The detector provided points per particle trajectory at radii from 40 to 110 cm.

Also in the forward part, a sequence of tracking chambers was present: the Forward Silicon Detector, the Forward Chambers A and B (FCA and FCB), the Forward Muon Chambers (MUF) were devoted to precise measurement of the trajectories of charged particles, and hence to the precise determination of the directions and momenta of the charged particles.

Electron and photon identification was provided primarily by the electromagnetic calorimetry system. This was composed of a barrel calorimeter (the High-density Projection Chamber, HPC) and a forward calorimeter (FEMC); a smaller calorimeter in the very forward region was used mainly for luminosity measurement.[14] The HPC was installed as a cylindrical layer outside the Outer Detector, inside the solenoid; it was an accordion of lead filled with gas as sensitive detector. The Forward ElectroMagnetic Calorimeter (FEMC) consisted of two 5 m diameter disks made of lead glass, with the front faces placed at $|z| = 284$ cm; it detected the Cherenkov light emitted by charged particles in the shower.

The hadron calorimeter (HCAL) was a sampling gas detector incorporated in the magnet yoke (made mainly of iron), covering both the barrel and the endcap regions. It provided calorimetric energy measurements of charged and neutral hadrons (strongly interacting particles).

The identification of charged hadrons in DELPHI relied also on the specific ionization energy loss per unit length in the TPC, and on ring-imaging Cherenkov (RICH) detectors in the barrel and in the forward regions.

The overall accuracy in momentum can be parameterized as

$$\frac{\delta p}{p} \simeq 0.6\% \, p_T \, , \tag{4.16}$$

where p is expressed in GeV/c, and the typical calorimetric resolution in the barrel part is

$$\frac{\delta E}{E} \simeq \frac{7\%}{\sqrt{E}} \oplus 1\% \, , \tag{4.17}$$

with E expressed in GeV.

Two reconstructed events are shown in Fig. 4.30.

[14] Luminosity can be measured with small error through the rate of occurrence of a process with a large cross section, well known both theoretically and experimentally. The elastic scattering e^+e^- at small angle (Bhabha scattering) fulfills the requirements.

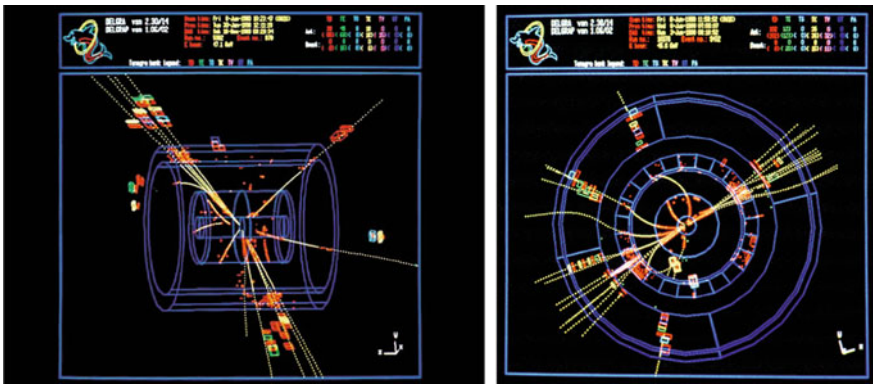

Fig. 4.30 Two events reconstructed by DELPHI, projected on the *xz* plane (left) and on the *xy* plane (right). Credits: CERN

4.4.2.3 CMS at LHC

The Compact Muon Solenoid (CMS) experiment is one of the two large general-purpose particle physics detectors built on the proton–proton Large Hadron Collider (LHC) at CERN.[15] Approximately 3000 scientists, representing 183 research institutes and 38 countries, form the CMS collaboration who built and since 2008 operates the detector. The detector is shown in Fig. 4.31. Proton–proton collisions at c.m. energies of 13 TeV are recorded.

As customary for collider detectors, CMS in structured in layers arranged in an onion-like structure.

Layer 1 is devoted to tracking. The inner silicon tracker is located immediately around the interaction point. It is used to identify the tracks of individual particles and match them to the vertices from which they originated. The curvature of charged particle tracks in the magnetic field allows their charge and momentum to be measured. The CMS silicon tracker consists of 13 layers in the central region and 14 layers in the endcaps. The three innermost layers (up to 11 cm radius) are made of $100 \times 150\,\mu$m pixels (a total of 66 million pixels) and the next four (up to 55 cm radius) are silicon strips (9.6 million strip channels in total). The CMS silicon tracker is the world's largest silicon detector, with 205 m^2 of silicon sensors (approximately the area of a tennis court) and 76 million channels.

[15] Seven detectors have been constructed at the LHC, located underground in large caverns excavated at the LHC's intersection points. ATLAS and CMS are large, general-purpose particle detectors. A Large Ion Collider Experiment (ALICE) and LHCb have more specific roles, respectively, the study of collisions of heavy ions and the study of the physics of the *b* quark. The remaining three are much smaller; two of them, TOTEM and LHCf, study the cross section in the forward region (which dominates the total hadronic cross section, as we shall see in Chap. 6); finally, MoEDAL searches for exotic particles, magnetic monopoles in particular.

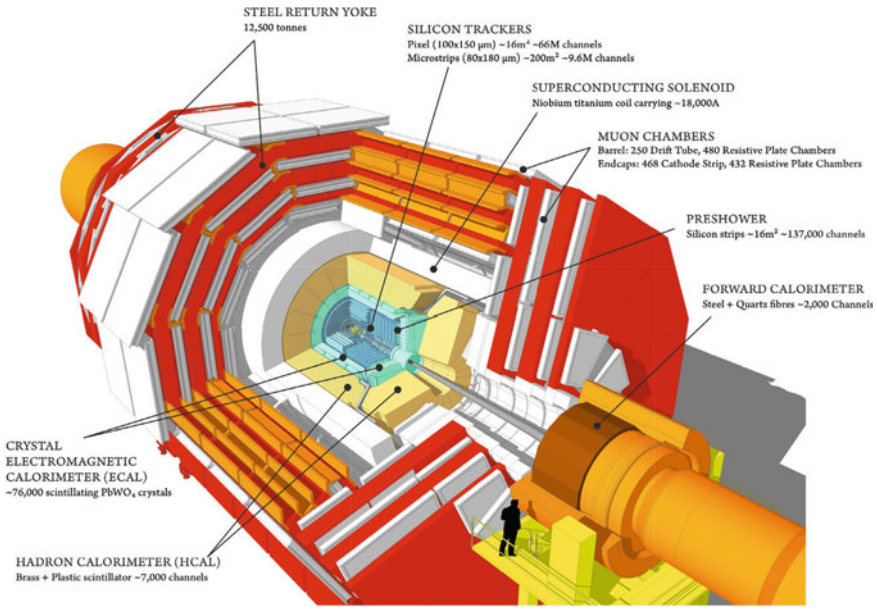

Fig. 4.31 The CMS detector at the LHC. Source: CERN

Layer 2 is devoted to electromagnetic calorimetry. The Electromagnetic Calorimeter (ECAL) is constructed from crystals of lead tungstate, $PbWO_4$, a very dense but optically clear material. It has a radiation length of 0.89 cm, and a rapid light yield (80% of light yield within one crossing time of 25 ns) of about 30 photons per MeV of incident energy. The crystals front size is 22 mm $\times$ 22 mm, with a depth of 23 cm. They are readout by silicon avalanche photodiodes and sit in a matrix of carbon fiber that ensures optical isolation. The barrel region consists of $\sim$60 000 crystals, with a further $\sim$7000 in each of the endcaps.

Layer 3 is devoted to hadronic calorimetry. The Hadronic Calorimeter (HCAL) consists of layers of dense material (brass or steel) interleaved with tiles of plastic scintillators, read out via wavelength-shifting fibers by hybrid photodiodes. This combination was optimized to guarantee the maximum amount of absorbing material inside the magnet coil.

Layer 4 is the magnet. It is 13 m long and 6 m in diameter, and it is a refrigerated superconducting niobium-titanium coil providing a solenoidal field of 3.8 T (the current being $\sim$18 000 A, giving a total stored energy of about 2.5 GJ, equivalent to about 500 kg of TNT: dump circuits to safely dissipate this energy are in place, should the magnet quench).

Layer 5 is occupied by the muon detectors and the return yoke. To identify muons and measure their momenta, CMS uses mostly drift tubes and resistive plate chambers. The drift tubes provide precise trajectory measurements in the central barrel region. The RPC provides an accurate timing signal at the passage of a muon.

The amount of raw data from each crossing is approximately 1 MB, which at the 40 MHz crossing rate would result in 40 TB of data per second. A multi-stage trigger system reduces the rate of interesting events down to about 100/s. At the first stage, the data from each crossing are held in buffers within the detector and some key information is used to identify interesting features (such as large transverse momentum particles, high-energy jets, muons or missing momentum). This task is completed in around 1 μs, and the event rate is reduced by a factor of about thousand down to 50 kHz. The data corresponding to the selected events are sent over fiber-optic links to a higher level trigger stage, which is a software trigger. The lower rate allows for a much more detailed analysis of the event, and the event rate is again reduced by a further factor of about a thousand, down to around 100 events per second. In a high-luminosity collider as the LHC, one single bunch crossing may produce several separate events, called pile-up events. Trigger systems must thus be very effective.

The overall accuracy in momentum can be parameterized as

$$\frac{\delta p}{p} \simeq 0.015\% \, p_T \oplus 0.5\% \,, \tag{4.18}$$

where p is expressed in GeV/c, and the typical calorimetric resolution in the barrel part is

$$\frac{\delta E}{E} \simeq \frac{3\%}{\sqrt{E}} \oplus 0.3\% \,, \tag{4.19}$$

with E expressed in GeV.

A reconstructed event is seen in Fig. 4.32.

4.4.2.4 ATLAS at LHC

ATLAS (A Toroidal LHC ApparatuS, Fig. 4.33) is 46 m long, 25 m in diameter, and weighs about 7000 tons. It consists of a series of ever-larger concentric cylinders around the interaction point:

- An inner tracking system: operating inside an axial magnetic field of 2 T, it is based on three types of tracking devices—an innermost silicon pixel detector is followed by a silicon strip detector and finally by straw tubes with particle identification capabilities based on transition radiation in the outer tracker.
- A hybrid calorimeter system: liquid argon with different types of absorber materials is used for the electromagnetic part, the hadronic endcap and the forward calorimeter. The central hadronic calorimeter is a sampling calorimeter with steel as the absorber material and scintillator as the active medium.
- A large muon spectrometer: an air-core toroid system generates an average field of 0.5 T (1 T), in the barrel (endcap) region of this spectrometer, resulting in a bending power between 2.0 and 7.5 Tm. Tracks are measured by monitored drift tubes and cathode strip chambers. Trigger information is provided by Thin Gap Chambers (TGC) in the endcap and RPC in the barrel.

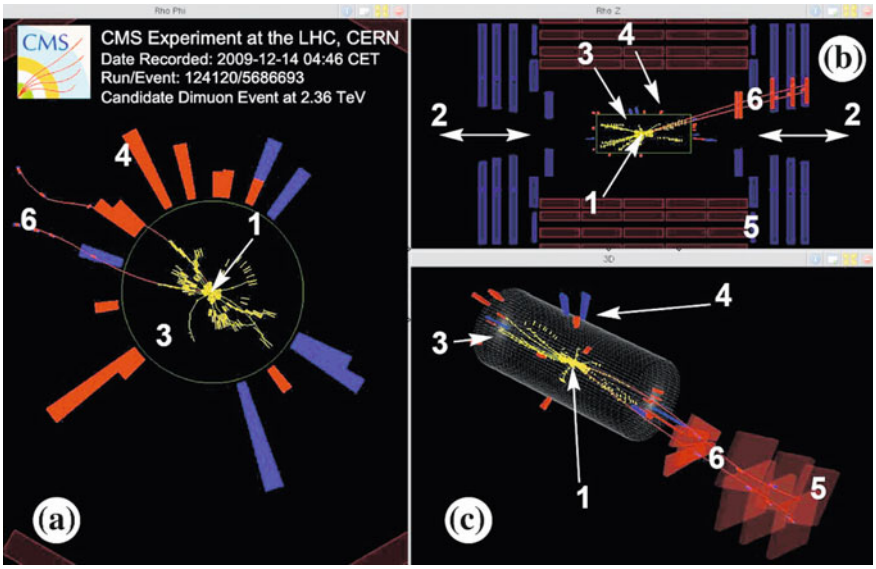

Fig. 4.32 An event reconstructed by CMS as shown in different projections by the CMS event display. Source: CERN

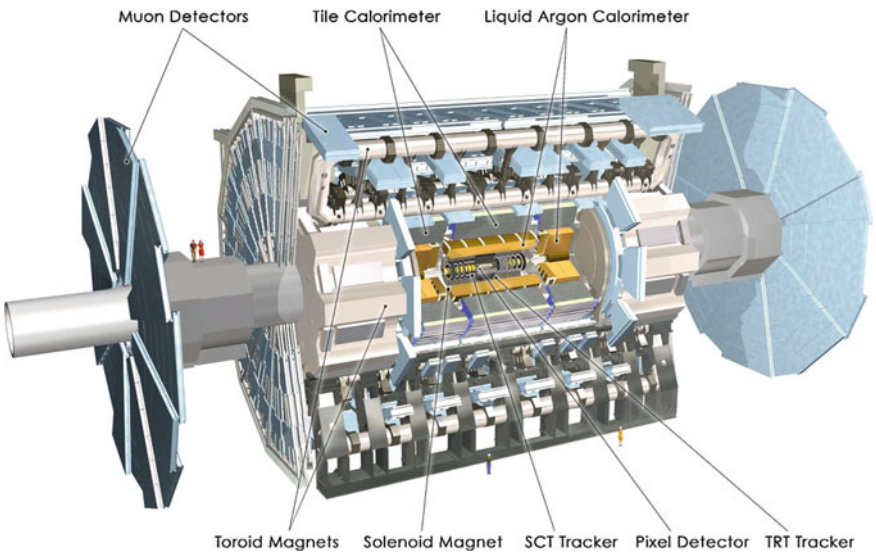

Fig. 4.33 Sketch of the ATLAS detector. Credit: CERN

Table 4.4 Comparison of the main design parameters of CMS and ATLAS

Parameter	ATLAS	CMS
Total weight (tons)	7000	12 500
Overall diameter (m)	22	15
Overall length (m)	46	20
Magnetic field for tracking (T)	2	4
Solid angel for precision measurement ($\Delta\phi \times \Delta\eta$)	$2\pi \times 5.0$	$2\pi \times 5.0$
Solid angel for energy measurement ($\Delta\phi \times \Delta\eta$)	$2\pi \times 9.6$	$2\pi \times 9.6$
Total cost (million euros)	550	550

An electromagnetic calorimeter and a Cherenkov counter instrument the endcap region. Two scintillator wheels were mounted in front of the electromagnetic endcaps to provide trigger signals with minimum bias.

The ATLAS trigger and data acquisition is a multi-level system with buffering at all levels. Trigger decisions are based on calculations done at three consecutive trigger levels.

The overall accuracy in momentum can be parameterized as

$$\frac{\delta p}{p} \simeq 0.05\% \, p_T \oplus 1\% \,, \tag{4.20}$$

where p is expressed in GeV/c, and the typical calorimetric resolution in the barrel part is

$$\frac{\delta E}{E} \simeq \frac{2.8\%}{\sqrt{E}} \oplus 0.3\% \,, \tag{4.21}$$

with E expressed in GeV.

The main design parameters of ATLAS and CMS are compared in Table 4.4.

4.5 Cosmic-Ray Detectors

The strong decrease in the flux Φ of cosmic rays with energy, in first approximation $\Phi \propto E^{-3}$, poses a big challenge to the dimensions and the running times of the experimental installations when high energies are studied. Among cosmic rays, a small fraction of about 10^{-3} are photons, which are particularly interesting since they are not deflected by intergalactic magnetic fields, and thus point directly to their sources; the large background from charged cosmic rays makes the detection even more complicated. Neutrinos are expected to be even less numerous than photons, and their detection is even more complicated due to the small cross section.

We shall examine first the detectors of cosmic rays which have a relatively large probability of interactions with the atmosphere: nuclei, electrons/positrons, and photons. We shall then discuss neutrinos, and finally the recently discovered gravitational waves, for which detection techniques are completely different.

Balloon and satellite-borne detectors operate at an altitude of above 15 km where they can detect the interaction of the primary particle inside the detector, but they are limited in detection area and therefore also limited in the energy range they can measure. The maximum primary energy that can be measured by means of direct observations is of the order of 1 PeV; above this energy the observations are performed by exploiting the cascades induced in atmosphere by the interactions of cosmic rays.

4.5.1 *Interaction of Cosmic Rays with the Atmosphere: Extensive Air Showers*

The physics of electromagnetic and hadronic showers has been described before; here we particularize the results obtained to the development of the showers due to the interaction of high-energy particles with the atmosphere. These are called extensive air showers (EAS).

High-energy hadrons, photons, and electrons interact in the high atmosphere. As we have seen, the process characterizing hadronic and electromagnetic showers is conceptually similar (Fig. 4.34).

For photons and electrons above a few hundred MeV, the cascade process is dominated by the pair production and the bremsstrahlung mechanisms: an energetic photon scatters on an atmospheric nucleus and produces an e^+e^- pair, which emits

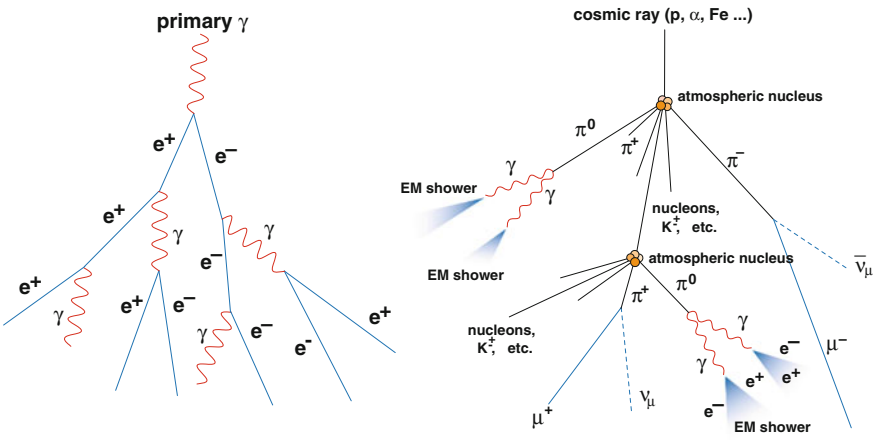

Fig. 4.34 Schematic representation of two atmospheric showers initiated by a photon (left) and by a proton (right). From R.M. Wagner, dissertation, MPI Munich 2007

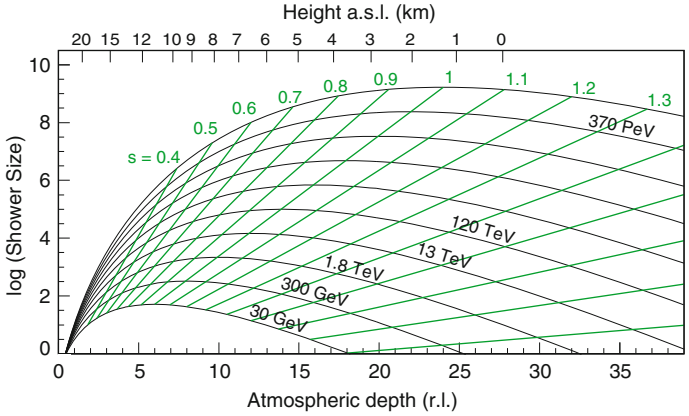

Fig. 4.35 Longitudinal shower development from a photon-initiated cascade. The parameter s describes the shower age. From R.M. Wagner, dissertation, MPI Munich 2007; adapted from reference [F4.1] in the "Further reading"

secondary photons via bremsstrahlung; such photons produce in turn a pair, and so on, giving rise to a shower of charged particles and photons, degrading the energy down to the critical energy E_c where the ionization energy loss of charged particles starts dominating over bremsstrahlung.

The longitudinal development of typical photon-induced extensive air showers is shown in Fig. 4.35 for different values of the primary energies. The maximum shower size occurs approximately after $\ln(E/E_c)$ radiation lengths, the radiation length for air being about 37 g/cm^2 (approximately 300 m at sea level and NTP). The critical energy E_c is about 80 MeV in air.[16]

The hadronic interaction length in air is about 90 g/cm^2 for protons (750 m for air at NTP), being shorter for heavier nuclei—the dependence of the cross section on the mass number A is approximately $A^{2/3}$. The transverse profile of hadronic showers is in general wider than for electromagnetic showers, and fluctuations are larger.

Particles release energy in the atmosphere, which acts like a calorimeter, through different mechanisms—which give rise to a measurable signal. We have discussed these mechanisms in Sect. 4.1.1; now we reexamine them in relation to their use in detectors.

[16] In the isothermal approximation, the depth x of the atmosphere at a height h (i.e., the amount of atmosphere above h) can be approximated as

$$x \simeq Xe^{-h/7\,\mathrm{km}}\,,$$

with $X \simeq 1030\,\mathrm{g/cm^2}$.

4.5.1.1 Fluorescence

As the charged particles in an extensive air shower go through the atmosphere, they ionize and excite the gas molecules (mostly nitrogen). In the de-excitation processes that follow, visible and ultraviolet (UV) radiations are emitted. This is the so-called fluorescence light associated to the shower.

The number of emitted fluorescence photons is small—of the order of a few photons per electron per meter in air. This implies that the fluorescence technique can be used only at high energies. However, it is not directional as in the case of Cherenkov photons (see below), and thus it can be used in serendipitous observations.

4.5.1.2 Cherenkov Emission

Many secondary particles in the EAS are superluminal, and they thus emit Cherenkov light that can be detected. The properties of the Cherenkov emission have been discussed in Sects. 4.1.1 and 4.2.

At sea level, the value of the Cherenkov angle θ_C in air for a speed $\beta = 1$ is about 1.3°, while at 8 km a.s.l. it is about 1°. The energy threshold for Cherenkov emission at sea level is 21 MeV for a primary electron and 44 GeV for a primary muon.

Half of the emission occurs within 20 m of the shower axis (about 70 m for a proton shower). Since the intrinsic angular spread of the charged particles in an electromagnetic shower is about 0.5°, the opening of the light cone is dominated by the Cherenkov angle. As a consequence, the ground area illuminated by Cherenkov photons from a shower of 1 TeV (the so-called light pool of the shower) has a radius of about 120 m, with an approximately constant density of photons per unit area. The height of maximal emission for a primary photon of energy of 1 TeV is approximately 8 km a.s.l., and about 150 photons per m^2 arrive at 2000 m a.s.l. (where typically Cherenkov telescopes are located, see later) in the visible and near UV frequencies. This dependence is not linear, being the yield of about 10 photons per square meter at 100 GeV.

The atmospheric extinction of light drastically changes the Cherenkov light spectrum (originally proportional to $1/\lambda^2$) arriving at the detectors, in particular suppressing the UV component (Fig. 4.36) which is still dominant. There are several sources of extinction: absorption bands of several molecules, molecular (Rayleigh) and aerosol (Mie) scattering.

Radio Emission. Cosmic-ray air showers also emit radio waves in the frequency range from a few to a few hundred MHz, an effect that opens many interesting possibilities in the study of UHE and EHE extensive air showers. At present, however, open questions still remain concerning both the emission mechanism and its strength.

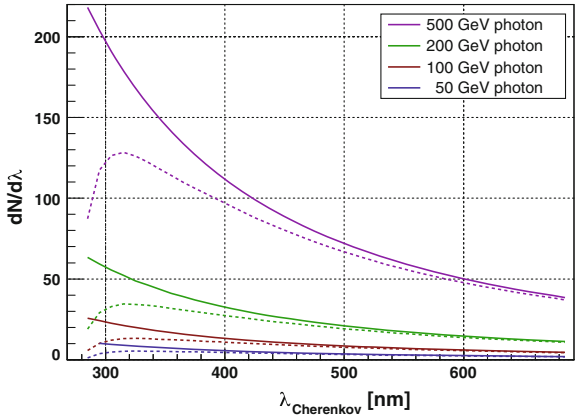

Fig. 4.36 Spectrum of the Cherenkov radiation emitted by gamma-ray showers at different energies initiated at 10 km a.s.l. (solid curves) and the corresponding spectra detected at 2200 meters a.s.l. (lower curve). From R.M. Wagner, dissertation, MPI Munich 2007

4.5.2 Detectors of Charged Cosmic Rays

The detection of charged cosmic rays may be done above the Earth's atmosphere in balloon or satellite-based experiments whenever the fluxes are large enough (typically below tens or hundreds of GeV) and otherwise in an indirect way by the observation of the extensive air showers produced in their interaction with the atmosphere (see Sect. 4.5.1).

In the last thirty years, several experiments to detect charged cosmic rays in space or at the top of the Earth's atmosphere were designed and a few were successfully performed. In particular:

- The Advanced Composition Explorer (ACE) launched in 1997 and still in operation (with enough propellant to last until ∼2024) has been producing a large set of measurements on the composition (from H to Ni) of solar and Galactic Cosmic rays covering energies from 1 keV/nucleon to 500 MeV/nucleon. ACE has several instruments which are able to identify the particle charge and mass using different types of detectors (e.g., silicon detectors, gas proportional counters, optical fiber hodoscopes) and techniques (e.g., the specific energy loss dE/dx, the time-of-flight, electrostatic deflection). The total mass at launch (including fuel) was about 800 kg.
- The Balloon-borne Experiment with Superconducting Spectrometer (BESS) performed successive flights starting in 1993 with the main aim to measure the low-energy antiproton spectrum and to search for antimatter, namely antihelium. The last two flights (BESS-Polar) were over Antarctica and had a long duration (8.5 days in 2004 and 29.5 days in 2007/2008). The instrument, improved before every flight, had to ensure a good charge separation and good particle identification. It had a horizontal cylindrical configuration and its main components were as follows: a thin-wall superconducting magnet; a central tracker composed of drift chambers; time-of-flight scintillation counter hodoscopes; an aerogel (an ultralight

porous material derived from a gel by replacing its liquid component with a gas) Cherenkov counter.

- The PAMELA experiment, launched in June 2006, measured charged particles and antiparticles out of the Earth's atmosphere during a long (six years) period. A permanent magnet of 0.43 T and a microstrip silicon tracking system ensured a good charge separation between electrons and positrons up to energies of the order of hundred GeV measured by a silicon/tungsten electromagnetic calorimeter complemented by a neutron counter to enhance the electromagnetic/hadronic discrimination power. The trigger was provided by a system of plastic scintillators which were also used to measure the time of flight and an estimation of the specific ionization energy loss (dE/dX).
- The Alpha Magnetic Spectrometer (AMS-02) was installed in May 2011 on the International Space Station. Its concept is similar to PAMELA but with a much larger acceptance and a more complete set of sophisticated and higher performing detectors. Apart from the permanent magnet and the precision silicon tracker it consists of a transition radiation detector, time-of-flight and anticoincidence counters, a ring-imaging Cherenkov detector, and an electromagnetic calorimeter (Fig. 4.37). Its total weight is 8500 kg and its cost was over 2 billion euros.
- ISS-CREAM (Cosmic Ray Energetics and Mass for the International Space Station) is in orbit since 2017. It uses a Si detector, timing detectors, and scintillating fiber hodoscopes to detect the charge of incident particles up to iron at energies up to the knee. Energies are measured with a transition radiation detector (TRD), and with a calorimeter. The mission follows successful balloon flights of the CREAM detector.

Extensive air showers produced by high-energy cosmic rays in their interaction with the atmosphere are detected using three different techniques:

- The measurement of a fraction of the EAS particles arriving at the Earth's surface through an array of surface detectors (SD);
- The measurement in moonless nights of the fluorescence light emitted mainly by the de-excitation of the atmosphere nitrogen molecules excited by the shower low energy electrons through an array of ultraviolet fluorescence detectors (FD) placed on the Earth surface or even in satellites; and
- The measurement of the Cherenkov light emitted by the ultrarelativistic air shower particles in a narrow cone around the shower axis, through telescopes as the Imaging Atmosphere Cherenkov Telescopes (IACTs), which will be discussed in the next section in the context of gamma-ray detection.

Other possible techniques (radio detection for example) might be exploited in the future.

Surface detectors measure at specific space locations the time of arrival of individual particles. The most widely used surface detectors are scintillation counters and water Cherenkov counters. More sophisticated tracking detectors as resistive plate chambers, drift chambers, and streamer tube detectors have been also used or proposed.

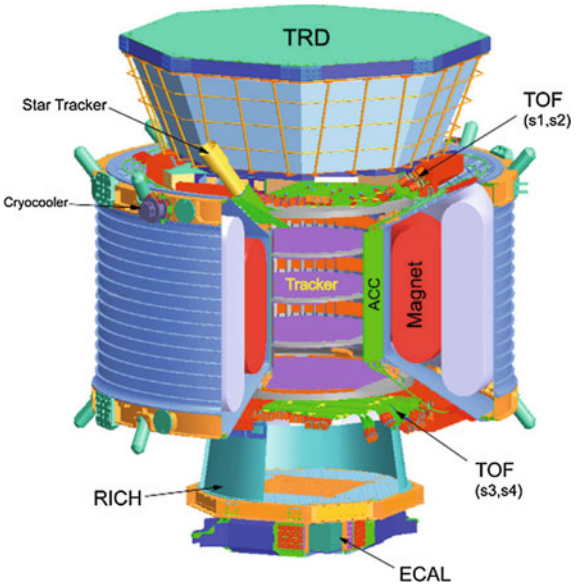

Fig. 4.37 The AMS-02 detector layout. Credit: AMS Collaboration

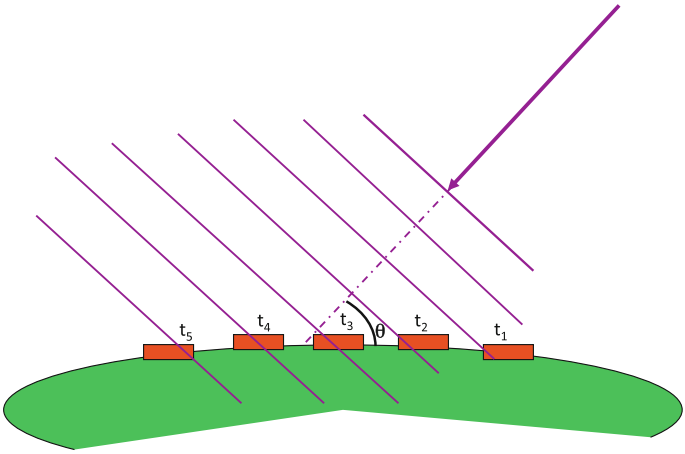

Fig. 4.38 Air shower front arriving at the Earth surface; arrival times are measured by surface detectors and allow for the determination of the shower arrival direction

The arrival direction of an air shower is determined from the arrival time at the different surface detectors of the shower front (Fig. 4.38). To a first approximation, the front can be described by a thin disk propagating at the speed of light; second-order corrections can be applied to improve the measurement.

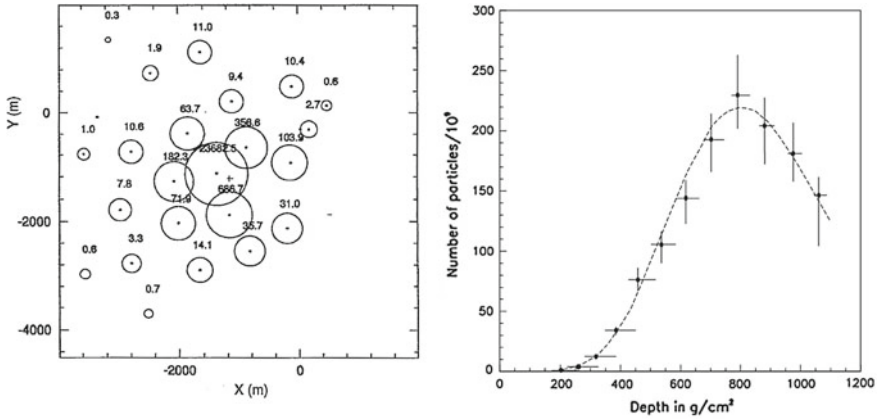

Fig. 4.39 *Left:* Map of the observed particle density pattern of the highest-energy event at the AGASA experiment. The cross corresponds to the fitted position of the shower core. From http://www.icrr.u-tokyo.ac.jp. *Right:* Shower longitudinal profile of the most energetic event observed by the Fly's Eye experiment. From D.J. Bird et al., Astrophys. J. 441 (1995) 144

The impact point of the air shower axis at the Earth's surface (the air shower core) is defined as the point of maximum particle density and is determined from the measured densities at the different surface detectors using, to a first approximation, a modified center-of-mass algorithm. In Fig. 4.39, left, the particle density pattern of the highest energy event at the AGASA array experiment[17] is shown. The energy of the event was estimated to be about 2×10^{20} eV. The measured densities show a fast decrease with the distance to the core and are usually parameterized by empirical or phenomenologically inspired formulae—the most popular being the NKG function, introduced in Sect. 4.1.7—which depend also on the shower age (the level of development of the shower when it reaches ground). Such functions allow for a better determination of the shower core and for the extrapolation of the particle density to a reference distance of the core, which is then used as an estimator of the shower size and thus of the shower energy. The exact function and the reference distance depend on the particular experimental setup.

Fluorescence telescopes record the intensity and arrival time of light emitted in the atmosphere in specific solid angle regions and thus allow reconstructing the shower axis and the shower longitudinal profile (Fig. 4.39, right). Figure 4.40 shows the image of a shower in the focal plane of one of the Pierre Auger fluorescence telescopes (see later). The third dimension, time, is represented in a color code.

The geometry of the shower (Fig. 4.41) is then reconstructed in two steps: first the shower detector plane (SDP) is found by minimizing the direction of the SDP perpendicular to the mean directions of the triggered pixels, and then the shower axis

[17] The Akeno Giant Air Shower Array (AGASA) is a very large surface array covering an area of 100 km^2 in Japan and consisting of 111 surface detectors (scintillators) and 27 muon detectors (proportional chambers shielded by Fe/concrete).

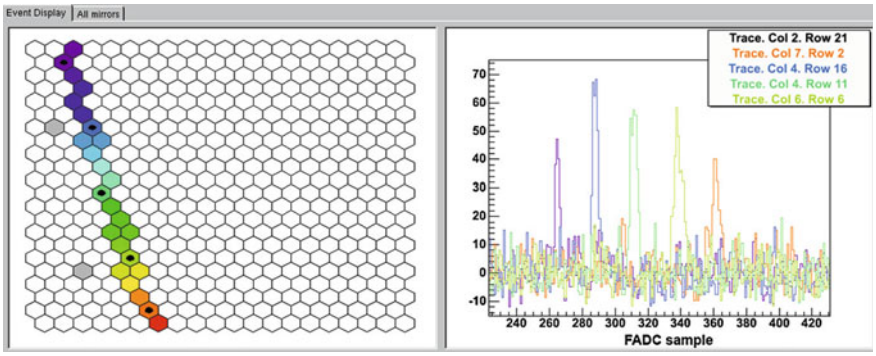

Fig. 4.40 Display of one shower in the focal plane of one of the Pierre Auger fluorescence telescopes. Left: Pattern of the pixels with signals. Right: response (signal versus time, with a time bin of 100 ns) of the selected pixels (marked with a black dot in the left panel). The development of the shower in the atmosphere can be qualitatively pictured. From https://www.auger.org

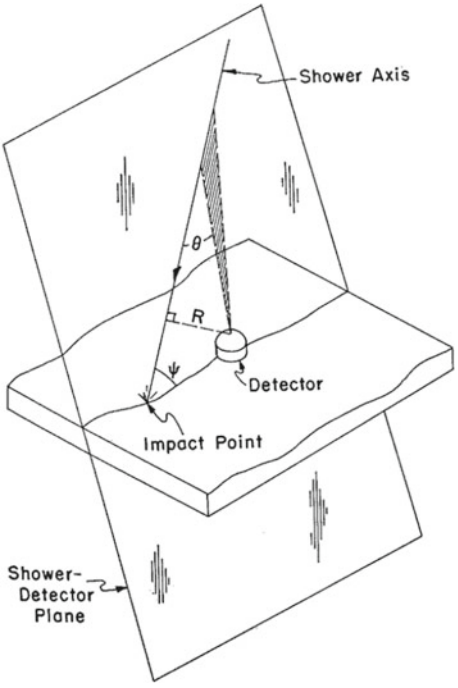

Fig. 4.41 Shower geometry as seen by a fluorescence telescope. From K.-H. Kampert and A. Watson, "Extensive Air Showers and Ultra High Energy Cosmic Rays: A Historical Review," EPJ-H 37 (2012) 359

parameters within the SDP are found from the measured arrival time of the light in each pixel, assuming that the shower develops along a line at the speed of light.

Simultaneous observations of the shower by two (stereo) or more fluorescence detectors or by a surface detector array (hybrid detection) provide further geometric

constraints improving considerably the resolution of the shower geometric reconstruction.

The intensity of collected light along the shower axis is corrected for the detector efficiency, the solid angle seen by each detector pixel, the attenuation in the atmosphere, the night sky background, and the contributions of fluorescence (dominant unless the shower axis points in the direction of the telescope) and of Cherenkov light are estimated. Finally, the shower longitudinal profile (Fig. 4.39, right) is obtained assuming proportionality between the fluorescence light emitted and the number of particles in the shower. The integral of such a profile is a good estimator of the energy of the shower (small "missing momentum" corrections due to low interacting particles in the atmosphere, like muons and neutrinos, have to be taken into account).

The Pierre Auger Observatory. The Pierre Auger Observatory in Malargue, Argentina, is the largest cosmic-ray detector ever built. It covers a surface of about 3000 square kilometers with 1600 surface detector stations (Cherenkov water tanks) arranged in a grid of 1.5 km side complemented by 27 fluorescence telescopes, grouped into four locations to cover the atmosphere above the detector area (Fig. 4.42).

Each water tank is a cylinder of $10\,m^2$ base by 1.5 m height filled with 12 tons of water (Fig. 4.43). The inner walls of the tank are covered with a high reflectivity material. The Cherenkov light, produced by the charged particles crossing the water, is collected by three PMTs placed at the top of the tank. Each tank is autonomous being the time given by a GPS unit and the power provided by a solar panel; it communicates via radio with the central data acquisition system.

Each fluorescence detector is a Schmidt telescope[18] with a field of view of 30° in azimuth and 29° in elevation (Fig. 4.43). Light enters the telescope through an ultraviolet filter installed over the telescope and is collected in a 3.5 m diameter spherical mirror which focuses it in a 440 PMT camera.

The signal by an event of extremely high energy is shown in Fig. 4.44.

The Telescope Array. The largest cosmic-ray detector in the Northern hemisphere is the Telescope Array (TA) in Utah, USA. Similar to Auger, it is also a hybrid detector composed of a surface array of 507 scintillator detectors, each 3 m in size, located on a 1.2 km square grid, plus three fluorescence stations, each with a dozen of telescopes instrumented with a 256 PMT camera covering 3°–33° in elevation. The total surface covered is about $800\,km^2$.

Future Prospects: Detection from Space. An innovative approach to detect extremely high-energy cosmic rays has been proposed by several collaborations as the "EUSO concept": increasing the effective area by looking to a large volume of the atmosphere from a satellite. A space telescope equipped with a Fresnel lens can detect the fluorescence light emitted by the extended air showers (Fig. 4.45). Observing the Earth from 400 km above and having a large field of view (±30°), one

[18] In a Schmidt telescope, a spherical mirror receives light that passed through a thin aspherical lens that compensates for the image distortions that will occur in the mirror. Light is then reflected in the mirror into a detector that records the image.

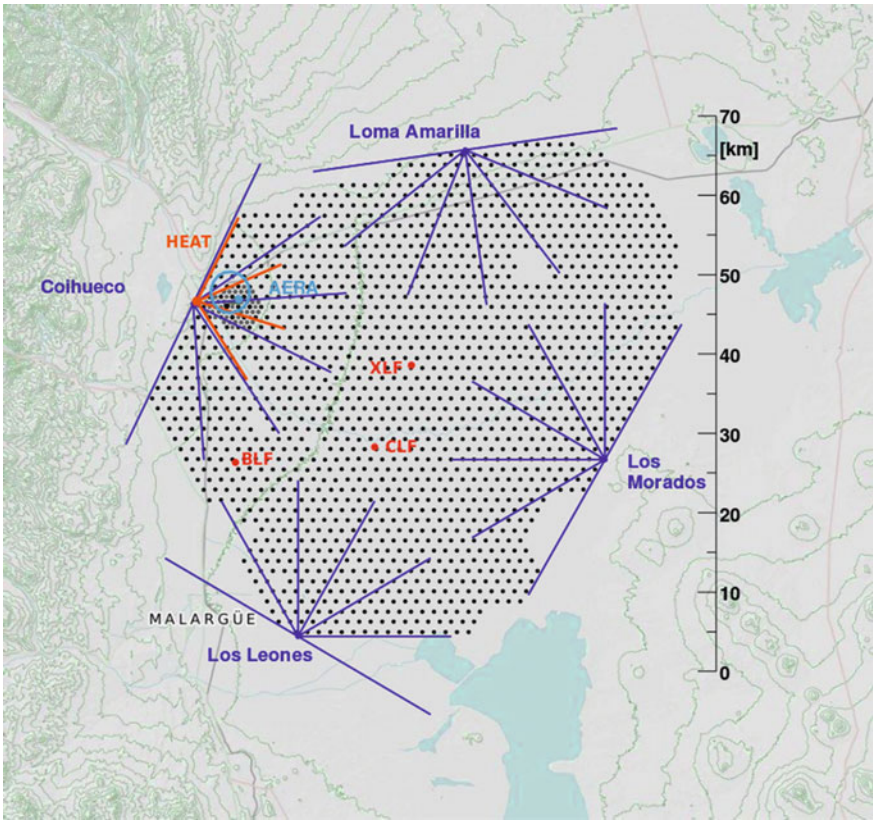

Fig. 4.42 The Pierre Auger Observatory near Malargue, Argentina. The radial lines point to the fluorescence detectors. The black dots are the 1600 surface detectors (SD). Sites with specialized equipment are also indicated. By Darko Veberic [GFDL http://www.gnu.org/copyleft/fdl.html], via Wikimedia Commons

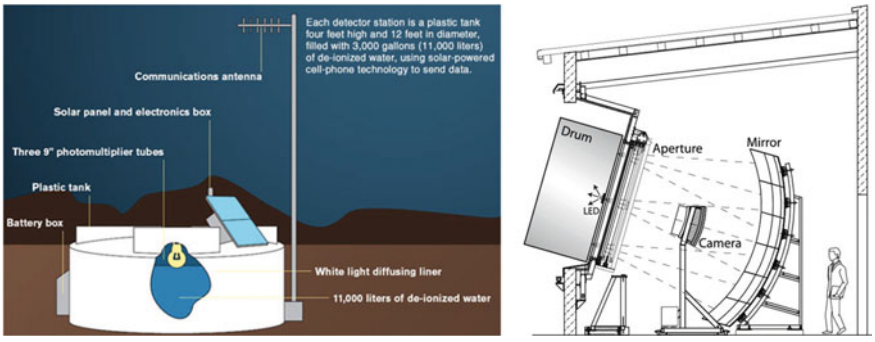

Fig. 4.43 Sketch of one of the Pierre Auger surface detectors (left); a fluorescence telescope (right). From https://www.auger.org

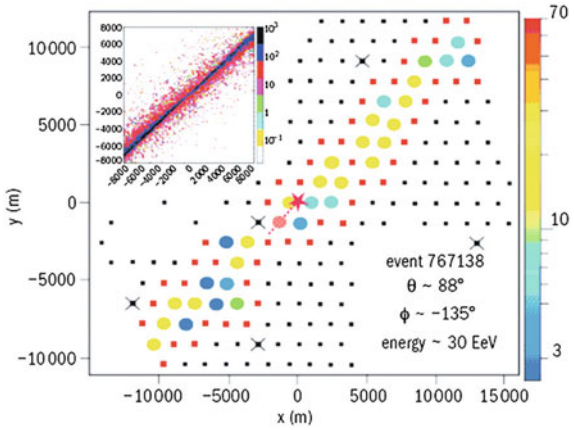

Fig. 4.44 A 30 EeV event at a zenith angle of about 88° recorded by the Auger detector. The inset shows a simulation of an event of the same energy and angle. From https://www.auger.org

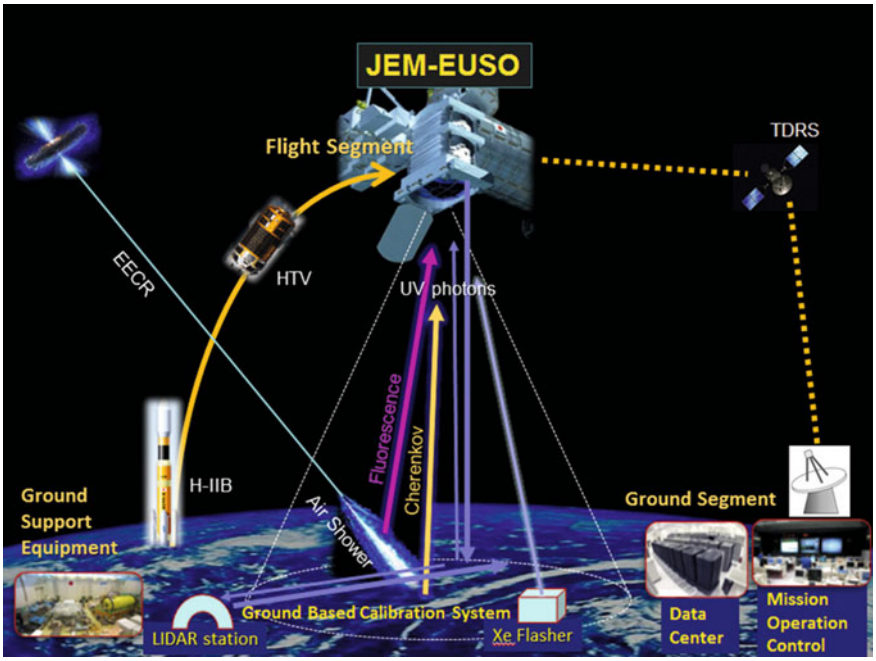

Fig. 4.45 EUSO observational principle. From http://jemeuso.riken.jp/en/

can cover a large surface on Earth (above $1.9 \times 10^5\,\mathrm{km}^2$), but the energy threshold is high (around $3 \times 10^{19}\,\mathrm{eV}$).

4.5.3 Detection of Hard Photons

Most photons in astrophysics are produced by systems near thermal equilibrium, approximately blackbodies. The bulk of astrophysical photons is due to CMB at a temperature of about 2.7 K (corresponding to an energy of about 0.1 meV). The highest-energy thermalized systems emit at energies of about a keV, i.e., in the X-ray range. We are interested in this book mainly on nonthermal processes, and thus, on photons in the keV range and above.

Nonthermal photons, in the keV range and above, are expected to be generated in astrophysical objects mostly by leptonic acceleration mechanisms (see Chap. 10), and by the decays of neutral pions produced in cosmic-ray interactions with radiation or gas—as these pions decay, they produce photons with typical energies one order of magnitude smaller than those of the cosmic-ray nucleons generating them. Photons in the MeV range can come also from nuclear de-excitation processes.

The detection of photons above the UV range is complicated by the absorption in the atmosphere (see Fig. 4.46) and by the faintness of the signal, in particular when compared to the corresponding charged particles of similar energy—being the latter three to four orders of magnitude more frequent. Photons interact with matter mostly due to photoelectric effect and by Compton mechanism at energies up to about 20–30 MeV, while e^+e^- pair production dominates above these energies.

Although arbitrary, a classification of hard photons as a function of their energy can be useful. We define as:

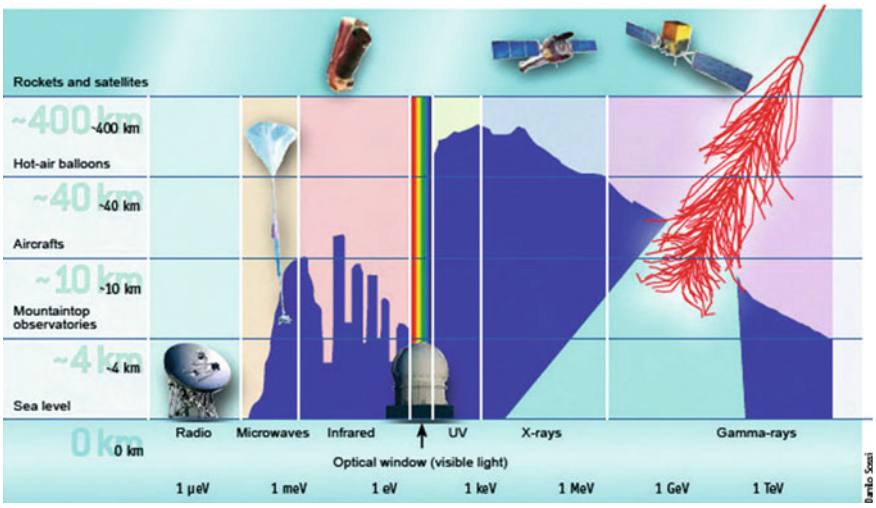

Fig. 4.46 Transparency of the atmosphere for different photon energies and possible detection techniques. Source: A. De Angelis and L. Peruzzo, "Le magie del telescopio MAGIC," Le Scienze, April 2007

1. Hard X-ray region (or keV region) the energy region between 3 and 300 keV.
2. Low-energy gamma-ray region (or MeV region) the energy region between 0.3 and 30 MeV. This is the region in which the Compton interaction probability is comparable with the pair production probability.
3. High-energy (HE) gamma-ray region (or GeV region) the energy region between 30 MeV and 30 GeV. The pair production process becomes dominant.
4. Very-high-energy (VHE) gamma-ray region (or TeV region) the energy region between 30 GeV and 30 TeV. Electromagnetic showers in the atmosphere start becoming visible.
5. PeV region the energy region between 30 TeV and 30 PeV. Charged particles from electromagnetic showers in the atmosphere can reach instruments at mountain-top altitudes. As we shall see in Chap. 10, however, the mean free path of photons at these energies is such that we expect photons from very few extragalactic sources to reach the Earth.

This classification, in particular, corresponds to different detection techniques, as we shall see now. The MeV, GeV, and TeV regions are especially important related to the physics of cosmic rays and to fundamental physics. Note the difference in range with respect to highest-energy charged cosmic rays—do not forget that the flux in the latter case is three orders of magnitude larger in the MeV–GeV region.

Main figures of merit for a detector are its effective area (i.e., the product of the area times the detection efficiency), the energy resolution, the space or angular resolution (called as well point spread function, or PSF). In particular the effective area has to be appropriate for the flux one wants to measure.

Due to the conversion probability in the atmosphere (whose thickness is about 28 radiation lengths at sea level) only satellite-based detectors can detect primary X/γ-rays – and thus gamma rays below the TeV region. Satellites are small, about 1 m^2 in area at maximum, because of the cost of space technology. The area sampled by ground-based detectors can be much larger than this. Since the fluxes of high-energy photons are low and decrease rapidly with increasing energy, TeV and PeV gamma rays can be detected only from the atmospheric showers they produce, i.e., by means of ground-based detectors. This fact clarifies another meaning of the division between HE and VHE photons: HE photons are detected using satellites, while for VHE photons the detection using ground-based instruments becomes possible.

4.5.3.1 Satellites

Satellite-based telescopes for hard photons can detect the primary particles at energies lower than ground-based telescopes. They have a small effective area, of the order of 1 m^2 maximum, which limits their sensitivity. They have a large duty cycle, and they suffer a low rate of background events, since they can be coupled to anticoincidence systems rejecting the charged cosmic rays. They have a large cost, dominated by the costs of launch and by the strong requirements of instruments to be sent into space, with little or no possibility of intervention to fix possible bugs.

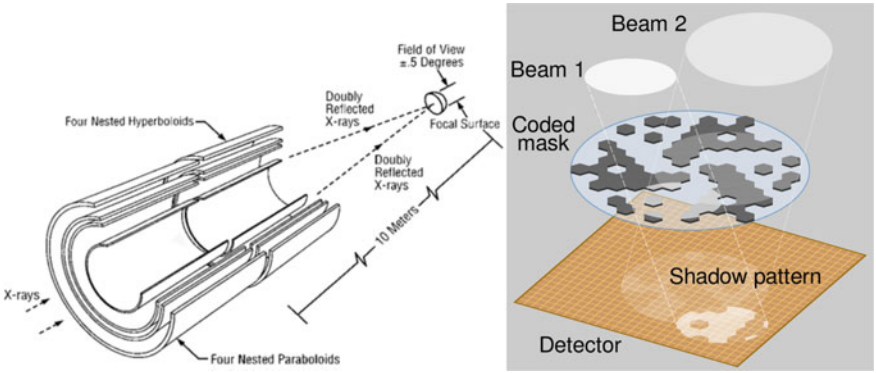

Fig. 4.47 Principles of operation of focusing grazing incident mirrors (left, credits: NASA) and of coded mask apertures (right, credits: Wikimedia Commons)

1. Satellites operational in the keV regime use different focal plane detectors and optical system. Optical systems (Fig. 4.47) are constituted by focusing grazing incident mirrors or by collimating elements such as coded mask systems (grids of materials opaque to various wavelengths of light: by blocking light in a known pattern, a coded "shadow" is cast upon a sensitive plane, and the properties of the original light sources can then be mathematically reconstructed from this shadow).
   1a. In the energy band of a few keV, satellites in use today include NASA's Chandra mission and ESA's XMM-Newton observatory, both launched in 1999; they both use X-ray grazing incident mirrors. Chandra has an effective area of 800 and 400 cm^2 at 0.25 and 5 keV, respectively. Different instruments can be inserted in the focal plane; at 1 keV, the typical field of view (FoV) is $30' \times 30'$ and space resolution is as good as 0.5 arcsec; the spectral resolving power $E/\Delta E$ is between 30 and 2000. ESA's X-ray Multi-Mirror Mission (XMM-Newton) uses three co-aligned grazing incidence gold-coated imaging X-ray telescopes each with an effective area of $\sim$1500 cm^2 at 1 keV with a spatial resolution of 6 arcsec. Also in this case there are different instruments. Typical effective area is of the order of 1000 cm^2 at 1 keV for a spectral resolving power of 20; of the order of 200 cm^2 for a resolving power of 1000. The maximum energy detected by these detectors is around 15 keV.
   NASA's NuSTAR (Nuclear Spectroscopic Telescope Array), launched in 2012, is a space-based X-ray telescope that operates in the range of 3–80 keV. NuSTAR is the first telescope using imaging techniques at energies above 15 keV. The NuSTAR grazing mirrors have a focal length of 10.15 m and are held at the end of a long deployable mast. The point spread function for the flight mirrors is 43 arc seconds, an unprecedentedly good resolution for focusing hard X-ray optics. In the future (launch is planned for 2028), the ATHENA (Advanced Telescope for High Energy Astrophysics) satellite, one hundred times more sensitive than the best existing X-ray telescopes, will fly within ESA's Cosmic Vision program.
   1b. At higher energies, collimating elements are used to image photons of energy

in the range from 100 keV to few MeV. Coded mask systems are used both by the Swift Burst Alert Telescope (BAT) and by the main instruments on board the INTEGRAL satellite.

The Neil Gehrels Swift Observatory (shortly Swift) is a NASA international mission launched in 2004. The primary scientific objectives are to determine the origin of Gamma Ray Bursts (GRB) and to pioneer their use as probes of the early Universe. Swift is a multiwavelength observatory carrying three instruments. The Burst Alert Telescope (BAT; 15–150 keV) is a wide field-of-view coded aperture imager with an effective area 5240 cm^2 and a FoV of 1.4 sr half coded and a position accuracy of $\sim 4'$. The X-Ray Telescope (XRT; 0.2–10.0 keV) uses a X-ray grazing mirror system and has a CCD Imaging spectrometer with an effective area of 110 cm^2 at 1.5 keV, a FoV of $23.6' \times 23.6'$ and a $\sim 5''$ position accuracy. The UV/Optical Telescope (UVOT; 170–650 nm) is a CCD detector with a FoV of $17' \times 17'$ and 0.3 arcsec position accuracy. The key characteristics of Swift are the rapid response to newly detected GRB and rapid data dissemination. As soon as the BAT discovers a new GRB, Swift rapidly releases its first position estimate, with (1–4) arcmin accuracy, to the ground segment, and an autonomous trigger allows the burst entering within the field of view of XRT and UVOT to follow up the afterglow.

ESA's International Gamma-Ray Astrophysics Laboratory (INTEGRAL) was launched in 2002. It is producing a complete map of the sky in the soft gamma-ray waveband and it is capable of performing high spectral and spatial observations in gamma rays. The observatory is also equipped with X-ray and optical detectors to provide simultaneous observations in these wavebands. The payload hosts several gamma-ray instruments. The Spectrometer (SPI; 20 keV–8 MeV) has a coded aperture mask with a FoV of 16° and a detection plane made of a Germanium array with a detector area of 500 cm^2, a spectral resolution ($E/\Delta E$) of 500 at 1 MeV and a spatial resolution of 2°. The Imager (IBIS; 15 keV–10 MeV) is also equipped with a coded aperture mask. Its FoV is $9° \times 9°$, and it has a detector area of 2600 cm^2 (CdTe array - ISGRI) and of 3100 cm^2 (CsI array - PICSIT) with a spatial resolution of $12'$. The Joint European X-Ray Monitor (JEM-X) makes observations simultaneously with the main gamma-ray instruments and provides images in the 3–35 keV prime energy band with an angular resolution of 3 arcmin.

In this energy range not collimated systems use scintillation materials to detect photons up to tens of MeV. The *Fermi* (see later) Gamma-ray Burst Monitor (GBM) is equipped with 12 NaI detectors sensitive from a few keV to about 1 MeV and two BGO detectors operating up to 40 MeV.

2. In the MeV regime, the state of the art for Compton imaging is mostly frozen at the COMPTEL instrument on the Compton Gamma Ray Observatory (CGRO), launched in 1991 aboard the space shuttle Atlantis, and safely deorbited in 2000. CGRO had four instruments that covered six decades of the electromagnetic spectrum, from 30 keV to 30 GeV. In order of increasing spectral energy coverage, these instruments were the Burst And Transient Source Experiment (BATSE), the Oriented Scintillation Spectrometer Experiment (OSSE), the Imaging Compton

Telescope (COMPTEL), and the Energetic Gamma Ray Experiment Telescope (EGRET). The Imaging Compton Telescope (COMPTEL) used the Compton effect and two layers of gamma-ray detectors to reconstruct an image of a gamma-ray source in the energy range 1–30 MeV. COMPTEL's upper layer of detectors were filled with a liquid scintillator which scattered an incoming gamma-ray photon. This photon was then absorbed by NaI crystals in the lower detectors. The instrument recorded the time, location, and energy of the events in each layer of detectors, making it possible to determine the direction and energy of the original gamma-ray photon and reconstruct an image and energy spectrum of the source. The silicon detector technology allows today improving the sensitivity of COMPTEL by two orders of magnitude, and also crucially improving the localization accuracy. Two detectors are under evaluation, e-ASTROGAM by a mostly European consortium and AMEGO by NASA, which use silicon detector planes without converter to build a hodoscope sensitive to both Compton interaction and pair production (Fig. 4.48).

3. In the GeV regime, pair production is mostly used to detect photons. Three modern gamma-ray telescopes sensitive to photons in the HE region are in orbit; they are called AGILE, *Fermi* Large Area Telescope (LAT) (Fig. 4.49), and DAMPE. Their technology has been inherited from the smaller and less technological EGRET instrument, operational in the years 1991–2000 on the Compton Gamma-Ray Observatory, and from particle physics. The direction of an incident photon is determined through the geometry of its conversion into an e^+e^- pair in foils of heavy materials which compose the instrument, and detected by planes of silicon detectors. The presence of an anticoincidence apparatus realizes a veto against unwanted incoming charged particles. The principle of operation is illustrated in Fig. 4.49, right.

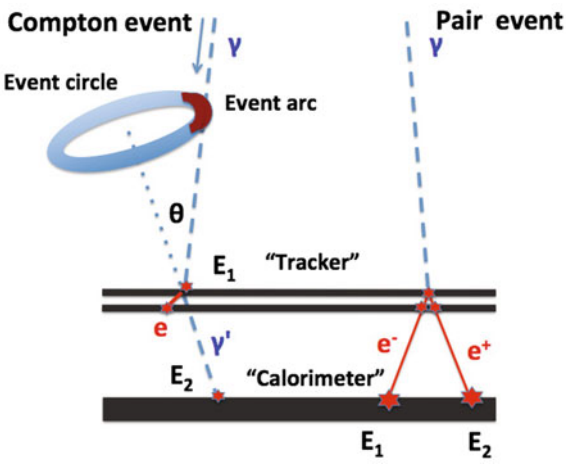

Fig. 4.48 Representative event topologies for a Compton event (left) and for a pair event (right). Photon tracks are shown in pale blue, dashed, and electron and/or positron tracks in red, solid. Courtesy of Alex Moiseev

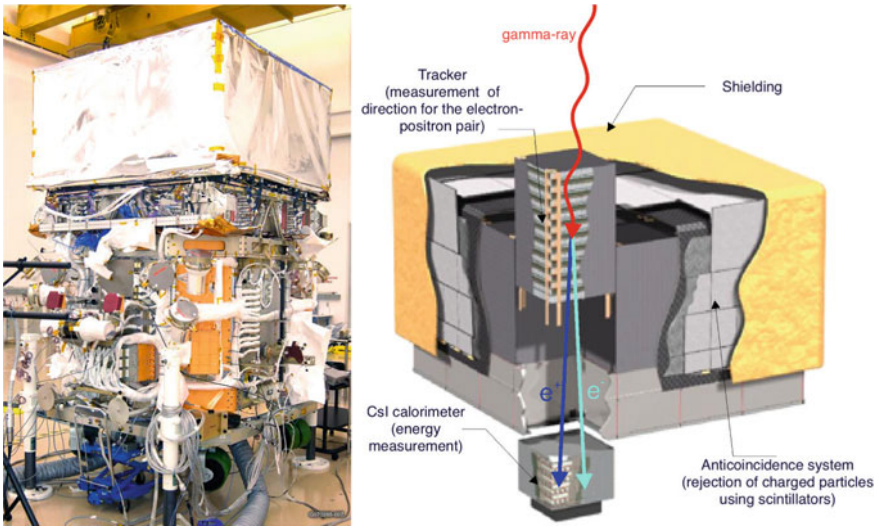

Fig. 4.49 On the left, the *Fermi* satellite. On the right, the layout of the Large Area Telescope (LAT), and principle of operation. Credits: NASA

The angular resolution of these telescopes is limited by the opening angle of the e^+e^- pair, approximately $0.8\,\text{MeV}/E$, and especially by the effect of multiple scattering. To achieve a good energy resolution, in this kind of detector, a calorimeter in the bottom of the tracker is possibly used, depending on the weight that the payload can comply with. Due to weight limitations, however, it is difficult to fit in a calorimeter that completely contains the showers; this leakage degrades the energy resolution. Since at low energies multiple scattering is the dominant process, the optimal detector design is a trade-off between small radiation length (which decreases the conversion efficiency) and large number of samplings (which increases the power consumption, limited by the problems of heat dissipation in space).

Fermi. The largest gamma-ray space-based detector ever built is up to now the *Fermi* observatory, launched in June 2008—and called GLAST before the successful positioning in orbit. It is composed of the spacecraft and two instruments: the Large Area Telescope (LAT) and the *Fermi* Gamma Burst Monitor (GBM); the two instruments are integrated and they work as a single observatory.

The structure of the LAT consists mainly of a tracker, an anticoincidence apparatus and a calorimeter (see Fig. 4.49). Its energy range goes from 20 MeV to about 300 GeV and above, while the energy range explored by the GBM is 10–25 MeV. *Fermi* was built and it is operated by an international collaboration with contributions from space agencies, high-energy particle physics institutes, and universities in France, Italy, Japan, Sweden, and the United States; it involves about 600 scientists. After the first year, data are public, i.e., every scientist in the world can in principle analyze them.

The scientific objectives of the LAT include the understanding of the nature of unidentified gamma-ray sources and origins of diffuse Galactic emission; of particle acceleration mechanisms at the sources, particularly in active galactic nuclei, pulsars, supernova remnants, and the Sun; of the high-energy behavior of gamma-ray burst and transient sources. The observations will also be used to probe dark matter and, at high energy, the early universe and the cosmic evolution of high-energy sources to redshift $z \sim 6$.

The characteristics and performance of the LAT are enabling significant progress in the understanding of the high-energy sky. In particular, it has good angular resolution for source localization and multiwavelength study, high sensitivity in a broad field of view to detect transients and monitor variability, good calorimetry over an extended energy band for detailed emission spectrum studies, and good calibration and stability for absolute, long-term flux measurements.

The LAT tracker is composed of 16 planes of high-Z material (W) in which incident γ rays can convert to an e^+e^- pair. The converter planes are interleaved with 18 two-layer planes of silicon detectors that measure the tracks of the particles resulting from pair conversion. This information is used to reconstruct the directions of the incident γ rays. After the tracker, a calorimeter can measure the energy. It is made of CsI(Tl) crystals with a total depth of 8.6 radiation lengths, arranged in a hodoscope configuration in order to provide longitudinal and transverse information on the energy deposition. The depth and the segmentation of the calorimeter enable the high-energy reach of the LAT and significantly contribute to background rejection. The aspect ratio of the tracker (height/width) is 0.4 (the width being about 1.7 m), resulting in a large field of view (2.4 sr) and ensuring that most pair-conversion showers initiated in the tracker will reach the calorimeter for energy measurement. Around the tracker, an anticoincidence detector (ACD) made of plastic scintillator provides charged particle background rejection.

The overall performance of *Fermi* can be summarized as follows in the region of main interest (30 MeV–30 GeV):

- Effective area of about $1\,\mathrm{m}^2$;
- Relative energy resolution decreasing between 10% at 100 MeV and 5% at 1 GeV, increasing again to 10% at 30 GeV;
- Angular resolution of 0.1° at 10 GeV, and approximately varying as $1/\sqrt{E}$.

AGILE, the precursor of *Fermi*, is a completely Italian satellite launched in April 2007. Its structure is very similar to *Fermi*, but its effective area is about one order of magnitude smaller. However, many remarkable physics results were obtained thanks to the AGILE data.

Finally DAMPE, launched in 2015, has also a structure and an effective area similar to AGILE. It is however characterized by an imaging calorimeter of about 31 radiation lengths thickness, made up of 14 layers of Bismuth Germanium Oxide (BGO) bars in a hodoscopic arrangement—this is the deepest calorimeter ever used in space.

4.5.3.2 Ground-Based Gamma-Ray Detectors

Ground-based VHE gamma-ray detectors–such as HAWC, H.E.S.S., MAGIC, and VERITAS–detect the atmospheric showers produced by primary photons and cosmic rays of energy higher than those observed by satellites.

The two kinds of detectors (on satellite and at the ground) are complementary. At energies below 1 GeV or so, the showers generated by photons do not have the time to develop properly, and thus the only way to detect photons below this energy is with the use of satellites. At TeV energies, however, the flux is too low to be detected with satellite-based detectors: due to their cost, and in particular to the cost of the launch, the satellites have areas of the order of $1\,\mathrm{m}^2$ at most, and at these energies even the most luminous gamma-ray sources have a flux smaller than one photon per square meter every ten hours. Ground-based detectors have a huge effective area, so their sensitivity is high; they detect a huge amount of background events, but they have low cost.

The main problem of ground-based detection is the rejection of the background from showers generated by protons. As an example to evaluate the entity of the problem, we consider a source with an emission energy distribution like the Crab Nebula, a nearby (∼2 kpc away) pulsar wind nebula and the first source detected in VHE gamma rays, and the brightest VHE gamma-ray source visible from both hemispheres—therefore, it has become the so-called *standard reference* in VHE gamma-ray astronomy.

The *stationary* flux from the Crab Nebula in the region from some 20 GeV to about 100 TeV follows approximately a function

$$\frac{dN_\gamma}{dE} \simeq 3.23 \times 10^{-7} \left(\frac{E}{\mathrm{TeV}}\right)^{-2.47-0.24\left(\frac{E}{\mathrm{TeV}}\right)} \mathrm{TeV}^{-1}\mathrm{s}^{-1}\mathrm{m}^{-2}\,. \tag{4.22}$$

The spectral energy distribution of background cosmic rays can be approximated as

$$\frac{dN}{dE} \simeq 1.8 \times 10^4 \left(\frac{E}{\mathrm{GeV}}\right)^{-2.7} \mathrm{GeV}^{-1}\mathrm{s}^{-1}\mathrm{sr}^{-1}\mathrm{m}^{-2}\,; \tag{4.23}$$

the approximation is valid from some 10 GeV to about 1 PeV.

The number of photons from the Crab per m^2 per second above a given threshold is shown in Fig. 4.50, and compared to the background from cosmic rays in a square degree. From this it becomes clear that in order to separate the gamma-ray signal from the background the angular resolution should be of one degree or better, and possibly there should be a way to distinguish electromagnetic showers from hadronic showers (e.g., by their topology or by the presence of muons in hadronic showers).

There are two main classes of ground-based VHE gamma-ray detectors: the EAS arrays and the Cherenkov telescopes (see Fig. 4.51).

EAS Detectors. The EAS detectors, such as MILAGRO, Tibet-AS and ARGO-YBJ in the past, and HAWC which is presently in operation, are large arrays of detectors

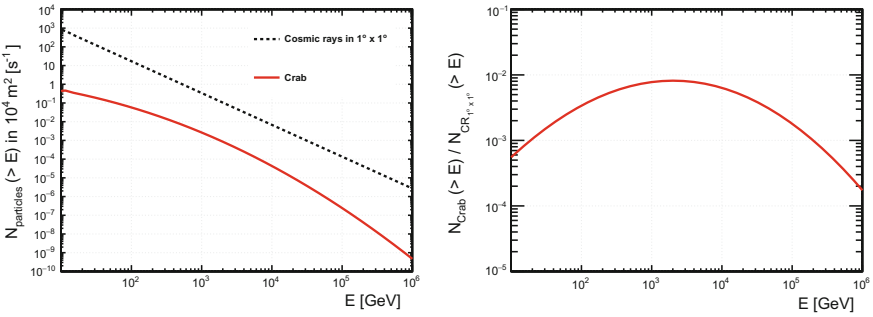

Fig. 4.50 Left: Signal above a given energy on an effective area of 10 000 m^2, integrated over 1 s: Crab (solid line) and background from charged cosmic rays within one square degree (dashed line). Right: ratio signal/background from the plot on the left

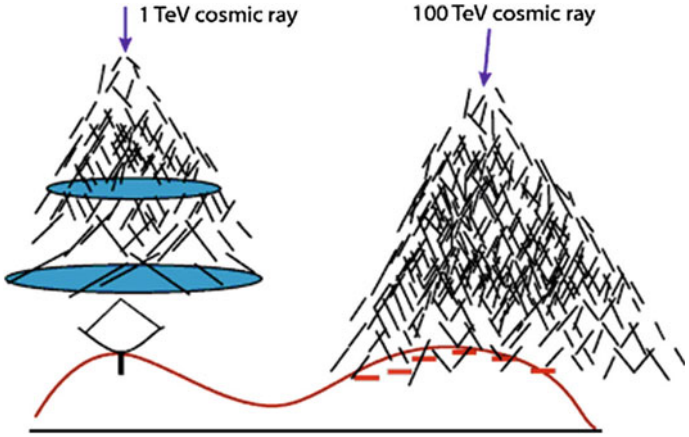

Fig. 4.51 Sketch of the operation of Cherenkov telescopes and of EAS detectors

sensitive to charged secondary particles generated in the atmospheric showers. They have a high duty cycle and a large field of view, but a relatively poor sensitivity. The energy threshold of such detectors is rather large—a shower initiated by a 1 TeV photon typically has its maximum at about 8 km a.s.l.

The principle of operation is the same as the one for the UHE cosmic rays detectors like Auger, i.e., direct sampling of the charged particles in the shower. This can be achieved:

- either using a sparse array of scintillator-based detectors, as, for example, in Tibet-AS (located at 4100 m a.s.l. to reduce the threshold; for an energy of 100 TeV there are about 50 000 electrons at mountain-top altitudes);
- or by effective covering of the ground, to ensure efficient collection and hence lower the energy threshold.

– The ARGO-YBJ detector at the Tibet site followed this approach. It was an array of resistive plate counters. Its energy threshold was in the 0.5–1 TeV range. The Crab Nebula could be detected with a significance of about 5 standard deviations (σ) in 50 days of observation.
– MILAGRO was a water Cherenkov instrument located in New Mexico (at an altitude of about 2600 m a.s.l.). It detected the Cherenkov light produced by the secondary particles of the shower when entering the water pool instrumented with photomultipliers. MILAGRO could detect the Crab Nebula with a significance of about $5\,\sigma$ in 100 days of observation, at a median energy of about 20 TeV.

The energy threshold of EAS detectors is at best in the 0.5–1 TeV range, so they are built to detect UHE photons as well as the most energetic VHE gamma rays. At such energies fluxes are small and large effective areas of the order of $10^4\,\mathrm{m}^2$ are required. We remind here that the effective area is the product of the collection area times the detection efficiency; the collection area can be larger than the area covered by the detector, since one can detect showers partially contained—this fact is more relevant for Cherenkov telescopes, see later.

Concerning the discrimination from the charged cosmic ray background, muon detectors devoted to hadron rejection may be present. Otherwise, this discrimination is based on the reconstructed shower shape. The direction of the detected primary particles is computed from the arrival times with an angular precision of about 1° to 2°. The calibration can be performed by studying the shadow in the reconstructed directions caused by the Moon. Energy resolution is poor.

Somehow, the past generation EAS detectors were not sensitive enough and just detected a handful of sources. This lesson led to a new EAS observatory with much better sensitivity: the High Altitude Water Cherenkov detector HAWC, inaugurated in 2015.

HAWC (Fig. 4.52) is a very high-energy gamma-ray observatory located in Mexico at an altitude of 4100 m. It consists of 300 steel tanks of 7.3 m diameter and 4.5 m deep, covering an instrumented area of about $22\,000\,\mathrm{m}^2$. Each tank is filled with purified water and contains three PMTs of 20 cm diameter, which observe the Cherenkov light emitted in water by superluminal particles in atmospheric air showers. Photons traveling through the water typically undergo Compton scattering or produce an electron–positron pair, also resulting in Cherenkov light emission. This is an advantage of the water Cherenkov technique, as photons constitute a large fraction of the electromagnetic component of an air shower at ground.

HAWC improves the sensitivity for a Crab-like spectrum by a factor of 15 compared to MILAGRO. The sensitivity should be good enough to possibly detect gamma-ray burst emissions at high energy.

A future installation in the Northern hemisphere, a hybrid detector called LHAASO, is in construction in China. LHAASO covers a total area of about $10^6\,\mathrm{m}^2$ with more than 5000 scintillation detectors, each of $1\,\mathrm{m}^2$ area. A central detector of 80 000 square meters (four times the HAWC detector) of surface water pools is equipped with PMTs to study gamma-ray astronomy in the sub-TeV/TeV energy

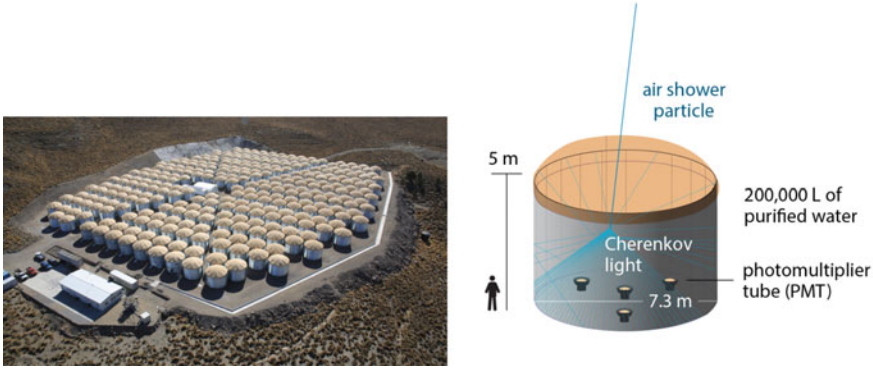

Fig. 4.52 Left: The HAWC detector. Right: Sketch of a water tank. Credit: HAWC Collaboration

range. About 1200 water tanks underground, with a total sensitive area of about 42 000 m^2, pick out muons, to separate gamma-ray initiated showers from hadronic showers. 18 wide field-of-view Cherenkov telescopes will complete the observatory. LHAASO will have the best sensitivity on gamma-ray initiated showers above some 10 TeV. One-quarter of the observatory should be ready by 2018, and completion is expected in 2021.

Cherenkov Telescopes. Most of the experimental results on VHE photons are presently due to Imaging Atmospheric Cherenkov Telescopes (IACTs), which detect the Cherenkov photons produced in air by charged, locally superluminal particles in atmospheric showers.

WHIPPLE in Arizona was the first IACT to see a significant signal (from the Crab Nebula, in 1989). The second-generation instruments HEGRA and CANGAROO improved the technology, and presently the third-generation instruments H.E.S.S. in Namibia, MAGIC in the Canary Islands and VERITAS in Arizona are running smoothly and detecting tens of sources every year. For reasons explained below, these instruments have a low duty cycle (about 1000–1500 h/year) and a small field of view (FoV), but they have a high sensitivity and a low energy threshold.

The observational technique used by the IACTs is to project the Cherenkov light collected by a large optical reflector onto a focal camera which is basically an array of photomultipliers, with a typical quantum efficiency of about 30%, in the focal plane of the reflector (see Fig. 4.53). The camera has a typical diameter of about 1 m, and covers a FoV of about $5° \times 5°$. The signal collected by the camera is analogically transmitted to trigger systems, similar to the ones used in high-energy physics. The events which pass the trigger levels are sent to the data acquisition system, which typically operates at a frequency of a few hundreds Hz. The typical resolution on the arrival time of a signal on a photomultiplier is better than 1 ns.

The shower has a duration of a few ns (about 2–3) at ground; this duration can be kept by an isochronous (parabolic) reflector.

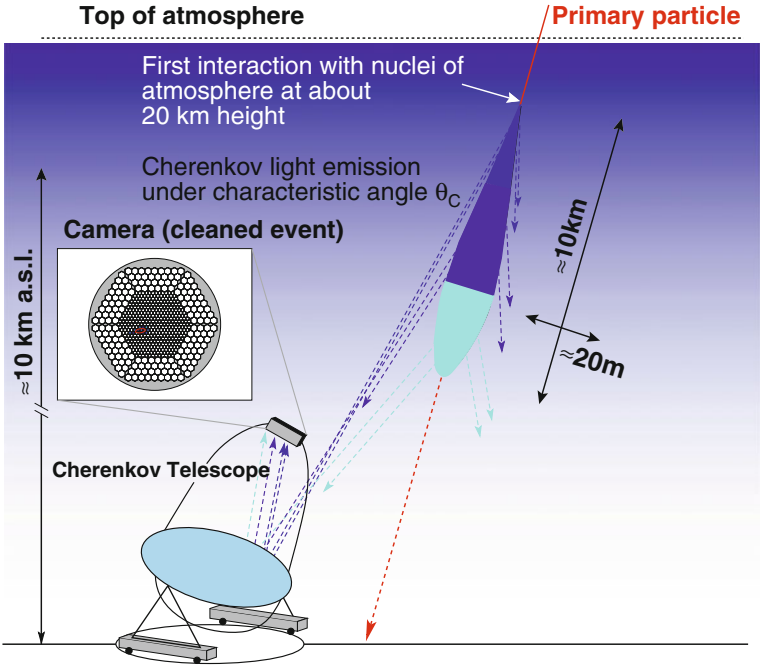

Fig. 4.53 Observational technique adopted by Cherenkov telescopes. From R.M. Wagner, dissertation, MPI Munich 2007

Since, as discussed above, about 10 photons per square meter arrive in the light pool for a primary photon of 100 GeV, a light collector of area 100 m^2 is sufficient to detect gamma-ray showers if placed at mountain-top altitudes. Due to the faintness of the signal, data can typically be taken only in moonless time, or with moderate moonlight, and without clouds, which limits the total observation time to some 1000–1500 h/year.

In the GeV–TeV region, the background from charged particles is three orders of magnitude larger than the signal. Hadronic showers, however, have a different topology, being larger and more subject to fluctuations than electromagnetic showers. Most of the present identification techniques rely on a technique pioneered by Hillas in the 1980s; the discriminating variables are called "Hillas parameters." The intensity (and area) of the image produced provide an estimate of the shower energy, while the image orientation is related to the shower direction (photons "point" to emission sources, while hadrons are in first approximation isotropic). The shape of the image is different for events produced by photons and by other particles; this characteristic can be used to reject the background from charged particles (Figs. 4.54 and 4.55).

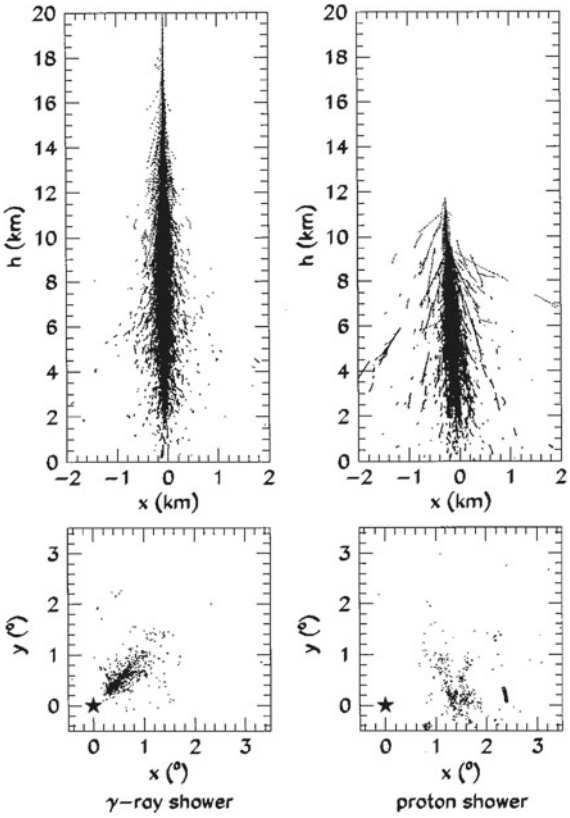

Fig. 4.54 Development of a vertical 1 TeV photon (left) and proton (right) showers in the atmosphere. The upper panels show the positions in the atmosphere of all shower electrons above the Cherenkov threshold; the lower panels show the resulting Cherenkov images in the focal plane of a 10 m reflecting mirror when the showers fall 100 m from the detector (the center of the focal plane is indicated by a star). From C.M. Hoffmann et al., "Gamma-ray astronomy at high energies," Reviews of Modern Physics 71 (1999) 897

The time structure of Cherenkov images provides an additional discriminator against the hadronic background, which can be used by isochronous detectors (with parabolic shape) and with a signal integration time smaller than the duration of the shower (i.e., better than 1–2 GHz).

Systems of more than one Cherenkov telescope provide a better background rejection, and a better angular and energy resolution than a single telescope.

There are three large operating IACTs: H.E.S.S., MAGIC, and VERITAS; the first located in the Southern hemisphere and the last two in the Northern hemisphere.

- The H.E.S.S. observatory (Fig. 4.56) in Namibia is composed of four telescopes with a diameter of 12 m each, working since early 2003. A fifth large telescope, a surface of about 600 m^2, is located in the center; it was inaugurated in 2012.

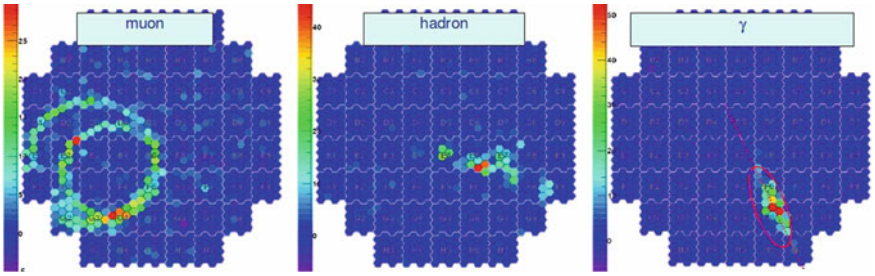

Fig. 4.55 Images from the focal camera of a Cherenkov telescope. The electromagnetic events differ from the hadronic events by several features: the envelope of the electromagnetic shower can be quite well described by an ellipse whereas the important fraction of large transverse momentum particles in hadronic showers will result in a more scattered reconstructed image. Muons are characterized by a conical section. From http://www.isdc.unige.ch/cta/images/outreach/

Fig. 4.56 The H.E.S.S. telescopes. Credit: H.E.S.S. Collaboration

- The MAGIC observatory (Fig. 4.57) in the Canary Island of La Palma is a twin telescope system; each parabola has a diameter of 17 m and a reflecting surface of $236\,m^2$.
- VERITAS is constituted by an array of four telescopes with a diameter of 12 m and is located near Tucson, Arizona. It is operational since April 2007.

These instruments are managed by international collaborations of some 150 scientists.

Typical sensitivities of H.E.S.S., MAGIC, and VERITAS are such that a source less than 1% of the flux of the Crab Nebula can be detected at a 5σ significance in 50 h of observation.

An overlap in the regions of the sky explored by the IACTs allows an almost continuous observation of sources placed at midlatitude; there is, however, space for two more installations, one in South America and one (MACE, in construction) in India.

Agreements between the Cherenkov telescopes and *Fermi* allow a balance between competition and cooperation.

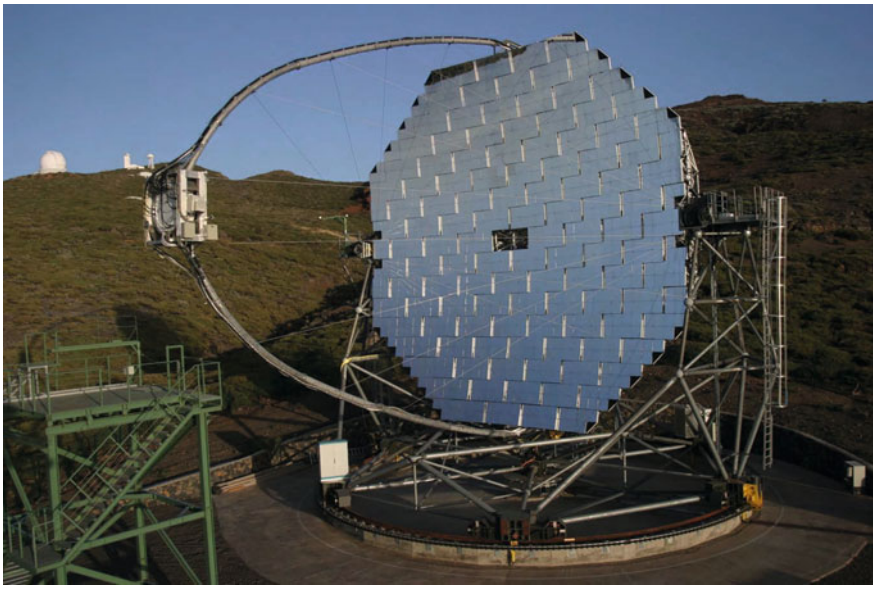

Fig. 4.57 One of the MAGIC telescopes. Credit: Robert Wagner, University of Stockholm

Table 4.5 A comparison of the characteristics of *Fermi*, the IACTs and of the EAS particle detector arrays. Sensitivity computed over one year for *Fermi* and the EAS, and over 50 h for the IACTs

Quantity	*Fermi*	IACTs	EAS
Energy range	20 MeV–200 GeV	100 GeV–50 TeV	400 GeV–100 TeV
Energy res.	5–10%	15–20%	∼50%
Duty cycle	80%	15%	>90%
FoV	$4\pi/5$	$5° \times 5°$	$4\pi/6$
PSF (deg)	0.1	0.07	0.5
Sensitivity	1% Crab (1 GeV)	1% Crab (0.5 TeV)	0.5 Crab (5 TeV)

4.5.3.3 Summary of the Performance of Gamma-Ray Detectors

A simplified comparison of the characteristics of the *Fermi* LAT satellite detector, of the IACTs and of the EAS detectors (ground-based), is shown in Table 4.5. The sensitivities of the above described high-energy detectors are shown in Fig. 4.58.

A Cherenkov Telescope: MAGIC. We shall now describe in larger detail one of the Cherenkov telescopes: MAGIC. The MAGIC experiment, located at an altitude of 2200 m a.s.l. on the Canary island of La Palma, is composed of two 17 m diameter IACTs devoted to the observation of VHE gamma rays with a lower energy threshold of 30 GeV. The first of the MAGIC telescopes started operations in 2004; the second was built some years later allowing stereo observations since autumn 2009.

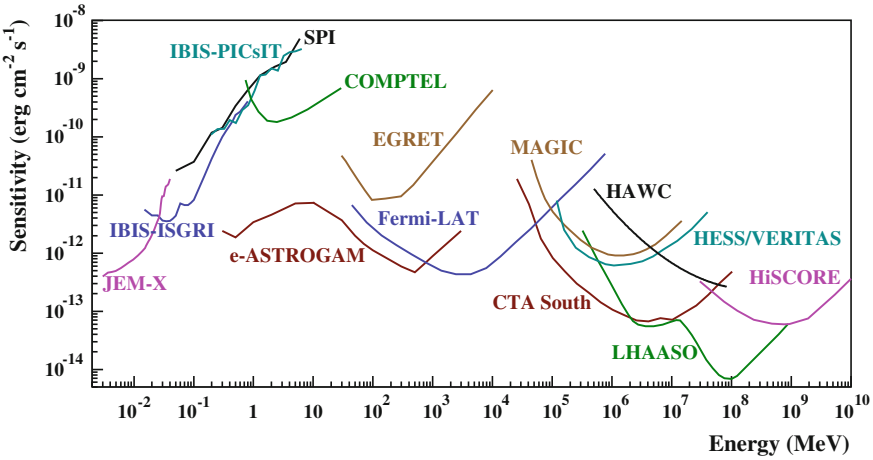

Fig. 4.58 Point source continuum differential sensitivity of different X- and γ-ray instruments. The curves for *INTEGRAL*/JEM-X, IBIS (ISGRI and PICsIT), and SPI are for an effective observation time $T_{\rm obs} = 1$ Ms. The COMPTEL and EGRET sensitivities are given for the typical observation time accumulated during the ~9 years of the CGRO mission. The *Fermi*/LAT sensitivity is for a high Galactic latitude source in 10 years of observation in survey mode. For MAGIC, H.E.S.S./VERITAS, and CTA, the sensitivities are given for $T_{\rm obs} = 50$ h. For HAWC $T_{\rm obs} = 5$ year, for LHAASO $T_{\rm obs} = 1$ year, and for HiSCORE $T_{\rm obs} = 1000$ h. The e-ASTROGAM sensitivity is calculated at 3σ for an effective exposure of 1 year and for a source at high Galactic latitude. Compilation by V. Tatischeff

MAGIC II was constructed like a copy of MAGIC I with a few improvements. Both are built using a lightweight carbon-fiber structure, and the size of the mirror dish (17 m diameter) and the camera field of view (3.5°) are the same. Each MAGIC camera is composed of 1039 0.1° hexagonal pixels (a hexagonal reflecting cone, called Winston cone, collecting the light onto a photomultiplier).

The reflectors are made of square mirrors with a curved surface; each mirror is 1 m^2 in size. Their position can be corrected thanks to an automatic mirror control (AMC) in such a way that they point to the focal camera.

In both telescopes the signals from the PMT in each pixel are optically transmitted to the countinghouse where trigger and digitization of the signals take place. The signals of both telescopes are digitized using a frequency of 2 GSample/s.

Regular observations are performed in stereoscopic mode. Only events that trigger both telescopes are recorded. The trigger condition for the individual telescope (level-0 trigger) is that at least 3 neighboring pixels must be above their pixel threshold. The stereo trigger makes a tight time coincidence between both telescopes taking into account the delay due to the relative position of the telescopes and their pointing direction. Although the individual telescope trigger rates are of several kHz, the stereo trigger rate is in the range of 150–200 Hz with just a few Hz being accidental triggers. The lower observational threshold can be reduced to 30 GeV thanks to a dedicated low-energy trigger.

4.5.3.4 Future Detectors for High-Energy Photons

It is difficult to think for this century of an instrument for GeV photons improving substantially the performance of the *Fermi* LAT: the cost of space missions is such that the size of *Fermi* cannot be reasonably overcome with present technologies. New satellites already approved (like the Chinese-Italian mission HERD, for which launch is expected after 2024) will improve some of the aspects of *Fermi*, – in this particular case, calorimetry.

Improvements are possible in the sectors of:

- **keV astrophysics**. The launch of ATHENA is foreseen in 2028 and will improve the sensitivity by two orders of magnitude.
- **MeV astrophysics**. The possible launches of e-ASTROGAM and/or AMEGO in 2028/29 will improve the sensitivity by two orders of magnitude, with a comparable improvement in the quality of data (localization accuracy, measurement of polarization, etc.).
- **TeV gamma-ray astrophysics**. VHE gamma-ray astrophysics in the current era has been dominated by Cherenkov telescopes. We know today that the previous generation EAS telescopes were underdimensioned in relation to the strength of the sources.

  The research in the future will push both on EAS and IACT, which have mutual advantages and disadvantages. The sensitivities of the main present and future detectors are illustrated in Fig. 4.58. We have already seen the characteristics of HAWC, which is under upgrade with the construction of an outrigger; a very large Cherenkov Telescope Array (CTA) is also in construction.

  The CTA is a future observatory for VHE gamma-ray astrophysics that is expected to provide an order of magnitude improvement in sensitivity over existing instruments.

  An array of tens of telescopes will detect gamma-ray-induced showers over a large area on the ground, increasing the efficiency and the sensitivity, while providing a much larger number of views of each cascade. This will result in both improved angular resolution and better suppression of charged cosmic-ray background events. Three types of telescopes are foreseen:

  – The low-energy (the goal is to detect showers starting from an energy of 20 GeV) instrumentation will consist of 23 m large-size telescopes (LST) with a FoV of about 4–5°.
  – The medium energy range, from around 100 GeV–1 TeV, will be covered by medium-size telescopes (MST) of the 12 m class with a FoV of 6–8°.
  – The high-energy instruments, dominating the performance above 10 TeV, will be small size (SST, 4–6 m in diameter) telescopes with a FoV of around 10°.

  CTA will be deployed in two sites. The Southern hemisphere site is less than 10 km from the Paranal Observatory in the Atacama Desert in Chile; it will cover about three square kilometers of land with telescopes that will monitor all the energy ranges in the center of the Milky Way's Galactic plane. It will consist of all three

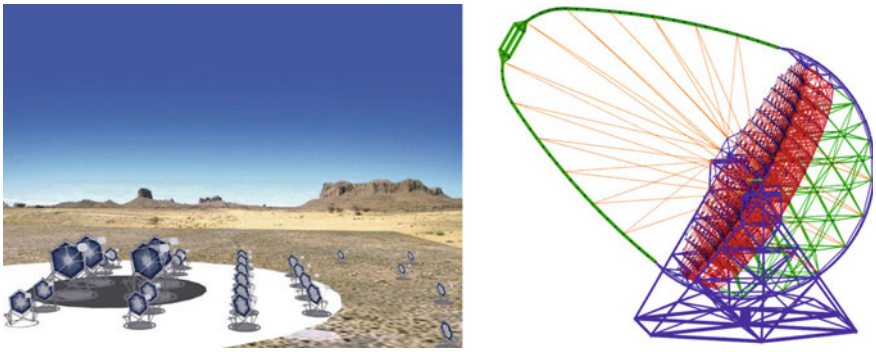

Fig. 4.59 Left: Possible layout of the CTA. Right: Project of the large telescope (LST). Credit: CTA Collaboration

types of telescopes with different mirror sizes (4 LSTs, 25 MSTs, and 70 SSTs in the present design). The Northern hemisphere site is located on the existing Roque de los Muchachos Observatory on the Canary island of La Palma, close to MAGIC; only the two larger telescope types (4 LSTs and 15 MSTs in the present design) would be deployed, on a surface of about one square kilometer. These telescopes will be mostly targeted at extragalactic astronomy. The telescopes of different sizes will be arranged in concentric circles, the largest in the center (Fig. 4.59).
Different modes of operation will be possible for CTA: deep field observation; pointing mode; scanning mode—also pointing to different targets.

- **PeV gamma-ray astrophysics**. Besides LHAASO, already in construction in the Northern hemisphere, another large-FoV detector is in construction in Russia, called HiSCORE (Hundred Square-km Cosmic ORigin Explorer). Together with a system of Cherenkov telescopes, HiSCORE should form the hybrid array TAIGA. There is a strong case for a PeV wide-FoV detector in the Southern hemisphere in order to study the highest-energy emissions of accelerators in the Galaxy. Several collaborations are proposing designs for such a detector, and convergence could be reached in the next years.

4.5.4 Neutrino Detection

The energy spectrum of neutrinos interesting for particle and astroparticle physics spans more than 20 orders of magnitude, from the $\sim$2 K ($\sim$0.2 meV) of relic neutrinos from the big bang, to the MeV of reactors, to the few MeV of the solar neutrinos, to the few GeV of the neutrinos produced by the interaction of cosmic rays with the atmosphere (atmospheric neutrinos), to the region of extremely high energy where the production from astrophysical sources is dominant. We concentrate here

on the detection of neutrinos of at least some MeV, and we present some of the most important neutrino detectors operating.

Since neutrino cross section is small, it is important that neutrino detectors be located underground or underwater to shield from cosmic rays.

4.5.4.1 MeV Neutrinos

Detectors of neutrinos in the MeV range mostly use the detection of the products of induced β decays. The first setups used a solution of cadmium chloride in water and two scintillation detectors as a veto against charged cosmic rays. Antineutrinos with an energy above the 1.8 MeV threshold can cause inverse beta decay interactions with protons in water, producing a positron which in turn annihilates, generating photon pairs that can be detected.

Radiochemical chlorine detectors consist instead of a tank filled with a chlorine solution in a fluid. A neutrino converts a ^{37}Cl atom into a ^{37}Ar; the threshold neutrino energy for this reaction is 0.814 MeV. From time to time the argon atoms are counted to measure the number of radioactive decays. The first detection of solar neutrinos was achieved using a chlorine detector containing 470 tons of fluid in the former Homestake Mine near Lead, South Dakota. This measurement evidenced a deficit of electron neutrinos from what expected by the power radiated from the Sun. For this discovery the leader of the experiment, Ray Davis, won the Nobel Prize in physics.[19] A similar detector design, with a lower detection threshold of 0.233 MeV, uses the Ga $\rightarrow$ Ge transition.

4.5.4.2 MeV to GeV Neutrinos

Probably the most important results in the sector of MeV to GeV neutrinos in the recent years are due to a Cherenkov-based neutrino detector, Kamiokande, in Japan. We give here a short description of this detector in its present version, called Super-Kamiokande.

The Super-Kamiokande Detector. Super-Kamiokande (often abbreviated to Super-K or SK) is a neutrino observatory located in a mine 1000 m underground under Mount Kamioka near the city of Hida, Japan. The observatory was initially designed to search for proton decay, predicted by several unification theories (see Sect. 7.6.1).

Super-K (Fig. 4.60) consists of a cylindrical tank about 40 m tall and 40 m in diameter containing 50 000 tons of ultrapure water. The volume is divided by a stainless steel structure into an inner detector (ID) region (33.8 m in diameter and 36.2 m in height) and an outer detector (OD) consisting of the remaining tank volume.

[19] One half of the Nobel Prize in physics 2002 was awarded jointly to the US physicist Raymond Davis Jr. (Washington 1914—New York 2006) and to the leader of the Kamiokande collaboration (see later) Masatoshi Koshiba (Aichi, Japan, 1926) "for pioneering contributions to astrophysics, in particular for the detection of cosmic neutrinos."

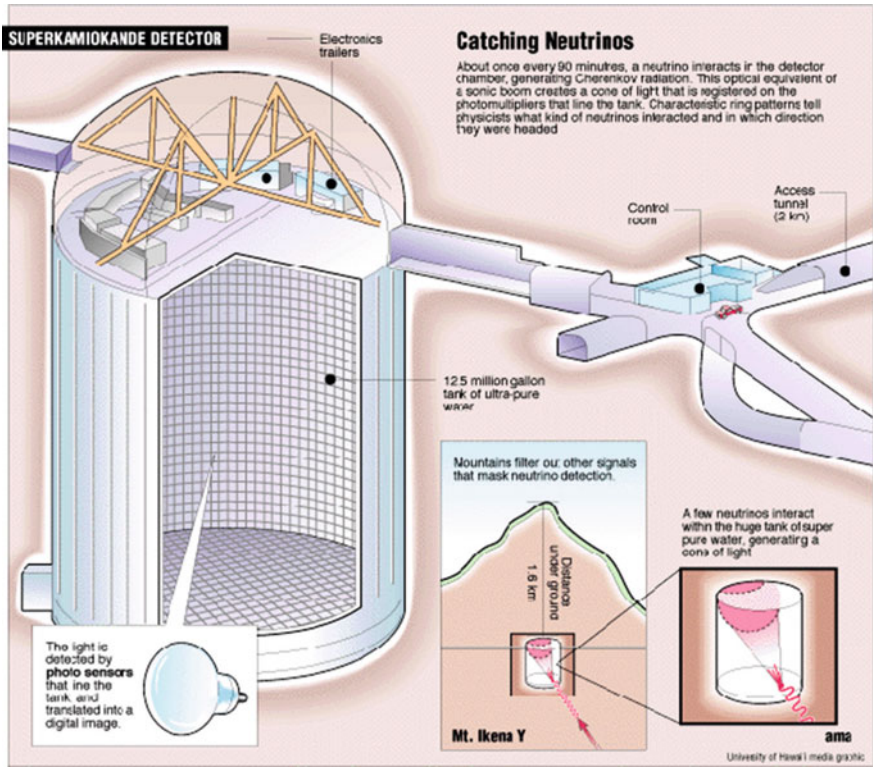

Fig. 4.60 The Super-Kamiokande detector. Credit: Super-Kamiokande Collaboration

Mounted on the structure are about 11 000 PMT 50 cm in diameter that face the ID and 2000 20 cm PMT facing the OD.

The interaction of a neutrino with the electrons or nuclei in the water can produce a superluminal charged particle generating Cherenkov radiation, which is projected as a ring on the wall of the detector and recorded by a PMT. The information recorded is the timing and charge information by each PMT, from which one can reconstruct the interaction vertex, the direction and the size of the cone.

Typical threshold for the detection of electron neutrinos is of about 6 MeV. Electrons lose quickly their energy, and, if generated in the ID, are likely to be fully contained (not penetrating inside the OD). Muons instead can penetrate, and the muon events can be partially contained (or not) in the detector. The threshold for the detection of muon neutrinos is about 2 GeV.

A new detector called Hyper-Kamiokande is envisaged, with a volume 20 times larger than Super-Kamiokande. Construction is expected to start around 2020, and to take about seven years.

The SNO Detector. The Sudbury Neutrino Observatory (SNO) used 1000 tons of heavy water (D_2O) contained in a 12 m diameter spherical vessel surrounded by a

cylinder of ordinary water, 22 m in diameter and 34 m high. In addition to the neutrino interactions visible in a detector as SK, the presence of deuterium allows the reaction producing a neutron, which is captured releasing a gamma-ray that can be detected. SNO was recently upgraded to SNO+, using the same sphere filled with a liquid scintillator (linear alkylbenzene) to act as detector and target material.

4.5.4.3 Very-High-Energy Neutrinos

Very-high-energy neutrinos are expected to be produced in astrophysical objects by the decays of charged pions produced in primary cosmic ray interactions with radiation or molecular clouds in astrophysical objects (this is called "hadronic" mechanism). As these pions decay, they produce neutrinos with typical energies one order of magnitude smaller than those of the cosmic-ray nucleons—more or less the same energies as photons. These neutrinos can travel long distances undisturbed by either the absorption experienced by high-energy photons or the magnetic deflection experienced by charged particles, making them a unique tracer of cosmic-ray acceleration. Additional sources can be the interactions of cosmic rays with the atmosphere (atmospheric neutrinos), and decays of heavier particles formed by the interaction of cosmic rays with the CMB, or decays of new, heavy particles.

Above an energy of 100 TeV, the expected atmospheric neutrino background falls to the level of one event per year per cubic kilometer, and any (harder) astrophysical flux can be clearly seen.

The challenge in the field of UHE neutrinos is to build telescopes with good enough sensitivity to see events, since the flux is expected to be lower than the photon flux (the main mechanism for the production of neutrinos, i.e., the hadronic mechanism, is common to photons, which in addition can be produced via a "leptonic" mechanism, as we shall see in Chap. 10). This requires instrumenting very large volumes. Efforts to use large quantities of water and ice as detectors are ongoing. Several experiments are completed, operating, or in development using Antarctic ice, the oceans, and lakes, with detection methods including optical and coherent radio detection as well as particle production.

Among the experiments in operation, the largest sensitivity detectors are Baikal NT-200 and IceCube.

Baikal NT-200 Detector. The underwater neutrino telescope NT-200 is located in the Siberian lake Baikal at a depth of approximately 1 km and is taking data since 1998. When ultimated, it will consist of 192 optical sensors deployed in eight strings, with a total active volume of 5 million cubic meters. Deployment and maintenance are carried out during winter, when the lake is covered with a thick ice sheet and the sensors can easily be lowered into the water underneath. Data are collected over the whole year and permanently transmitted to the shore over electrical cables.

The IceCube Experiment. IceCube, a cube of 1 km^3 instrumented in the Antarctica ices, has been in operation at the South Pole since 2010 (Fig. 4.61). The telescope views the ice through approximately 5160 sensors called digital optical modules

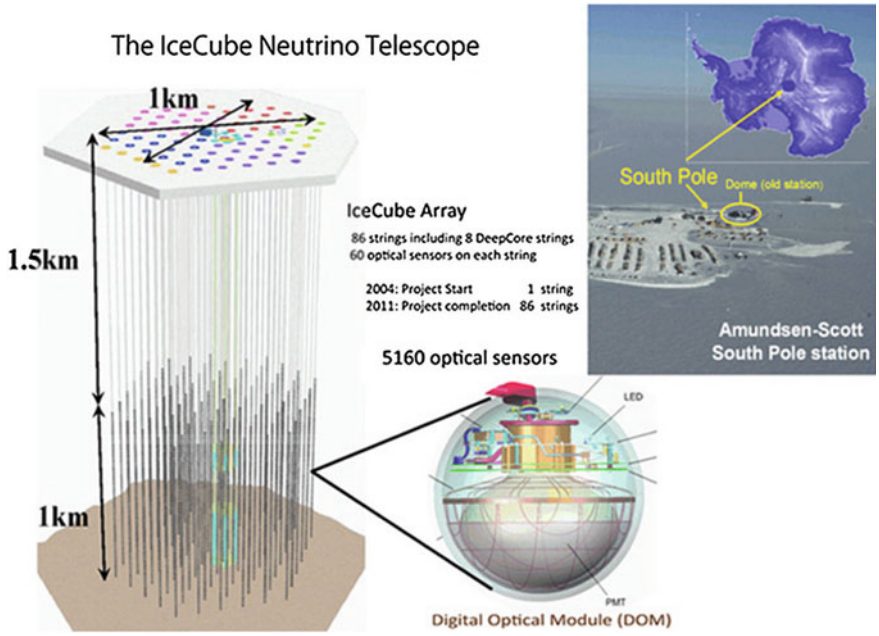

Fig. 4.61 The IceCube detector. Credit: http://www.icehap.chiba-u.jp/en/frontier/

(DOMs). The DOMs are attached to vertical strings, frozen into 86 boreholes, and arrayed over a cubic kilometer from 1 450 to 2 450 m depth. The strings are deployed on a hexagonal grid with 125 m spacing and hold 60 DOMs each. The vertical separation of the DOMs is 17 m. Eight of these strings at the center of the array were deployed more compactly, with a horizontal separation of about 70 m and a vertical DOM spacing of 7 m. This denser configuration forms the DeepCore subdetector, which lowers the neutrino energy threshold to about 10 GeV, creating the opportunity to study neutrino oscillations. At the surface, an air shower array is coupled to the detector. As the Earth is opaque to UHE neutrinos, detection of extremely high-energy neutrinos must come from neutrinos incident at or above the horizon, while intermediate energy neutrinos are more likely to be seen from below.

IceCube detects a dozen of very-high-energy events per year consistent with astrophysical sources. The IceCube sensitivity will soon reach the high-energy neutrino fluxes predicted in cosmogenic neutrino models.

KM3NeT. A large underwater neutrino detector, KM3NeT, is planned. KM3NeT will host a neutrino telescope with a volume of several cubic kilometers at the bottom of the Mediterranean sea. This telescope is foreseen to contain of the order of 12 000 pressure-resistant glass spheres attached to about 300 detection units—vertical structures with nearly one kilometer in height. Each glass sphere will contain 31 photomultipliers and be connected to shore via a high-bandwidth optical link. At shore, a computer farm will perform the first data filtering in the search for the signal of

cosmic neutrinos. KM3NeT builds on the experience of three pilot projects in the Mediterranean sea: the ANTARES detector near Marseille, the NEMO project in Sicily, and the NESTOR project in Greece. ANTARES was completed in 2008 and is the largest neutrino telescope in the Northern hemisphere.

4.6 Detection of Gravitational Waves

Gravitational waves are generated by aspherical motions of matter distributions; they propagate at the speed of light, bringing curvature of space–time information. Their effect on matter is to change the relative distances. This effect is however small, and even the most violent astrophysical phenomena (e.g., colliding black holes or neutron stars, collapsing stars) emit gravitational waves which, given the typical distance to the event, are expected to cause relative shifts on distances of only 10^{-20} on Earth. In fact, gravitational waves were predicted by Albert Einstein in his theory of general relativity roughly 100 years ago, but only recently has technology enabled us to detect them.

A figure of merit for a detector is the space strain ℓ:

$$\Delta L/L \sim \ell$$

where L is the distance between the two masses and ΔL is its variation. Another one is the horizon distance, i.e., the maximum range out to which it could see the coalescence of two 1.4 $M_\odot$ neutron stars.

The idea explored first to detect gravitational waves was to detect the elastic energy induced by the compression/relaxation of a metal bar due to the compression/relaxation of distance. Detectors were metal cylinders, and the energy converted to longitudinal oscillations of the bar was measured by piezoelectric transducers. The first large gravitational wave detector, built by Joseph Weber in the early 1960s, was a 1.2 ton aluminum cylindrical bar of 1.5 m length and 61 cm diameter (Fig. 4.62) working at room temperature and isolated as much as possible from acoustic and ground vibrations. The mechanical oscillation of the bar was translated into electric signals by piezoelectric sensors placed in its surface close to the central region. The detector behaved as a narrow band high$-Q$ (quality factor) mechanical resonator with a central frequency of about 1600 Hz. The attenuation of the oscillations is, in such devices, very small and therefore the bar should oscillate for long periods well after the excitation induced by the gravitational waves. The sensitivity of Weber's gravitational antenna was of the order of $\ell \sim 10^{-16}$ over timescales of 10^{-3} s. Bar detectors (ALLEGRO, AURIGA, Nautilus, Explorer, Niobe) reached sensitivities of $\ell \sim 10^{-21}$, thanks to the introduction of cryogenic techniques which allow for a substantial reduction in the thermal noise as well as the use of very performing superconducting sensors. However, their frequency bandwidths remain very narrow ($\sim$tens of Hz) and the resonant frequencies ($\sim$1 kHz) correspond typically to acoustic wavelengths of the order of the detector length. A further increase in sensitivity

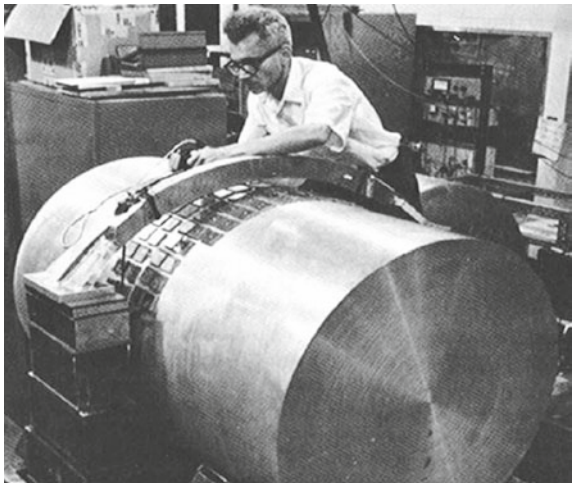

Fig. 4.62 Joseph Weber working on his gravitational antenna (1965). From http://www.physics.umd.edu/

implies a particular attention to the quantum noise, and thus a considerable increase of the detector mass (bars with hundred tons of mass are being considered).

Nowadays the most sensitive detectors are Michelson-type interferometers with kilometer-long arms and very stable laser beams (see Fig. 4.63). Resonant Fabry–Perot cavities are installed along their arms in a way that the light beams suffer multiple reflections increasing by a large factor the effective arm lengths. The lengths of the perpendicular arms of the interferometer will be differently modified by the incoming gravitational wave and the interference pattern will change accordingly. These detectors are per nature broadband, being their sensitivity limited only by the smallest time difference they are able to measure. Thanks to the Fabry–Perot cavities, the present and the aimed sensitivities ($\ell \sim 10^{-22} - 10^{-24}$) correspond to interferences over distances many orders of magnitude ($\sim 10^{14}$–10^{16}) smaller than the dimension of an atom, and thus both the stability of the laser beam and the control of all possible noise sources are critical.

These noise sources may be classified as thermal, readout, and seismic:

- The thermal noise is associated to the Brownian motion of the test masses due to the impact of the surrounding air molecules, to their internal vibrations, and to the mirror suspensions. To minimize such effects the rest masses should be placed in a high vacuum environment and the frequencies of the intrinsic resonances of the system should be set as far as possible from the target signal frequency band.
- The intrinsic readout noise is due to the fluctuations induced by the quantum nature of the interaction of the laser light beams with the mirrors. The light beams may be modeled as discrete sets of photons obeying in their arrival time to the mirror to Poisson statistics. The number of photons measured in a time window has a statistical intrinsic fluctuation ("shot noise"); its effects on sensitivity decrease with the increase of the laser power. On the other hand, the increase of the laser power increases the momentum transfer to the mirrors ("radiation pressure"), which will

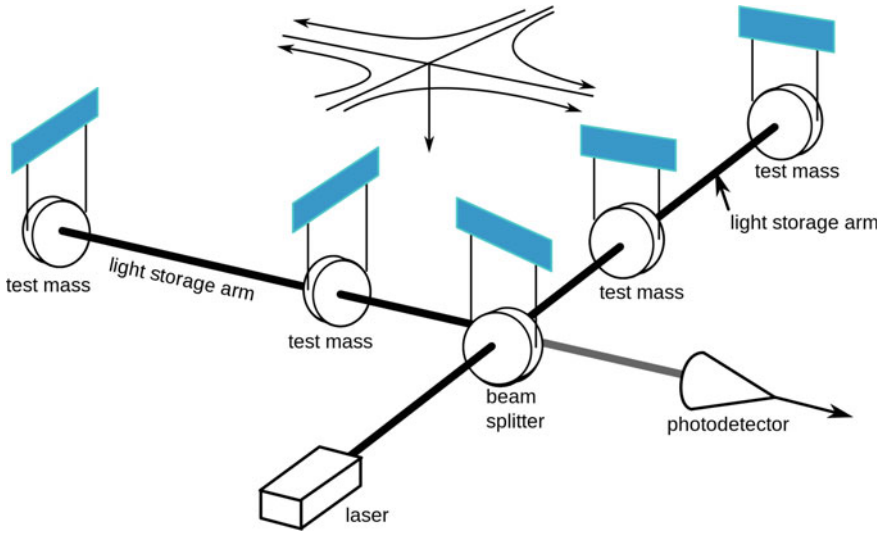

Fig. 4.63 Sketch of a Michelson interferometer. A monochromatic laser light is split into two beams which travel along the two perpendicular arms. The laser light moves back and forth in the two arms between the two mirrors depicted as test masses (Fabry–Perot cavity) and is then made to combine again to form an interference pattern. A gravitational wave passing through (also depicted in the figure) will change the length of one arm with respect to the other, causing relative phase shift of the laser light and thus in the interference pattern. Credit: LIGO Collaboration

change the phase of the beams. To minimize such contradictory effects, the tests masses should be as heavy as possible and the Heisenberg uncertainties relations (the quantum limit) carefully handled.

- The seismic noise accounts for all the natural or human-made perturbations comprising a large range of diversified phenomena like earthquakes, environment perturbations or nearby automobile traffic. The measured spectrum of such noise, in a quiet location, decreases with the frequency and imposes already an important sensitivity constraint to the next generation of laser interferometer detectors. To minimize such effects, the test masses are isolated from ground through several attenuation stages characterized by resonance frequencies much lower than the expected signal frequencies. To access lower frequencies (1–10 Hz), the possibility to build large interferometers underground in a low seismic region is being studied. To go further into the 10^{-4}–10^{-1} Hz region it will be necessary to build a large arm interferometer in space.

The largest gravitational wave observatories operating at present are the Laser Interferometer Gravitational Wave Observatory (LIGO) and Virgo. LIGO is built over two sites in the US (at Hanford, Washington, and at Livingston, Louisiana, 3 000 km apart), each one with a 4 km arm interferometer, while Virgo is installed near Pisa, Italy, and consists of a 3 km arm interferometer. A Japanese underground detector known as KAGRA which is 3 km in arm length is being commissioned and

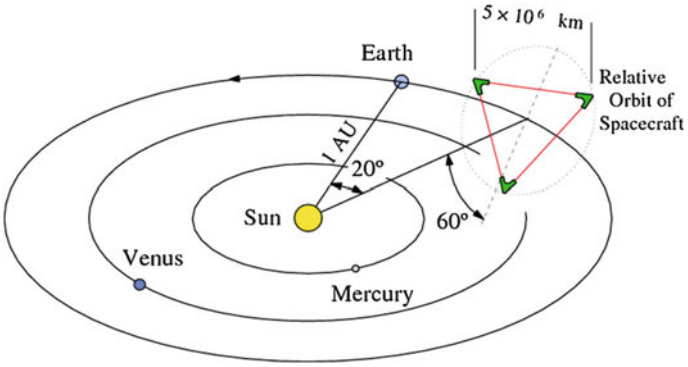

Fig. 4.64 Proposed LISA detector (the size is increased by a factor of 10). From M. Pitkin et al., "Gravitational Wave Detection by Interferometry (Ground and Space)," http://www.livingreviews.org/lrr-2011-5

should start operating in 2019. A third LIGO detector is planned to be built in India before 2024. A close collaboration among all the gravitational waves observatories is in place.

The first detection of gravitational waves was performed by LIGO in 2015; the signal was generated by two black holes with, respectively, 36 and 29 solar masses that merged into a 62 solar masses BH, thus releasing an energy corresponding to $3\,M_{\odot}c^2$ mostly in gravitational waves. Now we have a handful of signals of different phenomena, as we shall discuss in Chap. 10.

The development of new detectors (e.g., interferometers in space) will allow us to explore different frequency bands, and to detect gravitational waves generated by different astrophysical processes. In a more distant future a space observatory will be built extending the detection sensitivity to a much lower frequency range (10^{-4}–10^{-1} Hz). The LISA project, comprising three satellite detectors spaced by more than 2.5 million kilometers (Fig. 4.64), has been approved by ESA; launch is scheduled for the year 2034. Meanwhile a LISA Pathfinder mission was launched and demonstrated the feasibility to achieve the low-frequency noise requirements of the LISA mission.

The present and expected sensitivities of gravitational wave detectors are summarized in Fig. 4.65.

Further Reading

[F4.1] B. Rossi, "High-Energy Particles," Prentice-Hall, New York 1952. Still a fundamental book on particle detection, in particular related to the interaction of particles with matter and to multiplicative showers.

[F4.2] K. Kleinknecht, "Detectors for Particle Radiation" Cambridge University Press 1986.

[F4.3] W.R. Leo, "Techniques for Nuclear and Particle Physics Experiments," Springer Verlag 1994.

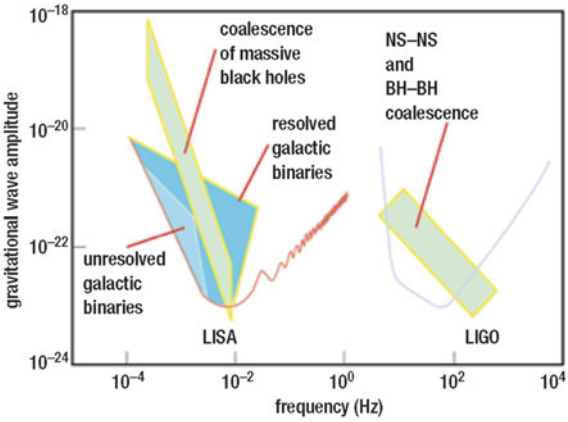

Fig. 4.65 Present and expected sensitivities of gravitational wave detectors. From M. Hendry and G. Woan, Astronomy and Geophysics 48 (2007) 1

Exercises

1. *Muon energy loss*. A muon of 100 GeV crosses a layer of 1 m of iron. Determine the energy loss and the expected scattering angle.
2. *Energy loss in a water Cherenkov detector*. In the Pierre Auger Observatory the surface detectors are composed of water Cherenkov tanks 1.2 m high, each containing 12 tons of water. These detectors are able to measure the light produced by charged particles crossing them. Consider one tank crossed by a single vertical muon with an energy of 5 GeV. The refraction index of water is $n \simeq 1.33$ and can be in good approximation considered constant for all the relevant photon wavelengths. Determine the energy lost by ionization, and compare it with the energy lost by Cherenkov emission.
3. *Cherenkov radiation*. A proton with momentum 1.0 GeV/c passes through a gas at high pressure. The refraction index of the gas can be changed by changing the pressure. Compute: (a) the minimum refraction index at which the proton will emit Cherenkov radiation; (b) the Cherenkov radiation emission angle when the refraction index of the gas is 1.6.
4. *Pair production and multiple scattering*. What is the optimal thickness (in radiation lengths) of a layer of silicon in a gamma-ray telescope with hodoscopic structure in order that the multiple scattering does not deteriorate the information from the opening angle of the electron-positron pair in a photon conversion?
5. *Compton scattering*. A photon of wavelength λ is scattered off a free electron initially at rest. Let λ' be the wavelength of the photon scattered in the direction θ. Compute: (a) λ' as a function of λ, θ and universal parameters; (b) the kinetic energy of the recoiling electron.
6. *Reconstruction of a Compton interaction event*. Detecting gamma rays by Compton scattering in a gamma-ray telescope with hodoscopic structure (Fig. 4.48) is more complicated than for pair production. The Compton scattering of the incident photon occurs in one of the tracker planes, creating an electron and a scattered photon. The tracker measures the interaction location, the electron

energy, and in some cases the electron direction. The scattered photon can be absorbed in the calorimeter where its energy and absorption position are measured.

Suppose that an incident gamma-ray Compton scatters by an angle Θ in one layer of the tracker, transferring energy E_1 to an electron. The scattered photon is then absorbed in the calorimeter, depositing its energy E_2. Demonstrate that the scattering angle is given by $\cos\Theta = m_e c^2/E_2 + m_e c^2/(E_1 + E_2)$, where m_e is the electron mass. With this information, one can derive an "event circle" from which the original photon arrived—this sort of Compton events are called "untracked." Multiple photons from the same source enable a full deconvolution of the image, using probabilistic techniques.

For energetic incident gamma rays (above $\sim$1 MeV), measurement of the track of the scattered electron might in addition be possible, resulting in a reduction of the event circle to a definite direction. If the scattered electron direction is measured, the event circle reduces to an event arc with length due to the uncertainty in the electron direction reconstruction, allowing improved source localization. This event is called "tracked," and its direction reconstruction is somewhat similar to that for pair event—the primary photon direction is reconstructed from the direction and energy of two secondary particles: scattered electron and photon. Comment.

7. *Nuclear reactions*. The mean free path of fast neutrons in lead is of the order of 5 cm. What is the total fast neutron cross section in lead?
8. *Range*. Compare approximately the ranges of two particles of equal velocity and different mass and charge traveling through the same medium.
9. *Hadron therapy*. The use of proton and carbon ion beams for cancer therapy can reduce the complications on the healthy tissue compared to the irradiation with MeV gamma rays. Discuss why.
10. *Neutrino interaction in matter*. For neutrinos produced in nuclear reactors typical energies are $E_\nu \sim 1$ MeV. What is the probability to interact in a water detector with the thickness of one meter? What is the probability to interact inside the Earth traveling along a trajectory that passes through its center? Answer the same questions for a neutrino of energy 1 PeV.
11. *Electromagnetic showers*. How does an electromagnetic shower evolve as a function of the penetration depth in a homogeneous calorimeter? What is the difference between an incoming photon and an incoming electron/positron?
12. *Hadronic showers*. Let us approximate the effective cross section for protons on nucleons in air with a value of 20 mb. Calculate the interaction length of a proton (in g/cm^2, and in meters at NTP). What is the average altitude above the sea level where this interaction takes place? In hadronic showers we find also an electromagnetic component, and muons. Where do these come from?
13. *Tracking detectors*. Could you build a tracking detector for photons? And for neutrinos?
14. *Photodetectors*. What gain would be required from a photomultiplier in order to resolve the signal produced by three photoelectrons from that due to two or

four photoelectrons? Assume that the fluctuations in the signal are described by Poisson statistics, and consider that two peaks can be resolved when their centers are separated by more than the sum of their standard deviations.

15. *Cherenkov counters*. Estimate the minimum length of a gas Cherenkov counter used in the threshold mode to be able to distinguish between pions and kaons with momentum 20 GeV. Assume that 200 photons need to be radiated to ensure a high probability of detection and that radiation covers the whole visible spectrum (neglect the variation with wavelength of the refractive index of the gas).
16. *Electromagnetic calorimeters*. Electromagnetic calorimeters have usually 20 radiation lengths of material. Calculate the thickness (in cm) for calorimeters made of BGO, $PbWO_4$ (as in the CMS experiment at the LHC), uranium, iron, tungsten, and lead. Take the radiation lengths from Appendix B or from the Particle Data Book.
17. *The HERA collider*. The HERA accelerator collided protons at energy $E_p \simeq 820\,\text{GeV}$ with electrons at $E_e \simeq 820\,\text{GeV}$. Which value of E_e would be needed to obtain the same center-of-mass energy at an *ep* fixed-target experiment?
18. *The LHC collider*. What is the maximum energy for a tunnel 27 km long with a maximum magnetic field in the vacuum tube of 8.36 T?
19. *Focusing in the LHC*. The diameter of the vacuum tube in the LHC is 18 mm. How many turns and for how long can a proton beam stay vertically in the tube if you do not focus it?
20. *Collisions in the LHC*. In the LHC ring there are 2835 bunches in each ring which collide with each other once in each detector. How many collisions of bunches are there in

    (a) one second,
    (b) one run which will last about 10 h?

21. *Luminosity*. How much integrated luminosity does an experiment need to collect in order to measure at better than 1% the rate of a process with cross section of 1 pb?
22. *Luminosity measurement at the LEP collider*. The luminosity at the Large Electron–Positron Collider (LEP) was determined by measuring the elastic e^+e^- scattering (Bhabha scattering) as its cross section at low angles is well known from QED. In fact, assuming small polar angles, the Bhabha scattering cross section integrated between a polar angle θ_{min} and θ_{max} is given at first order by

$$\sigma \simeq \frac{1040\,\text{nb}}{s\ /\ \text{GeV}^2}\left(\frac{1}{\theta_{\text{max}}^2 - \theta_{\text{min}}^2}\right).$$

    Determine the luminosity of a run of LEP knowing that this run lasted 4 h, and the number of identified Bhabha scattering events was 1200 in the polar range of $\theta \in [29; 185]$ mrad. Take into account a detection efficiency of 95% and a background of 10% at $\sqrt{s} = m_Z$.

23. *Luminosity and cross section*. The cross section of a reaction to produce the Z boson at the LEP e^+e^- collider is 32 nb at the beam energy 91 GeV. How long did LEP have to wait for the first event if the luminosity was $23 \times 10^{30}\,\mathrm{cm}^{-2}\mathrm{s}^{-1}$?
24. *Synchrotron radiation*. Consider a circular synchrotron of radius R_0 which is capable of accelerating charged particles up to an energy E_0. Compare the radiation emitted by a proton and an electron and discuss the difficulties to accelerate these particles with this technology.
25. *Initial state radiation*. The effective energy of the elastic e^+e^- scattering can be changed by the radiation of a photon by the particles of the beam (initial state radiation), which is peaked at very small angles. Supposing that a measured e^+e^- pair has the following transverse momenta: $p_1^t = p_2^t = 5\,\mathrm{GeV}$, and the radiated photon is collinear with the beam and has an energy of 10 GeV, determine the effective energy of the interaction of the electron and positron in the center of mass, $\sqrt{s_{e^+e^-}}$. Consider that the beam was tuned for $\sqrt{s} = m_Z$.
26. *Bending radius of cosmic rays from the Sun*. What is the bending radius of a solar proton, 1 MeV kinetic energy, in the Earth's magnetic field (0.5 G), for vertical incidence with respect to the field?
27. *Low Equatorial Orbit*. Low-Earth Orbits (LEOs) are orbits between 300 and 2000 km from the ground; the altitude is optimal in order to protect them from cosmic rays, thanks to the Van Allen radiation belts. Due to atmospheric drag, satellites do not usually orbit below 300 km. What is the velocity of an Earth satellite in a LEO and how does it compare to the escape velocity from Earth? How many revolutions per day does it make? Suppose that the satellite sees a solid angle of $2\pi/5$, and that it rolls: after how many hours will it observe all the sky?
28. *Electromagnetic showers in the atmosphere*. If a shower is generated by a gamma ray of $E = 1\,\mathrm{TeV}$ penetrating the atmosphere vertically, considering that the radiation length X_0 of air is approximately $37\,\mathrm{g/cm}^2$ and its critical energy E_c is about 88 MeV, calculate the height h_M of the maximum of the shower in the Heitler model and in Rossi's approximation B.
29. *Extensive electromagnetic air showers*. The main characteristic of an electromagnetic shower (say, initiated by a photon) can be obtained using a simple Heitler model. Let E_0 be the energy of the primary particle and consider that the electrons, positrons and photons in the cascade always interact after traveling a certain atmospheric depth $d = X_0$, and that the energy is always equally shared between the two particles. With this assumptions, we can schematically represent the cascade as in Fig. 4.10.

    (a) Write the analytical expressions for the number of particles and for the energy of each particle at depth X as a function of d, n and E_0.
    (b) The multiplication of the cascade stops when the particles reach a critical energy, E_c (when the decay probability surpasses the interaction probability). Using the expressions obtained in the previous question, write as a function of E_0, E_c and $\lambda = d/\ln(2)$, the expressions, at the shower maximum, for:
        i. the average energy of the particles,

ii. the number of particles, $N_{\max}$,
iii. the atmospheric depth, $X_{\max}$.

30. *Extensive hadronic air showers*. Consider a shower initiated by a proton of energy E_0. We will describe it with a simple Heitler-like model: after each depth d an equal number of pions, n_π, of each of the 3 types is produced: π^0, π^+, π^-. Neutral pions decay through $\pi^0 \to \gamma\gamma$ and their energy is transferred to the electromagnetic cascade. Only the charged pions will feed the hadronic cascade. We consider that the cascade ends when these particles decay as they reach a given decay energy E_{dec}, after n interactions, originating a muon (plus an undetected neutrino).

(a) How many generations are needed to have more that 90% of the primary energy, E_0 in the electromagnetic component?
(b) Assuming the validity of the superposition principle, according to which a nucleus of mass number A and energy E_0 behaves like A nucleons of energy E_0/A, derive expressions for:
i. the depth where this maximum is reached, $X_{\max}$,
ii. the number of particles at the shower maximum, $N_{\max}$,
iii. the number of muons produced in the shower, N_μ.

31. *Cherenkov telescopes*. Suppose you have a Cherenkov telescope with 7 m diameter, and your camera can detect a signal only when you collect 100 photons from a source. Assuming a global efficiency of 0.1 for the acquisition system (including reflectivity of the surface and quantum efficiency of the PMT), what is the minimum energy (neglecting the background) that such a system can detect at a height of 2 km a.s.l.?
32. *Cherenkov telescopes and muon signals*. Show that the image of the Cherenkov emission from a muon in the focal plane of a parabolic IACT is a conical section (approximate the Cherenkov angle as a constant).
33. *Imaging Atmospheric Cherenkov Telescopes*. In the isothermal approximation, the depth x of the atmosphere at a height h (i.e., the amount of atmosphere above h) can be approximated as

$$x \simeq Xe^{-h/7\,\mathrm{km}},$$

with $X \simeq 1030\,\mathrm{g/cm^2}$. If a shower is generated by a gamma ray of $E = 1\,\mathrm{TeV}$ penetrating the atmosphere vertically, considering that the radiation length X_0 of air is approximately $36.6\,\mathrm{g/cm^2}$ (440 m) and its critical energy E_c is about 88 MeV and using Rossi's approximation B (Table 4.1):

(a) Calculate the height h_M of the maximum of the shower in the Heitler model and in Rossi's approximation B.
(b) If 2000 useful Cherenkov photons per radiation length are emitted by charged particles in the visible and near UV, compute the total number N_γ of Cherenkov photons generated by the shower (note: the critical energy is larger than the Cherenkov threshold).

(c) Supposing that the Cherenkov photons are all emitted at the center of gravity of the shower (that in the Heitler approximation is just the maximum of the shower minus one radiation length), compute how many photons per square meter arrive to a detector at an altitude h_d of 2000 m, supposing that the average attenuation length of photons in air is 3 km, and that the light pool can be derived by an opening angle of $\sim 1.3^\circ$ from the shower maximum (1.3° is the Cherenkov angle and 0.5°, to be added in quadrature, comes from the intrinsic shower spread). Comment on the size of a Cherenkov telescope, considering an average reflectivity of the mirrors (including absorption in transmission) of 70%, and a photodetection efficiency (including all the chains of acquisition) of 20%.

(d) Redo the calculations for $E = 50\,\text{GeV}$, and comment.